



NRL/FR/7140--99-9923

# **Space-Frequency Correlations in Multistatic Acoustic Reverberation Due to a Wind-Driven Sea Surface: Theoretical Results at Low Frequency**

R. F. GRAGG

*Acoustic Systems Branch  
Acoustics Division*

November 26, 1999

REPORT DOCUMENTATION PAGE			Form Approved OMB No. 0704-0188	
Public reporting burden for this collection of information is estimated to average 1 hour per response, including the time for reviewing instructions, searching existing data sources, gathering and maintaining the data needed, and completing and reviewing the collection of information. Send comments regarding this burden estimate or any other aspect of this collection of information, including suggestions for reducing this burden, to Washington Headquarters Services, Directorate for Information Operations and Reports, 1215 Jefferson Davis Highway, Suite 1204, Arlington, VA 22202-4302, and to the Office of Management and Budget, Paperwork Reduction Project (0704-0188), Washington, DC 20503.				
1. AGENCY USE ONLY (Leave Blank)	2. REPORT DATE  November 26, 1999	3. REPORT TYPE AND DATES COVERED  Final		
4. TITLE AND SUBTITLE  Space-Frequency Correlations in Multistatic Acoustic Reverberation Due to a Wind-Driven Sea Surface: Theoretical Results at Low Frequency			5. FUNDING NUMBERS	
6. AUTHOR(S)  R. F. Gragg				
7. PERFORMING ORGANIZATION NAME(S) AND ADDRESS(ES)  Naval Research Laboratory Washington, DC 20375-5320			8. PERFORMING ORGANIZATION REPORT NUMBER  NRL/FR/7140—99-9923	
9. SPONSORING/MONITORING AGENCY NAME(S) AND ADDRESS(ES)  Office of Naval Research 800 North Quincy Street Arlington, VA 22217-5660			10. SPONSORING/MONITORING AGENCY REPORT NUMBER	
11. SUPPLEMENTARY NOTES				
12a. DISTRIBUTION/AVAILABILITY STATEMENT  Approved for public release; distribution is unlimited.			12b. DISTRIBUTION CODE	
13. ABSTRACT (Maximum 200 words)  Analytic methods are used to assess the impact of the two-dimensional (2-D) wave spectrum of a wind-driven sea on multistatic low-frequency surface reverberation. The problem is initially posed with a narrowband source beneath a time-dependent sea surface in an ocean that can have depth dependence and bottom layering. The propagated signal interacts with the slower moving surface waves to produce a narrowband scattered field. The small-waveheight approximation is applied to a deterministic sea surface to express the scattered field in terms of the surface elevation and the Green's function for a perfectly calm sea. Randomness is then incorporated into the surface description, and its impact is formulated for an arbitrarily placed pair of receivers. The three-dimensional (3-D) cross-spectral density (CSD) of the reverberation is reduced to a sum of baseband and sideband terms formulated as multiple mean-sea-surface integrals. The sideband result is identified as an active scattering generalization of the van Cittert-Zernike theorem from partial coherence theory. The focus is then narrowed to shallow deployment in a homogeneous ocean, and stationary-phase estimates are used to produce analytic expressions for the CSD. The zero-Doppler component and Bragg-Doppler sidebands are expressed in terms of the power spectrum of the source, the power spectrum and directionality of the surface waves, and the multistatic source/receiver geometry. Sample sideband calculations are provided to illustrate the results, and system implications are considered.				
14. SUBJECT TERMS  Surface reverberation Partial coherence Small-waveheight approximation			15. NUMBER OF PAGES  55	
van Cittert-Zernike theorem Bragg scattering Doppler shift			16. PRICE CODE	
17. SECURITY CLASSIFICATION OF REPORT  UNCLASSIFIED	18. SECURITY CLASSIFICATION OF THIS PAGE  UNCLASSIFIED	19. SECURITY CLASSIFICATION OF ABSTRACT  UNCLASSIFIED	20. LIMITATION OF ABSTRACT  UL	

# CONTENTS

1. INTRODUCTION . . . . .	1
1.1 Overview . . . . .	1
1.2 Background . . . . .	2
1.3 Conventions and Notation . . . . .	3
2. AMPLITUDES . . . . .	4
2.1 Surface Elevation . . . . .	4
2.2 Scattered Field . . . . .	5
2.2.1 Differential Problem . . . . .	6
2.2.2 Narrowband Emission from a Point Source . . . . .	6
2.2.3 Integral Formulation . . . . .	6
2.2.4 Small-Waveheight Approximation . . . . .	7
3. MOMENTS . . . . .	8
3.1 Source Modulation . . . . .	8
3.2 Surface Elevation . . . . .	8
3.2.1 Free-Wave Sea Surface . . . . .	8
3.2.2 Surface Frequency Spectrum and Directionality . . . . .	9
3.3 Scattered Field . . . . .	9
3.3.1 Order 0 . . . . .	10
3.3.2 Order 1 . . . . .	10
3.3.3 Order 2, Baseband Terms . . . . .	10
3.3.4 Order 2, Sideband Terms . . . . .	11
3.4 Summary of the Reverberation CSD . . . . .	13
3.4.1 Baseband . . . . .	13
3.4.2 Sidebands . . . . .	13
4. SHALLOW DEPLOYMENT IN A UNIFORM OCEAN . . . . .	14
4.1 Green's Function . . . . .	14
4.2 Baseband, Order 0 . . . . .	14
4.3 Baseband, Order 2 . . . . .	15
4.3.1 Fundamental Integral . . . . .	15
4.3.2 Stationary-Phase Evaluation . . . . .	15
4.3.3 CSD Estimate . . . . .	16
4.4 Baseband Summary . . . . .	16
4.5 Sidebands, Fundamental Integral . . . . .	17
4.6 Sidebands, Stationary-Phase Evaluation . . . . .	18

4.6.1	Stationary Points . . . . .	20
4.6.2	Phase Factors . . . . .	23
4.6.3	Amplitude Factors . . . . .	24
4.6.4	Synthesis . . . . .	24
4.6.5	Bragg-Only Constraint . . . . .	24
4.7	Sidebands, CSD Estimate . . . . .	25
4.8	Sidebands, Colocated Receivers: the PSD . . . . .	26
4.9	Sidebands, Symmetries . . . . .	26
5.	SIDEBAND SIMULATIONS . . . . .	27
5.1	Horizontal Geometries . . . . .	29
5.2	Vertical Geometries . . . . .	44
6.	SUMMARY AND CONCLUSIONS . . . . .	46
7.	ACKNOWLEDGMENT . . . . .	47
	REFERENCES . . . . .	48
	APPENDIX – Bipolar Coordinates . . . . .	51



# SPACE-FREQUENCY CORRELATIONS IN MULTISTATIC ACOUSTIC REVERBERATION DUE TO A WIND-DRIVEN SEA SURFACE: THEORETICAL RESULTS AT LOW FREQUENCY

## 1. INTRODUCTION

### 1.1 Overview

For decades, the U.S. Navy's operational needs were well served by the pursuit of acoustic antisubmarine warfare (ASW) as a largely passive enterprise. In recent years, however, the emphasis has shifted strongly toward active operations, and this change has lent newfound importance to some hitherto secondary topics. Prominent among these is the irregular and dynamic nature of the sea surface. Previously of interest only in connection with ambient noise and propagation loss, the surface has taken on new importance as a source of reverberation in active systems. Features of particular interest in the reverberant field are (a) Doppler shifts, which can mimic or mask the echoes from moving targets, and (b) two-point spatial correlations, whose nature may ultimately help systems distinguish target returns from surface reverberation.

This report treats the second-order space-frequency statistics of reverberation from time-dependent sea surfaces. The focus is on low frequencies and wind speeds, where interface scattering dominates bubble effects [1]. Theoretical techniques are used to express the reverberation's Doppler characteristics and spatial correlations in terms of accepted empirical parameterizations for the surface-wave statistics. The overall goal is a comprehensive expression for the second-order spatial and temporal correlation features that relate to acoustic systems operating in the low-frequency (LF) band. Naturally, some judicious physical approximations must be made. The source is treated as a motionless point that emits a narrowband signal. The environment is allowed to have depth dependence (including a layered bottom), but every part of it is range-independent, deterministic, and static—with one exception. That exception is the sea surface, which is composed of waves traveling in all directions with various (and ultimately random) amplitudes and phases. A comprehensive new formulation is derived for the cross-spectral density (CSD) of the reverberation in terms of (a) the second-order statistics of the sea surface and (b) the Green's function for the same environment *without* surface waves. This is expected to provide a basis for future work in complex environments; however, for the remainder of this report, the subsurface medium is represented as a homogeneous half-space. This simplification allows analytic methods to reduce a crucial fivefold spatial integration to a single azimuth integral. The result is a novel analytic expression from which model computations are easily done. Sample computations are carried out to display the dependence of the amplitudes and phases of the CSD sidebands on the multistatic horizontal and vertical placement of the receiver pair, the wind speed, and the directionality of the surface waves.

Section 2 deals on a deterministic level with the two fundamental elements of the problem—the sea surface and the acoustic field scattered from it. First, the makeup of a deterministic time-dependent surface is discussed and then the small-waveheight approximation (SWHA) is invoked to characterize the narrowband signal that results from scattering by such a surface. In

Section 3, the surface elevation is treated as a random process that is stationary both in time and in horizontal coordinates. A SWHA series is obtained for the resulting reverberation CSD throughout the water and sediment, and the terms are grouped into baseband contributions (zeroth order and second order) and Bragg-Doppler sidebands (second order only). The sideband expression, Eq. (30), is recognized as an active-scattering extension of the van Cittert-Zernike theorem from the classical theory of partially coherent fields. With the sea surface described in terms of its power spectrum and directional spectrum, each CSD term is reduced to an azimuthal integration involving a fundamental integral over surface wavenumber. Section 3.4 summarizes the results. In Section 4, the fundamental integrals for the baseband and sidebands are evaluated by two-dimensional (2-D) stationary phase estimation for a uniform ocean. This uses a source/receiver geometry that yields analytic results: the source and receivers are deployed at depths much less than the ranges involved. Section 5 presents a set of computer simulations for the sidebands. These are done using the Pierson-Moskowitz power spectrum and Longuet-Higgins directional spectrum to illustrate the sensitivity of the sidebands to receiver placement, frequency, and sea-surface parameters. Section 6 presents a summary and conclusions.

## 1.2 Background

Perturbative treatment of sea-surface scattering is certainly not a new idea. Indeed, various perturbative approaches are to be found throughout the acoustics and radar literatures. Some of these deserve particular mention here in relation to the present work.

In the 1970s, Harper and Labianca published a series of articles [2–6] that applied analytic techniques to the theory of bistatic sea-surface scattering. Their main result was a formalism for describing the Doppler sidebands in the power spectral density (PSD). The present report has certain basic features in common with that work. Both use perturbation theory along with Rayleigh’s approximation for the surface boundary condition, and both ultimately treat the source signal and sea surface as stochastic inputs that generate a stochastic output—the scattered field—whose second moment is the basic goal of the analysis. In other respects, however, the two approaches differ. Harper and Labianca began by modeling the input stochastic processes themselves. They then used analytic wave-propagation techniques to determine the resulting output process and, finally, ensemble-averaged a quadratic expression in the output to produce the desired second moment. This required devoting considerable effort to devising an ensemble of faithful realizations of the sea surface and to obtaining the consequent realizations for the perturbative contributions to the scattered field, including those that ultimately contribute nothing to the ensemble average.

In contrast, this report (a) addresses multistatic sea-surface scattering and (b) approaches the subject directly on the level of second-order statistics [7, Chapter 5]. It follows the basic agenda of the classical theory of partially coherent wave fields [8–11], exploiting an input/output relation for the field’s *second moment* rather than for the field itself. That relation arises as follows. The field’s general space-time second moment  $\Gamma(\vec{r}_1, t_1, \vec{r}_2, t_2)$  obeys two wave equations—in  $\vec{r}_1, t_1$  and in  $\vec{r}_2, t_2$ . For a field that is statistically stationary in time, this moment reduces to the Mutual Coherence Function (MCF),  $C(\vec{r}_1, \vec{r}_2, \tau)$ , which depends on the time *difference*  $\tau = t_2 - t_1$ . Its transform in the frequency domain is the CSD,  $C(\vec{r}_1, \vec{r}_2, f)$ , which obeys a pair of Helmholtz equations—in  $\vec{r}_1$  and in  $\vec{r}_2$ —within any source-free region  $\vec{r}_1, \vec{r}_2 \in V$ . Green’s theorem then provides the desired input/output relation—an expression for the CSD inside  $V$  in the form of an integral over the boundary  $\vec{r}_1, \vec{r}_2 \in \partial V$  involving the appropriate Green’s function and boundary values.

In this form, that relation would be prohibitively difficult to use, since its input involves integration over the actual sea surface. Fortunately, in the small-waveheight regime, one can use a

classic Rayleigh technique to replace the exact expression by a perturbative series approximation, each term of which involves integration over the *mean* sea-surface—a simple horizontal plane. In this perturbative representation, the  $n$ th-order contribution to the output is generated by the  $n$ th angle and frequency moments of the surface-wave distribution. Harper and Labianca followed basically the same procedure in producing a perturbative series for the field amplitude. However, the desired result—the  $n$ th perturbative contribution to the output moment—is more readily obtained when the procedure is applied to the moments rather than to the stochastic process itself. In that context, it is immediately clear, for example, that the first-order contribution to the CSD vanishes identically. Working on the level of moments also seems to have an advantage in terms of reliability. Their work with the stochastic field amplitude led Harper and Labianca to assert that reciprocity failed beyond the second perturbative order [6, p. 1,149]. This claim appears to be an artifact of the complexity of their approach and is not borne out here.

In 1993, Goalwin published an article [12] that modeled the multistatic reverberation CSD for a pair of receivers. His work, like the present effort, approached the problem on the level of second moments and obtained a multiple-integral expression for the second-order perturbative contribution. To facilitate the analysis, however, he placed the receivers at a common depth and was, thus, unable to examine the vertical aspects of spatial correlation. More significantly, he dealt with the sea surface as a “frozen” (motionless) interface, thereby precluding any treatment of surface Doppler. In addition, like Harper and Labianca, Goalwin applied the stationary-phase method only numerically, obtaining no analytic results comparable to those produced here.

### 1.3 Conventions and Notation

Vectors in 3-D are indicated by arrows, and 2-D vectors and matrices are denoted by underlining (e.g., 3-D vector  $\vec{r} = (\underline{r}, z)$  and 2-D matrix  $\underline{m}$ ). Directions in the horizontal plane are often specified in terms of the a unit vector  $\underline{n}(\theta)$  that points along an azimuth  $\theta$  relative to the dominant wind direction. The frequency  $f$  or its angular counterpart  $\omega = 2\pi f$  (or both) may appear in any given expression; the choice is entirely a matter of convenience. The same is true for the horizontal wavevector  $\underline{k} = 2\pi\underline{s}$ .

The standard Fourier transformation connects the time and frequency domains:  $a(f) = \int_{-\infty}^{+\infty} dt E(+ft)a(t)$  with the kernel  $E(q) = \exp(i2\pi q)$ . The same basic symbol is used in both domains— $a(t)$ ,  $a(f)$ —with only the argument identifying which one is meant. The relation is often denoted  $a(t) \xrightarrow{t \rightarrow f} a(f)$ , with the arrow indicating the forward direction. The variables above the arrow are sometimes omitted when they should be clear from context. The spatial Fourier transform in two dimensions follows the same pattern except that, because of the traveling-wave form  $E(\underline{s} \cdot \underline{r} - ft)$ , its kernel uses the opposite sign:  $a(\underline{s}) = \int d^2\underline{r} E(-\underline{s} \cdot \underline{r})a(\underline{r})$ . Again, the transformation is denoted  $a(\underline{r}) \xrightarrow{\underline{r} \rightarrow \underline{s}} a(\underline{s})$ , with the arrow indicating the forward direction (this time, the one with the minus in its kernel).

When  $a(t)$  is effectively constant, it will be written as  $a(\textit{t})$  to emphasize that it is virtually a dc signal. To the same approximation, its spectrum is singular:  $a(f) \approx a(f \sim 0)\delta(f)$ , where  $a(f \sim 0) = \int_0^{0+} df a(f)$  denotes the integrated strength of the singularity. Numerically, of course,  $a(f \sim 0) = a(\textit{f})$ . Likewise, when  $a(\underline{r})$  is effectively independent of  $\underline{r}$ , it is denoted  $a(\textit{r})$  and its wavenumber spectrum is  $a(\underline{s}) \approx a(\underline{s} \sim \underline{0})\delta(\underline{s})$ , where  $a(\underline{s} \sim \underline{0}) = a(\textit{s})$ . These are understood in the same spirit as expressions like “ $\alpha \ll \beta$ ” (i.e., as a physical notation rather than a purely mathematical one).

A field  $a(\underline{r}, t)$  is a function of both spatial position and time. Double Fourier transforma-

tion,  $a(\underline{r}, t) \xrightarrow{t \xrightarrow{f} \underline{s}} a(\underline{s}, f)$ , allows it to be viewed as a function of wavenumber and frequency  $a(\underline{s}, f)$ . Although any physical field can be represented as a real-valued function in the space/time domain— $a(\underline{r}, t) = a^*(\underline{r}, t)$ , with the corresponding symmetry  $a(\underline{s}, f) = a^*(-\underline{s}, -f)$  in the wavenumber/frequency domain—it will usually be more convenient to use representations involving complex-valued fields  $\alpha(\underline{r}, t)$ . This practice (the equivalent of representing  $\cos q$  by the real part of  $e^{iq}$ ) is perfectly harmless provided due care is used with nonlinear functions of the field, particularly the quadratic form  $\alpha^*(\underline{r}_1, t_1)\alpha(\underline{r}_2, t_2)$ .

We will need to deal with the second-order statistical moments of fields (i.e., ensemble averages of such quadratic forms). Of course, we may equally well deal with moments of  $\alpha(\underline{r}, f)$ ,  $\alpha(\underline{s}, t)$ , or  $\alpha(\underline{s}, f)$ , instead. Our interest, then, will be focused on the two-point correlations in one of these forms:

$$\begin{aligned}\Gamma_\alpha(\underline{r}_1, t_1, \underline{r}_2, t_2) &= \langle \alpha^*(\underline{r}_1, t_1) \alpha(\underline{r}_2, t_2) \rangle \\ \Gamma_\alpha(\underline{r}_1, f_1, \underline{r}_2, f_2) &= \langle \alpha^*(\underline{r}_1, f_1) \alpha(\underline{r}_2, f_2) \rangle \\ \Gamma_\alpha(\underline{s}_1, f_1, \underline{s}_2, f_2) &= \langle \alpha^*(\underline{s}_1, f_1) \alpha(\underline{s}_2, f_2) \rangle .\end{aligned}$$

Here too, the same main symbol is used universally, and only the arguments distinguish the space/wavenumber and time/frequency domains. Naturally, since Fourier transformations connect these domains, all three forms are equivalent. In dealing with statistically stationary fields, it is often convenient to use “mean and difference” coordinates (i.e., to re-express the dependence on a coordinate pair  $(\zeta_i, \zeta_j)$  in terms of a dependence on their mean  $\bar{\zeta}_{ij} = \frac{1}{2}(\zeta_j + \zeta_i)$  and difference  $\zeta_{ij} = \zeta_j - \zeta_i$ ). In this representation, the three moments above are

$$\begin{aligned}\Gamma_\alpha(\underline{r}_{12}, t_{12}, \bar{\underline{r}}_{12}, \bar{t}_{12}) &= \langle \alpha^*(\underline{r}_1, t_1) \alpha(\underline{r}_2, t_2) \rangle \\ \Gamma_\alpha(\underline{r}_{12}, \bar{f}_{12}, \bar{\underline{r}}_{12}, f_{12}) &= \langle \alpha^*(\underline{r}_1, f_1) \alpha(\underline{r}_2, f_2) \rangle \\ \Gamma_\alpha(\bar{\underline{s}}_{12}, \bar{f}_{12}, \underline{s}_{12}, f_{12}) &= \langle \alpha^*(\underline{s}_1, f_1) \alpha(\underline{s}_2, f_2) \rangle .\end{aligned}$$

Temporal stationarity is so common that special notation and terminology are used.

$$C_\alpha(\underline{r}_1, \underline{r}_2, t_{12}) \stackrel{def}{=} \Gamma_\alpha(\underline{r}_{12}, t_{12}, \bar{\underline{r}}_{12}, \bar{t}_{12}) = C_\alpha^*(\underline{r}_2, \underline{r}_1, -t_{12})$$

is called the MCF, and its  $t_{12} \xrightarrow{\bar{f}_{12}}$  transform,

$$C_\alpha(\underline{r}_1, \underline{r}_2, \bar{f}_{12}) \stackrel{def}{=} \Gamma_\alpha(\underline{r}_{12}, \bar{f}_{12}, \bar{\underline{r}}_{12}, f_{12} \sim 0) = C_\alpha^*(\underline{r}_2, \underline{r}_1, \bar{f}_{12}),$$

is known as the CSD or Mutual Spectral Density Function (MSDF).

## 2. AMPLITUDES

We begin by formulating the problem in the context of a time-dependent linear system with one input,  $e(t)$ , the signal emitted by the source; one internal time dependence,  $h(\underline{r}, t)$ , the sea-surface elevation; and one output,  $A(\vec{r}, t)$ , the modulation of the field scattered by the surface. Initially these are all treated as deterministic quantities. A stochastic treatment follows in Section 3.

### 2.1 Surface Elevation

Even if the surface elevation were completely arbitrary, it could still be Fourier analyzed via  $h(\underline{r}, t) \xrightarrow{t \xrightarrow{f} \underline{s}} h(\underline{s}, f)$  (i.e., synthesized from unrestricted sinusoids  $E(\underline{s} \cdot \underline{r} - ft)$ ) according to

$$h(\underline{r}, t) = \int_{R^2} d^2 \underline{s} \int_{-\infty}^{+\infty} df E(\underline{s} \cdot \underline{r} - ft) h(\underline{s}, f) , \quad (1)$$

with only the requirement that  $h(\underline{s}, f) = h^*(-\underline{s}, -f)$  to guarantee that  $h(\underline{r}, t)$  is real. But of course the surface elevation is not that arbitrary. Its components are traveling waves<sup>1</sup> that obey the appropriate dispersion relation for waves on the sea surface—a constraint in the form of a mapping  $|f| = F(s)$ , where  $s = |\underline{s}|$  (or, equivalently,  $s = S(|f|)$  in terms of the inverse map  $S = F^{-1}$ ). The functional form of  $F(s)$  depends on the nature of the restoring forces acting on surface displacements at the fundamental length scale of the problem. For the present, we only note that  $F(s)$  must be an increasing differentiable function on  $s > 0$  and vanish at the origin ( $F'(s) > 0$ ,  $F(0) = 0$ ). This is general enough to span the spectrum from capillary to gravity waves in deep or shallow water [14, Eq. (6.3.12)]. Incorporating a surface dispersion relation imposes the restriction  $\underline{s} = S(|f|)\underline{n}(\theta)$  on the 3-D integration region  $\{\underline{s} \in R^2, |f| < \infty\}$  in Eq. (1), shrinking it to the 2-D manifold  $\{\underline{s} \in R^2, |f| = F(s)\}$ .

Alternatively, one may use a synthesis like

$$h(\underline{r}, t) = \oint d\theta \int_0^\infty df \alpha(\theta, f) \cos\{\phi(\theta, f) + 2\pi[S(f)\underline{n}(\theta) \cdot \underline{r} - ft]\} \quad (2)$$

in which  $\oint d\theta$  is a  $360^\circ$  azimuth integration, and the traveling-wave component for each  $\{\theta, f\}$  has an amplitude  $\alpha$  and a phase  $\phi$ , both real. This arguably has more down-to-earth physical realism on its side because (a) it incorporates the dispersion relation in a natural way, (b) it is manifestly real-valued, and (c) it avoids double-counting (since  $f \geq 0$ , the component with  $\{\theta, |f|\}$  is included, but its physical twin with  $\{\theta + \pi, -|f|\}$  is not).

Used consistently, the two approaches are, naturally, equivalent. The  $\alpha$  and  $\phi$  in Eq. (2) are specified only for positive frequencies, but their definitions can be extended to the negative spectrum via  $\alpha(\theta, -f) = +\alpha(\theta + \pi, f)$  and  $\phi(\theta, -f) = -\phi(\theta + \pi, f)$ . In terms of the complex amplitude,  $u(\theta, f) = \frac{1}{2}\alpha(\theta, f)e^{i\phi(\theta, f)}$  whose symmetry is  $u(\theta, f) = u^*(\theta + \pi, -f)$ , Eq. (2) is simply

$$h(\underline{r}, t) = \int_{-\infty}^{+\infty} df \oint d\theta u(\theta, f) E(S(f)\underline{n}(\theta) \cdot \underline{r} - ft) . \quad (3)$$

Any physically realizable sea surface can be synthesized in this way by integrations over azimuth and frequency. The symmetry of  $u$  guarantees  $h(\underline{s}, f) = h^*(-\underline{s}, -f)$ , so that  $h(\underline{r}, t)$  remains real. A comparison of Eqs. (1) and (3) shows that

$$h(\underline{s}, f) = \frac{\delta(s - S(f))}{s} u(\theta, f) , \quad (4)$$

which illustrates how the dispersion relation restricts the surface elevation in the wavenumber/frequency domain.

## 2.2 Scattered Field

Initially we regard the sea surface,  $z = h(\underline{r}, t)$ , as a deterministic boundary and present an expression for the acoustic field that scatters from it. The subsurface acoustic environment is prescribed by the sound speed  $c$  and density  $\rho$ , which are considered to be continuous functions of depth except for simple discontinuities wherever the material properties change abruptly (e.g., at the sea floor and at sediment interfaces).

<sup>1</sup>We are representing these surface components as perfect sinusoids. Their shape is actually slightly distorted by the orbital motion of the near-surface water, but the effect is negligible for small waveheights [13].

### 2.2.1 Differential Problem

This corresponds to a linear differential boundary value problem of the familiar form

$$\mathcal{W}P(\vec{r}, t) = Q(\vec{r}, t) \quad \cdots \quad z > h(\underline{x}, t) \quad (5a)$$

$$P(\vec{r}, t) = 0 \quad \cdots \quad z = h(\underline{x}, t) \quad (5b)$$

$$P(\vec{r}, t) \rightarrow 0 \quad \cdots \quad |\vec{r}| \rightarrow \infty \quad (5c)$$

featuring a wave operator [15],  $\mathcal{W} = -\{\rho(\vec{r})\partial/\partial\vec{r}\} \cdot \{\rho^{-1}(\vec{r})\partial/\partial\vec{r}\} + c^{-2}(\vec{r})\partial^2/\partial t^2$ , determined by the medium's sound speed and density. In signal engineering terms, the environment, in conducting the signal from source to receiver, acts as a linear filter. Two things drive the system: the source function  $Q(\vec{r}, t)$  and the sea-surface elevation  $h(\underline{x}, t)$ . It is the latter that makes the problem challenging by causing the ocean to act as a *time-varying* filter. Other conceivable contributors, such as time-dependence or randomness in  $c$  and  $\rho$ , are disallowed in the present formulation.

Although this problem is well posed in a mathematical sense [16], it is appropriate to make at least passing mention of some of its physical shortcomings. First, it is implicit that  $c$  and  $\rho$  must actually be uniform near the surface if there is to be no time-dependence within the medium. This means excluding all effects associated with near-surface hydrodynamics, such as the advection of air bubbles by the subsurface water [17]. In fact, scattering by near-surface bubbles [18], whether advecting or not, is omitted altogether. Furthermore, a more realistic surface boundary condition might even be applied. An air/water impedance condition, for instance, would allow transmission into the air and that may actually be a significant loss mechanism in shallow water [19].

### 2.2.2 Narrowband Emission from a Point Source

We suppose that the source is fixed in position and that its time-dependence is uniform throughout. This time-dependence we take to be a modulation applied to a carrier frequency  $f_0$ . Thus the source term is  $Q(\vec{r}, t) = q(\vec{r})e(t)\exp(-i\omega_0 t)$ . The resulting acoustic field has the form  $P(\vec{r}, t) = A(\vec{r}, t)\exp(-i\omega_0 t)$ , in which  $A(\vec{r}, t)$ , like  $e(t)$ , is a slow complex modulation.<sup>2</sup> We further idealize the source as a spatial point (i.e., take  $q(\vec{r}) = \delta(\vec{r} - \vec{r}_0)$ ). To zeroth order (i.e., neglecting  $\partial A/\partial(\omega_0 t)$  and  $\partial^2 A/\partial(\omega_0 t)^2$  relative to  $A$ ), we obtain

$$\hat{\mathcal{W}}A(\vec{r}, t) = e(t)\delta(\vec{r} - \vec{r}_0) \quad \cdots \quad z > h(\underline{x}, t) \quad (6a)$$

$$A(\vec{r}, t) = 0 \quad \cdots \quad z = h(\underline{x}, t) \quad (6b)$$

$$A(\vec{r}, t) \rightarrow 0 \quad \cdots \quad |\vec{r}| \rightarrow \infty, \quad (6c)$$

in which  $\hat{\mathcal{W}} = -(\{\rho(\vec{r})\partial/\partial\vec{r}\} \cdot \{\rho^{-1}(\vec{r})\partial/\partial\vec{r}\} + k_0^2(\vec{r}))$  is a general Helmholtz operator with a spatially varying wavenumber  $k_0(\vec{r}) = \omega_0/c(\vec{r})$ . The time variation in  $A$  is caused by  $e$  and  $h$ .

When  $h$  is frozen, the function  $A(\vec{r}, t)/e(t)$  loses all dependence on time and is, in fact, simply the space-frequency Green's function for that fixed boundary at the frequency  $f_0$  (i.e., the frequency response function of the now time-invariant environment at the carrier frequency). However, we want to deal with situations in which  $h$  is time dependent. Our first step in doing that is to recast Eq. (6) in integral form.

### 2.2.3 Integral Formulation

For any volume  $V$ , provided its boundary  $\partial V$  remains fixed and the density is uniform along the normal direction at the boundary,  $\hat{\mathcal{W}}U(\vec{r}) = \delta(\vec{r} - \vec{r}_0)$  is, by Green's theorem, equivalent to

<sup>2</sup>  $A$  also depends parametrically on  $\vec{r}_0$  and  $f_0$ , of course, but this will be left implicit.

$$U(\vec{r}) = G(\vec{r}, \vec{r}_0) - \int_{\partial V} d^2\vec{r}_b G_b(\vec{r}, \vec{r}_b) U(\vec{r}_b) \quad \dots \quad \vec{r}, \vec{r}_0 \in V, \quad (7)$$

where  $G(\vec{r}_a, \vec{r}_b)$  is the Green's function<sup>3</sup> for pressure-release conditions on  $\partial V$ , and the subscript notation used in the integrand means

$$G_b(\vec{r}, \vec{r}_b) \stackrel{def}{=} \vec{n}(\vec{r}_b) \cdot \lim_{\vec{u} \rightarrow \vec{r}_b} \left( \frac{\partial G(\vec{r}, \vec{u})}{\partial \vec{u}} \right) \quad \dots \quad \vec{r} \in V, \vec{r}_b \in \partial V, \quad (8)$$

with the limit taken from within  $V$ . It is simply a shorthand for the outward normal derivative with respect to the subscripted argument (i.e., the “boundary Green's function” [20]). Reciprocity is embodied in the expression  $G(\vec{r}_a, \vec{r}_b)\rho(\vec{r}_b) = G(\vec{r}_b, \vec{r}_a)\rho(\vec{r}_a)$ .

Equation (7) can be applied to  $U = A/e$  by identifying  $V$  with the half-space  $z > 0$  and  $\partial V$  with the  $z = 0$  plane,  $S$ . The result is that throughout the water and sediment,

$$A(\vec{r}, t) = e(t)G(\vec{r}, \vec{r}_0) - \int_S d^2\vec{r}_a G_a(\vec{r}, \vec{r}_a) A(\vec{r}_a, t). \quad (9)$$

$G$  is the “sea state zero” Green's function for pressure-release conditions on  $S$ , so that

$$G_a(\vec{r}, \vec{r}_a) = - \left( \frac{\partial G(\vec{r}, \vec{r}_a)}{\partial z_a} \right)_{z_a=0}$$

is just its upward derivative at the surface point  $\vec{r}_a = (\underline{r}_a, 0)$ . Equation (9) relates  $A$  to its values on the fixed plane  $S$ , but it is not a solution because Eq. (6) needs boundary values specified on the actual moving sea surface.

#### 2.2.4 Small-Waveheight Approximation

To get such a solution, one must infer the values of  $A(\vec{r}, t)$  at  $z = 0$  from the vanishing boundary values imposed at  $z = h(\underline{r}, t)$ . This can be done by the SWHA [21]. Since this is such a well-known procedure, we omit the details and simply note that the modulation emerges as a series  $A = A^{(0)} + A^{(1)} + A^{(2)} + \dots$  whose initial terms are

$$A^{(0)}(\vec{r}, t) = e(t)G(\vec{r}, \vec{r}_0) \quad (10a)$$

$$A^{(1)}(\vec{r}, t) = -e(t) \int_S d^2\underline{r}_a G_a(\vec{r}, \vec{r}_a) h(\underline{r}_a, t) G_a(\vec{r}_a, \vec{r}_0) \quad (10b)$$

$$A^{(2)}(\vec{r}, t) = e(t) \iint_S d^2\underline{r}_a d^2\underline{r}_b G_a(\vec{r}, \vec{r}_a) h(\underline{r}_a, t) G_{ab}(\vec{r}_a, \vec{r}_b) h(\underline{r}_b, t) G_b(\vec{r}_b, \vec{r}_0). \quad (10c)$$

Again, the subscript notation of Eq. (8) is used for the surface normal derivatives. All of these  $A^{(n)}$  terms have an implicit parametric dependence on  $\vec{r}_0$  and  $f_0$ , and they all derive their time dependence from both  $e$  and  $h$  (except  $A^{(0)}$ , which is independent of  $h$ ). Furthermore, each  $A^{(n)}$  inherits the Green's function's reciprocity property. It has been suggested [6] that this order-by-order reciprocity might not extend beyond second order; however reciprocity has been explicitly demonstrated for all orders in the cw (continuous wave) case with a frozen surface [22], and it seems clear enough from the above that it does, in fact, persist in general. This is the SWHA for the complex modulation that results when a given narrowband signal scatters from a given time-dependent wave surface. It appears here *not* as a novel result (indeed, Eq. (10) is a minor variation on Eqs. (30) and (31) of Ref. 6) but rather as a natural starting point for the following section's systematic treatment of the source signal and the sea surface as stochastic processes.

<sup>3</sup>The space/frequency Green's function's dependence on  $f_0$  is left implicit.

### 3. MOMENTS

For most real-world applications, one must abandon the depiction of  $e(t)$ ,  $h(\underline{r}, t)$  and  $A(\vec{r}, t)$  as deterministic quantities and instead treat them as random processes. We do that here, taking all of them to be statistically stationary so that their mean values  $\langle e \rangle$ ,  $\langle h \rangle$ ,  $\langle A \rangle$  can be assumed to vanish and attention can be focused on their second moments.

#### 3.1 Source Modulation

The narrowband modulation  $e(t)$  can be characterized by its PSD,  $C_e(f)$ . This can be written in the form  $C_e(f) = P_e R_e(f)$  with the normalization  $\int_{-\infty}^{+\infty} df R_e(f) = 1$  so that the emitted power is  $P_e = \int_{-\infty}^{+\infty} df C_e(f)$ . The Gaussian case with bandwidth  $\Delta f$ , for example, would have  $R_e(f) = \exp[-\frac{1}{2}(f/\Delta f)^2]/(\sqrt{2\pi}\Delta f)$ . But whatever the statistics, when the bandwidth vanishes,  $R_e(f)$  reduces to its dc limit,  $\delta(f)$ . We will often use such an ideal *reference* source—a cw source with unit power output (i.e.,  $R_e(f) = \delta(f)$  and  $P_e = 1$ ).

#### 3.2 Surface Elevation

Because the sea surface is, by assumption, temporally and spatially stationary, its component waves turn out to form what is sometimes called a “free wave field” (i.e., a collection of 2-D plane waves that have no frequency or angle correlation with each other [23]). Such a surface is customarily described in terms of its frequency spectrum and its directional spectrum.

##### 3.2.1 Free-Wave Sea Surface

In a stochastic description, the complex amplitude  $u(\theta, f)$  becomes a random process. Since  $\langle u \rangle$  vanishes, the relevant statistic is the second moment

$$\Gamma_u(\theta_1, f_1, \theta_2, f_2) = \langle u^*(\theta_1, f_1) u(\theta_2, f_2) \rangle . \quad (11)$$

From the traveling-wave surface representation, Eq. (3), we have

$$\begin{aligned} \Gamma_h(\underline{r}_1, t_1, \underline{r}_2, t_2) &= \oint d\theta_1 \oint d\theta_2 \int_{-\infty}^{+\infty} df_1 \int_{-\infty}^{+\infty} df_2 \langle u^*(\theta_1, f_1) u(\theta_2, f_2) \rangle \\ &\quad \times E(-S(f_1)\underline{n}(\theta_1) \cdot \underline{r}_1 + f_1 t_1 + S(f_2)\underline{n}(\theta_2) \cdot \underline{r}_2 - f_2 t_2) \\ &= \int d^2 \underline{s}_1 d^2 \underline{s}_2 df_1 df_2 E(\cdots) \frac{\delta(s_1 - S(f_1))}{s_1} \frac{\delta(s_2 - S(f_2))}{s_2} \Gamma_u(\theta_1, f_1, \theta_2, f_2) , \end{aligned} \quad (12)$$

with  $\underline{s}_j = s_j \underline{n}(\theta_j)$  and  $(\cdots) = (\bar{s}_{12} \underline{r}_{12} + \underline{s}_{12} \bar{\underline{r}}_{12}) - (\bar{f}_{12} t_{12} + f_{12} \bar{t}_{12})$  in the second form. We are supposing that  $h(\underline{r}, t)$  is statistically stationary in  $t$ , as is commonly held to a good approximation. Consequently,  $\Gamma_h(\underline{r}_{12}, t_{12}, \bar{\underline{r}}_{12}, \bar{t}_{12})$  needs to be independent of  $\bar{t}_{12}$ , and, thus, the  $E(-f_{12} \bar{t}_{12})$  factor in the integrand cannot actually introduce any  $\bar{t}_{12}$  dependence, no matter what value  $f_{12}$  may take. In other words, there must be a  $\delta(f_{12})$  factor lurking in the moments. We are also supposing that  $h(\underline{r}, t)$  is stationary in  $\underline{r}$ . By similar reasoning, the moments must also contain the factor  $\delta(\underline{s}_{12}) = \delta(\theta_1 - \theta_2) \delta(s_1 - s_2)/s_1$ . But since we already know that a factor  $\delta(s_1 - S(f_1)) \delta(s_2 - S(f_2)) \delta(f_1 - f_2)$  is present, the only news provided by this spatial stationarity is that the moments must contain an angular singularity  $\delta(\theta_1 - \theta_2)$  as well. In other words, the traveling-wave components of the surface-wave field are uncorrelated in both frequency and azimuth (i.e., they are a free wave field). For such a field, it is not difficult to show, via the polar form  $\bar{\underline{s}}_{12} = \bar{s}_{12} \underline{n}(\bar{\theta}_{12})$ , that

$$C_h(\bar{\underline{s}}_{12}, \underline{s}_{12} \sim \underline{0}, \bar{f}_{12}) = \frac{\delta(\bar{s}_{12} - S(\bar{f}_{12}))}{\bar{s}_{12}} C_u(\bar{\theta}_{12}, \theta_{12} \sim 0, \bar{f}_{12}) . \quad (13)$$

The form and content of Eq. (13) are a direct inheritance from Eq. (4).



### 3.2.2 Surface Frequency Spectrum and Directionality

It is “customary” [24] to represent the above angle-frequency moment in the factored form<sup>4</sup>

$$C_u(\bar{\theta}_{12}, \theta_{12} \sim 0, \bar{f}_{12}) = \Phi(\bar{\omega}_{12}) \begin{cases} H(\bar{\theta}_{12}) & \cdots \bar{\omega}_{12} > 0 \\ H(\bar{\theta}_{12} + \pi) & \cdots \bar{\omega}_{12} < 0 \end{cases} , \quad (14)$$

in terms of the frequency spectrum  $\Phi$  and directional spectrum  $H$ , both of which are real and positive. We use this representation throughout the theoretical development *without* specifying any functional forms for  $\Phi$  or  $H$ .

### 3.3 Scattered Field

We turn now to the statistics of the reverberant field. For simplicity, we hereafter drop the subscript “ $A$ ” and write  $\Gamma(\cdots)$ ,  $C(\cdots)$  rather than  $\Gamma_A(\cdots)$ ,  $C_A(\cdots)$ . The modulation  $A(\vec{r}, t)$ , like the surface  $h(\underline{x}, t)$  that scatters it, is a stochastic field—a random function of space and time, albeit a complex-valued one. Our objective is to find the second moments of  $A(\vec{r}, t)$  for various  $\vec{r}$ ,  $t$ . We write the general two-point space/time moment as

$$\langle A^*(\vec{r}_1, t_1) A(\vec{r}_2, t_2) \rangle = \Gamma(\underline{r}_1, t_{12}, \underline{r}_2, \bar{t}_{12}; \underline{r}_0, z_0, z_1, z_2) , \quad (15)$$

consigning the source position  $(\underline{r}_0, z_0)$  to the list of parameters along with the receiver depths. The brackets  $\langle \rangle$  denote averaging over ensembles of both source signals and sea surfaces.

The SWHA series for  $A$  immediately yields a similar series for the second moment. With the arguments omitted for clarity, this is

$$\Gamma = \Gamma^{(0)} + \Gamma^{(1)} + \Gamma^{(2)} + \cdots . \quad (16a)$$

The  $N$ th term is  $\Gamma^{(N)} = \sum_{N \geq D \geq 0} \Gamma^{(N,D)}$ , where  $\Gamma^{(N,D)} = \Gamma^{jm} + \Gamma^{mj}$  with  $N = j + m$  and  $D = |j - m|$ , in terms of the elementary  $(j + m)$ th-order moments,

$$\Gamma^{jm} = \langle A^{(j)*} A^{(m)} \rangle . \quad (16b)$$

The terms through second order are  $\Gamma^{(0)} = \Gamma^{(0,0)}$ ,  $\Gamma^{(1)} = \Gamma^{(1,1)}$ , and  $\Gamma^{(2)} = \Gamma^{(2,0)} + \Gamma^{(2,2)}$ . Thus,

$$\Gamma^{(0)} = \Gamma^{00} \quad (17a)$$

$$\Gamma^{(1)} = \Gamma^{01} + \Gamma^{10} \quad (17b)$$

$$\Gamma^{(2)} = \Gamma^{11} + (\Gamma^{02} + \Gamma^{20}) . \quad (17c)$$

Equation (17) clearly holds in the space/frequency and wavenumber/frequency domains as well. The space/frequency version is obtained through the double transformation

$$\Gamma(\underline{r}_1, t_{12}, \underline{r}_2, \bar{t}_{12}; \cdots) \xrightarrow{t_{12} \rightarrow \bar{f}_{12}} \xrightarrow{\bar{t}_{12} \rightarrow f_{12}} \Gamma(\underline{r}_1, \bar{f}_{12}, \underline{r}_2, f_{12}; \cdots) , \quad (18)$$

which, in the time-stationary case, reduces to

$$C(\underline{r}_1, \underline{r}_2, t_{12}; \cdots) \xrightarrow{t_{12} \rightarrow \bar{f}_{12}} C(\underline{r}_1, \underline{r}_2, \bar{f}_{12}; \cdots) . \quad (19)$$

The SWHA contributions to this CSD are investigated below for orders  $N = 0, 1, 2$ . As should be expected from the symmetry of the problem, these depend on only the *relative* receiver locations,

<sup>4</sup>The positive-frequency part is Eq. (3.22) in Ref. 24, where the left-hand side would be written  $F(\bar{\omega}_{12}, \bar{\theta}_{12})$ .

$\underline{r}_{01}$ ,  $\underline{r}_{02}$  rather than on  $\underline{r}_0$ ,  $\underline{r}_1$ , and  $\underline{r}_2$ , separately. Anticipating that, we hereafter write this CSD as  $C(\underline{r}_{01}, \underline{r}_{02}, \bar{f}_{12}; \dots)$ . In a similar spirit, we often write the Green's function  $G(\vec{r}_i, \vec{r}_j)$  as  $G(\underline{r}_{ji}; z_i, z_j)$  to emphasize its dependence on the *relative* horizontal separation  $\underline{r}_{ji}$ . The main focus is on the second-order CSD, which consists of two kinds of terms:  $\langle A^{(2)*} A^{(0)} \rangle$  and  $\langle A^{(1)*} A^{(1)} \rangle$ . It turns out that the first type merely supplies a small baseband correction, while the second provides something quite different—Doppler sidebands.

### 3.3.1 Order 0

From Eq. (10a), we have

$$\Gamma^{(0)}(\underline{r}_1, t_1, \underline{r}_2, t_2; \underline{r}_0, z_0, z_1, z_2) = \langle A^{(0)*}(\vec{r}_1, t_1) A^{(0)}(\vec{r}_2, t_2) \rangle = \Gamma_e(t_1, t_2) G^*(\vec{r}_1, \vec{r}_0) G(\vec{r}_2, \vec{r}_0) . \quad (20)$$

The stationarity of  $e(t)$  converts this to

$$C^{(0)}(\underline{r}_{01}, \underline{r}_{02}, f; z_0, z_1, z_2) = C_e(f) G^*(\underline{r}_{01}; z_1, z_0) G(\underline{r}_{02}; z_2, z_0) , \quad (21)$$

which is plainly a baseband term (one whose frequency-dependence reduces to  $\delta(f)$  if the source bandwidth vanishes) consisting of the source modulation PSD modified by a pair of cw propagation factors at the carrier frequency. As anticipated, its horizontal dependence is on  $\underline{r}_{01}, \underline{r}_{02}$ .

### 3.3.2 Order 1

Because the source signal and sea surface are statistically independent, their joint moments factor  $\langle h e \rangle = \langle h \rangle \langle e \rangle$ . Since  $\langle h \rangle = 0$ ,  $\Gamma^{(1)}$  vanishes identically.

### 3.3.3 Order 2, Baseband Terms

The two terms comprising  $\Gamma^{(2,2)}$  are

$$\Gamma^{02}(\underline{r}_1, t_1, \underline{r}_2, t_2; \underline{r}_0, z_0, z_1, z_2) = \langle A^{(0)*}(\vec{r}_1, t_1) A^{(2)}(\vec{r}_2, t_2) \rangle \quad (22a)$$

$$\Gamma^{20}(\underline{r}_1, t_1, \underline{r}_2, t_2; \underline{r}_0, z_0, z_1, z_2) = \langle A^{(2)*}(\vec{r}_1, t_1) A^{(0)}(\vec{r}_2, t_2) \rangle . \quad (22b)$$

We obtain the first one in detail and then get the second by inspection. From Eq. (10),

$$\begin{aligned} \Gamma^{02}(\underline{r}_1, t_1, \underline{r}_2, t_2; \underline{r}_0, z_0, z_1, z_2) &= \langle e^*(t_1) e(t_2) \rangle G^*(\vec{r}_1, \vec{r}_0) \\ &\times \iint d^2 \underline{r}_a d^2 \underline{r}_b G_a(\vec{r}_2, \vec{r}_a) G_{ab}(\vec{r}_a, \vec{r}_b) G_b(\vec{r}_b, \vec{r}_0) \langle h(\underline{r}_a, t_1) h(\underline{r}_b, t_2) \rangle , \end{aligned} \quad (23)$$

where the two ensemble averages refer separately to the source and the sea surface. We rewrite all three moments in mean-and-difference coordinates and then invoke stationarity in time, space, or both (indicated by  $\rightsquigarrow$ ) to simplify them.

- For the source modulation,

$$\langle e^*(t_1) e(t_2) \rangle = \Gamma_e(t_1, t_2) = \Gamma_e(t_{12}, \bar{t}_{12}) \rightsquigarrow \Gamma_e(t_{12}, \bar{f}_{12}) = C_e(t_{12}) \xrightarrow{t_{12} \rightarrow f} C_e(f) .$$

- For the surface elevation,

$$\begin{aligned} \langle h(\underline{r}_a, t_a) h(\underline{r}_b, t_b) \rangle &= \Gamma_h(\underline{r}_a, t_a, \underline{r}_b, t_b) = \Gamma_h(\underline{r}_{ab}, t_{ab}, \bar{\underline{r}}_{ab}, \bar{t}_{ab}) \rightsquigarrow \Gamma_h(\underline{r}_{ab}, t_{ab}, \bar{\underline{f}}_{ab}, \bar{f}_{ab}) \\ &= \int_{-\infty}^{\infty} d\bar{f}_{ab} \oint d\bar{\theta}_{ab} E(S(\bar{f}_{ab}) \underline{n}(\bar{\theta}_{ab}) \cdot \underline{r}_{ab} - \bar{f}_{ab} t_{ab}) C_u(\bar{\theta}_{ab}, \theta_{ab} \sim 0, \bar{f}_{ab}) . \end{aligned}$$

- For the reverberation field,

$$\begin{aligned}\Gamma^{02}(\underline{\mathbf{r}}_1, t_1, \underline{\mathbf{r}}_2, t_2; \dots) &= \Gamma^{02}(\underline{\mathbf{r}}_1, t_{12}, \underline{\mathbf{r}}_2, \bar{t}_{12}; \dots) \rightsquigarrow \Gamma^{02}(\underline{\mathbf{r}}_1, t_{12}, \underline{\mathbf{r}}_2, \bar{t}_{12}; \dots) \\ &= C^{02}(\underline{\mathbf{r}}_{01}, \underline{\mathbf{r}}_{02}, t_{12}; \dots) \xrightarrow{t_{12} \rightarrow f} C^{02}(\underline{\mathbf{r}}_{01}, \underline{\mathbf{r}}_{02}, f; \dots) .\end{aligned}$$

These three expressions convert Eq. (23) into

$$\begin{aligned}C^{02}(\underline{\mathbf{r}}_{01}, \underline{\mathbf{r}}_{02}, f; z_0, z_1, z_2) &= C_e(f) G^*(\vec{\mathbf{r}}_1, \vec{\mathbf{r}}_0) \\ &\times \iint d^2 \underline{\mathbf{r}}_a d^2 \underline{\mathbf{r}}_b G_a(\vec{\mathbf{r}}_2, \vec{\mathbf{r}}_a) G_{ab}(\vec{\mathbf{r}}_a, \vec{\mathbf{r}}_b) G_b(\vec{\mathbf{r}}_b, \vec{\mathbf{r}}_0) \\ &\times \int_{-\infty}^{\infty} df' \oint d\theta E(S(f') \underline{\mathbf{n}}(\theta) \cdot \underline{\mathbf{r}}_{ab}) C_u(\theta, \theta_{ab} \sim 0, f') .\end{aligned}\quad (24)$$

As anticipated, this is another baseband term like Eq. (21), though smaller and with a more complicated spatial dependence. With a little rearrangement, it can be written as

$$\begin{aligned}C^{02}(\underline{\mathbf{r}}_{01}, \underline{\mathbf{r}}_{02}, f; z_0, z_1, z_2) &= C_e(f) G^*(\vec{\mathbf{r}}_1, \vec{\mathbf{r}}_0) \int_{-\infty}^{\infty} df' \oint d\theta C_u(\theta, \theta_{ab} \sim 0, f') \\ &\times [L(\underline{\mathbf{s}}, \underline{\mathbf{r}}_{02}; z_0, z_2)]_{\underline{\mathbf{s}}=S(f') \underline{\mathbf{n}}(\theta)} ,\end{aligned}\quad (25)$$

in terms of the mean-sea-surface fundamental integral,

$$L(\underline{\mathbf{s}}, \underline{\mathbf{r}}_{02}; z_0, z_2) = \int d^2 \underline{\mathbf{r}}_b G_b(\underline{\mathbf{r}}_{0b}; z_b, z_0) J(\underline{\mathbf{s}}, \underline{\mathbf{r}}_{b2}; z_2) ,\quad (26)$$

in which  $J$  is the convolution

$$J(\underline{\mathbf{s}}, \underline{\mathbf{r}}; z) = G_{ab}(\underline{\mathbf{s}}; z_a, z_b) \overset{\circ}{\star} \{E(-\underline{\mathbf{s}} \cdot \underline{\mathbf{r}}) G_a(\underline{\mathbf{s}}; z, z_a)\} .\quad (27)$$

$C^{20}(\underline{\mathbf{r}}_{01}, \underline{\mathbf{r}}_{02}, f; z_0, z_1, z_2)$  comes from Eq. (22b) by the same process. Details are omitted. Instead, both terms are summarized in Section 3.4.

### 3.3.4 Order 2, Sideband Terms

The only term contributing to  $\Gamma^{(2,0)}$  is  $\Gamma^{11}$ . Thus,

$$\begin{aligned}\Gamma^{(2,0)}(\underline{\mathbf{r}}_1, t_1, \underline{\mathbf{r}}_2, t_2; \underline{\mathbf{r}}_0, z_0, z_1, z_2) &= \Gamma_e(t_1, t_2) \iint d^2 \underline{\mathbf{r}}_a d^2 \underline{\mathbf{r}}_b G_a^*(\underline{\mathbf{r}}_{a1}; z_1, z_a) G_a^*(\underline{\mathbf{r}}_{0a}; z_a, z_0) \\ &\times G_b(\underline{\mathbf{r}}_{b2}; z_2, z_b) G_b(\underline{\mathbf{r}}_{0b}; z_b, z_0) \Gamma_h(\underline{\mathbf{r}}_a, t_1, \underline{\mathbf{r}}_b, t_2) .\end{aligned}\quad (28)$$

In mean-and-difference time coordinates this can be written as

$$\Gamma^{(2,0)}(\underline{\mathbf{r}}_1, t_{12}, \underline{\mathbf{r}}_2, \bar{t}_{12}; \dots) = \Gamma_e(t_{12}, \bar{t}_{12}) \mathcal{L} \Gamma_h(\underline{\mathbf{r}}_a, t_{12}, \underline{\mathbf{r}}_b, \bar{t}_{12}) ,$$

in which  $\mathcal{L}$  represents the integral operator and the ellipsis stands for the parameters  $\underline{\mathbf{r}}_0, z_0, z_1, z_2$ . The stationarity of the source implies  $\Gamma_e(t_{12}, \bar{t}_{12}) = C_e(t_{12})$ , the stationarity of the sea surface implies  $\Gamma_h(\underline{\mathbf{r}}_a, t_{12}, \underline{\mathbf{r}}_b, \bar{t}_{12}) = C_h(\underline{\mathbf{r}}_a, \underline{\mathbf{r}}_b, t_{12})$ , and together they imply that  $A^{(1)}(\vec{\mathbf{r}}, t)$  is stationary in time and that  $\Gamma^{(2,0)}(\underline{\mathbf{r}}_1, t_{12}, \underline{\mathbf{r}}_2, \bar{t}_{12}; \dots) = C^{(2,0)}(\underline{\mathbf{r}}_{01}, \underline{\mathbf{r}}_{02}, t_{12}; \dots)$ . In the frequency domain, therefore,

$$C^{(2,0)}(\underline{\mathbf{r}}_{01}, \underline{\mathbf{r}}_{02}, f; z_0, z_1, z_2) = C_e(f) \overset{f}{\star} C_{\text{ref}}^{(2,0)}(\underline{\mathbf{r}}_{01}, \underline{\mathbf{r}}_{02}, f; z_0, z_1, z_2) \quad (29)$$

in which the source PSD is convolved with the reference CSD (Section 3.1),

$$\begin{aligned}C_{\text{ref}}^{(2,0)}(\underline{\mathbf{r}}_{01}, \underline{\mathbf{r}}_{02}, f; z_0, z_1, z_2) &= \\ \iint d^2 \underline{\mathbf{r}}_a d^2 \underline{\mathbf{r}}_b G_a^*(\underline{\mathbf{r}}_{a1}; z_1, z_a) \left\{ G_a^*(\underline{\mathbf{r}}_{0a}; z_a, z_0) C_h(\underline{\mathbf{r}}_{ab}, \bar{\mathbf{r}}_{ab}, f) G_b(\underline{\mathbf{r}}_{0b}; z_b, z_0) \right\} G_b(\underline{\mathbf{r}}_{b2}; z_2, z_b) .\end{aligned}\quad (30)$$

Equation (29) is *not* a baseband term: its frequency-dependence does not reduce to  $\delta(f)$  in the limit of a cw source.

For a *passive* ASW problem with the sea surface acting as the *primary* acoustic source, the curly brackets in the integrand above would contain nothing but the boundary source CSD [11, Eq. (3.19)]. Thus Eq. (30) would reduce to a form of the van Cittert-Zernike theorem from partial coherence theory [9, Section 10.4.2], which gives the CSD within a volume in terms of its values on the bounding surface. This is often a convenient starting point for passive problems (e.g., the Kuperman and Ingenito treatment of the ambient noise field generated by the sea surface itself [25, Eq. (7)]). In the *active* problem, the sea surface is a *secondary* source—a scatterer. Rather than that simple boundary value, the curly brackets contain (a) two Green’s functions that propagate the signal from the primary source to a pair of surface points and (b) a wave-height CSD that embodies the sea-surface correlation. In that sense, Eq. (30) is a perturbative generalization of the van Cittert-Zernike theorem to active scattering from a time-dependent surface.

Further reduction of Eq. (30) is possible when  $C_h$  in the integrand is examined in the wavenumber domain. Generally,  $C_h(\underline{r}_{ab}, \bar{\underline{r}}_{ab}, f) \xrightarrow{\underline{r}_{ab} \rightarrow \bar{\underline{s}}_{ab}} \bar{\underline{r}}_{ab} \xrightarrow{\bar{\underline{s}}_{ab}} C_h(\bar{\underline{s}}_{ab}, \underline{s}_{ab}, f)$ ; however, when  $h$  is spatially stationary (i.e., when  $C_h(\bar{\underline{s}}_{ab}, \underline{s}_{ab}, f) \approx C_h(\bar{\underline{s}}_{ab}, \underline{s}_{ab} \sim \underline{0}, f) \delta(\underline{s}_{ab})$ ) this reduces to  $C_h(\underline{r}_{ab}, \bar{\underline{r}}_{ab}, f) = \int d^2 \bar{\underline{s}}_{ab} E(\bar{\underline{s}}_{ab} \cdot \underline{r}_{ab}) C_h(\bar{\underline{s}}_{ab}, \underline{s}_{ab} \sim \underline{0}, f)$ . Then Eq. (30) becomes

$$C_{\text{ref}}^{(2,0)}(\underline{r}_{01}, \underline{r}_{02}, f; z_0, z_1, z_2) = \int d^2 \bar{\underline{s}}_{ab} M_1^* M_2 C_h(\bar{\underline{s}}_{ab}, \underline{s}_{ab} \sim \underline{0}, f)$$

in terms of the surface integral  $M_\ell = \int d^2 \underline{r}_c E(\bar{\underline{s}}_{ab} \cdot \underline{r}_c) G_c(\underline{r}_{c\ell}; z_\ell, z_c) G_c(\underline{r}_{0c}; z_c, z_0)$ . It is a simple matter to express the latter as  $M_\ell = E(\bar{\underline{s}}_{ab}, \underline{r}_0) N_\ell$  in which  $N_\ell$  is a spatial convolution which becomes a simple product in the wavenumber domain:

$$N_\ell = E(\bar{\underline{s}}_{ab}, \underline{r}_{0\ell}) G_c(\underline{r}_{0\ell}; z_c, z_0) \star^{\underline{r}_{0\ell}} G_c(\underline{r}_{0\ell}; z_\ell, z_c) \xrightarrow{\underline{r}_{0\ell} \rightarrow \bar{\underline{s}}_{0\ell}} G_c(\bar{\underline{s}}_{0\ell} - \bar{\underline{s}}_{ab}; z_c, z_0) G_c(\bar{\underline{s}}_{0\ell}; z_\ell, z_c) .$$

Thus, for any real  $f$ , whether positive or negative, Eq. (30) becomes

$$C_{\text{ref}}^{(2,0)}(\underline{r}_{01}, \underline{r}_{02}, f; z_0, z_1, z_2) = \int d^2 \bar{\underline{s}}_{ab} C_h(\bar{\underline{s}}_{ab}, \underline{s}_{ab} \sim \underline{0}, f) I^*(\bar{\underline{s}}_{ab}, \underline{r}_{01}; z_0, z_1) I(\bar{\underline{s}}_{ab}, \underline{r}_{02}; z_0, z_2)$$

in which

$$I(\underline{s}, \underline{r}; z_0, z) = \int d^2 \underline{\sigma} E(\underline{\sigma} \cdot \underline{r}) G_\alpha(\underline{\sigma} - \underline{s}; z_\alpha, z_0) G_\alpha(\underline{\sigma}; z, z_\alpha) . \quad (31)$$

Using Eq. (13), the  $C_h$  factor can be expressed as an angle/frequency moment and, when that moment has the factored form of Eq. (14), the result is

$$C_{\text{ref}}^{(2,0)}(\underline{r}_{01}, \underline{r}_{02}, \pm|f|; z_0, z_1, z_2) = \Phi(|\omega|) \oint d\theta H(\theta) [I^*(\underline{s}, \underline{r}_{01}; z_0, z_1) I(\underline{s}, \underline{r}_{02}; z_0, z_2)]_{\underline{s}=\pm S(|f|)\underline{n}(\theta)} , \quad (32)$$

an expression with explicit upshifted and downshifted Doppler sidebands.

Equations (31) and (32) should prove computationally useful whenever the Green’s function is simple enough for the  $I$  terms to be evaluated analytically since that would leave only a single angular integration to be done numerically. This plan is pursued in Section 4, with the ocean modeled as a uniform half-space. But first, the results are gathered and summarized in Section 3.4, using the familiar “ $k$ - $\omega$ ” notation.

### 3.4 Summary of the Reverberation CSD

We have found that the reverberation CSD assumes the form

$$C(\underline{\mathbf{r}}_{01}, \underline{\mathbf{r}}_{02}, f; z_0, z_1, z_2) = C_e(f) \star C_{\text{ref}}(\underline{\mathbf{r}}_{01}, \underline{\mathbf{r}}_{02}, f; z_0, z_1, z_2) \quad (33)$$

because the sea surface and the source are temporally stationary. We focus on  $C_{\text{ref}}$  since the PSD for any narrowband source can always be included later by convolution. From the angular singularity in  $C_h$  (a consequence of the spatial stationarity of  $h$ ), the angle-frequency factorization *ansatz* for  $C_u$  (Eq. (14)), and the horizontal invariance of the subsurface medium, we have seen that  $C_{\text{ref}}$  has the structure outlined below through second order in the SWHA.

#### 3.4.1 Baseband

There is a zeroth-order baseband component,

$$C_{\text{ref}}^{(0)}(\underline{\mathbf{r}}_{01}, \underline{\mathbf{r}}_{02}, f; z_0, z_1, z_2) = \delta(f) G^*(\underline{\mathbf{r}}_{01}; z_1, z_0) G(\underline{\mathbf{r}}_{02}; z_2, z_0) . \quad (34)$$

There is also a pair of second-order baseband contributions:

$$\begin{aligned} C_{\text{ref}}^{02}(\underline{\mathbf{r}}_{01}, \underline{\mathbf{r}}_{02}, f; z_0, z_1, z_2) &= \delta(f) G^*(\vec{\mathbf{r}}_1, \vec{\mathbf{r}}_0) \int_{-\infty}^{\infty} df' \oint d\theta C_u(\theta, \theta_{ab} \sim 0, f') \\ &\quad \times [L(\underline{\mathbf{K}}, \underline{\mathbf{r}}_{02}; z_0, z_2)]_{\underline{\mathbf{K}}=K(\omega')\underline{\mathbf{n}}(\theta)} \end{aligned} \quad (35a)$$

$$\begin{aligned} C_{\text{ref}}^{20}(\underline{\mathbf{r}}_{01}, \underline{\mathbf{r}}_{02}, f; z_0, z_1, z_2) &= \delta(f) G(\vec{\mathbf{r}}_2, \vec{\mathbf{r}}_0) \int_{-\infty}^{\infty} df' \oint d\theta C_u(\theta, \theta_{ab} \sim 0, f') \\ &\quad \times [L^*(\underline{\mathbf{K}}, \underline{\mathbf{r}}_{01}; z_0, z_1)]_{\underline{\mathbf{K}}=K(\omega')\underline{\mathbf{n}}(\theta+\pi)} , \end{aligned} \quad (35b)$$

in which

$$L(\underline{\mathbf{K}}, \underline{\mathbf{r}}_{0\ell}; z_0, z_\ell) = \int d^2 \underline{\mathbf{r}}_b G_b(\underline{\mathbf{r}}_{0b}; z_b, z_0) J(\underline{\mathbf{K}}, \underline{\mathbf{r}}_{b\ell}; z_\ell) \quad (36)$$

and

$$J(\underline{\mathbf{K}}, \underline{\mathbf{r}}; z) = \frac{1}{(2\pi)^2} \int d^2 \underline{\mathbf{k}} e^{+i(\underline{\mathbf{k}}-\underline{\mathbf{K}})\cdot\underline{\mathbf{r}}} G_{ab}(\underline{\mathbf{k}}; z_a, z_b) G_a(\underline{\mathbf{K}}-\underline{\mathbf{k}}; z, z_a) . \quad (37)$$

#### 3.4.2 Sidebands

Nonbaseband contributions emerge at second order as a pair of Doppler sidebands,

$$\begin{aligned} C_{\text{ref}}^{(2,0)}(\underline{\mathbf{r}}_{01}, \underline{\mathbf{r}}_{02}, \pm|f|; z_0, z_1, z_2) &= \Phi(|\omega|) \oint d\theta H(\theta) \\ &\quad \times [e^{i\underline{\mathbf{r}}_{12}\cdot\underline{\mathbf{K}}/2} I^*(\underline{\mathbf{K}}, \underline{\mathbf{r}}_{01}; z_0, z_1) I(\underline{\mathbf{K}}, \underline{\mathbf{r}}_{02}; z_0, z_2)]_{\underline{\mathbf{K}}=\pm K\underline{\mathbf{n}}(\theta)} \\ &\quad \cdots |\omega| = \Omega(K), \quad K \geq 0 \end{aligned} \quad (38)$$

in which

$$I(\underline{\mathbf{K}}, \underline{\mathbf{r}}; z_0, z) = \frac{1}{(2\pi)^2} \int d^2 \underline{\mathbf{k}} e^{i\underline{\mathbf{k}}\cdot\underline{\mathbf{r}}} G_\alpha(\underline{\mathbf{k}} - \underline{\mathbf{K}}/2; z_\alpha, z_0) G_\alpha(\underline{\mathbf{k}} + \underline{\mathbf{K}}/2; z, z_\alpha) . \quad (39)$$

Since the wavevector in Eq. (38) is restricted to  $\underline{\mathbf{K}} = +K\underline{\mathbf{n}}(\theta)$  and  $\underline{\mathbf{K}} = -K\underline{\mathbf{n}}(\theta)$ , each surface wavenumber  $K > 0$  contributes explicitly to both the upper ( $+|\omega|$ ) and lower ( $-|\omega|$ ) sidebands. For each  $K$ , Eq. (38) is evaluated by integrating over azimuth and then assigning the result to the proper Doppler-shifted frequency,  $\pm|f|$ .

In Eqs. (34–39) we have concise expressions, valid through second order in the SWHA, for the baseband and sideband parts of the reverberation CSD. The zeroth-order baseband term does not relate to the sea state at all. The second-order baseband and sideband terms do involve the sea surface, but in different ways. The baseband term only depends on the average surface roughness, which is constant in time, whereas the sideband term involves the full surface dispersion relation. (In photographic terms, a snapshot could determine the baseband, but the sideband would require a movie.) The remaining task is to determine the  $\underline{K}$  dependence of the fundamental integrals  $L$  for the baseband and  $I$  for the sidebands. The following section does this for an ocean modeled as a uniform half-space.

#### 4. SHALLOW DEPLOYMENT IN A UNIFORM OCEAN

The CSD expressions obtained above will now be evaluated assuming a uniform ocean and a geometry in which all the depths are much smaller than the source-receiver ranges ( $z_0, z_1, z_2 \ll r_{01}, r_{02}$ )—a case that retains considerable operational relevance while remaining analytically tractable. The  $\ell$ th receiver's horizontal displacement from the source is written  $\underline{r}_{0\ell} = r_{0\ell} \underline{n}(\theta_\ell)$ , and its azimuth  $\theta_\ell$  serves as a convenient reference for surface waves,  $\vartheta_\ell = \theta - \theta_\ell$  (e.g., in  $\underline{n}(\theta) \cdot \underline{n}(\theta_\ell) = \cos \vartheta_\ell$ ).

##### 4.1 Green's Function

For an ocean modelled as a uniform half-space beneath a pressure-release plane, the Green's function is a sum of source and image-source terms:

$$G(\underline{r}; z, z') = \frac{e^{ik_0 \sqrt{r^2 + (z' - z)^2}}}{4\pi \sqrt{r^2 + (z' - z)^2}} - \frac{e^{ik_0 \sqrt{r^2 + (z' + z)^2}}}{4\pi \sqrt{r^2 + (z' + z)^2}}. \quad (40)$$

In the horizontal wavenumber domain, this becomes

$$G(\underline{k}; z, z') = \frac{e^{i\kappa(k_0, k)|z' - z|}}{2i\kappa(k_0, k)} - \frac{e^{i\kappa(k_0, k)|z' + z|}}{2i\kappa(k_0, k)}, \quad (41)$$

whose terms correspond to propagation with 3-D wavevectors  $\vec{k} = \underline{k} + \kappa \vec{e}_z$  and  $\vec{k} = \underline{k} - \kappa \vec{e}_z$ . These wavevectors' magnitudes and those of their horizontal and vertical components are, respectively,  $k_0 = |\vec{k}| = \omega_0/c_0$ ,  $k = |\underline{k}|$ , and  $\kappa(k_0, k) = \sqrt{k_0^2 - k^2}$ . The surface normal derivatives are simply  $G_a(\underline{k}; z_b, z_a) = e^{i\kappa(k_0, k)z_b}$ ,  $G_b(\underline{k}; z_b, z_a) = e^{i\kappa(k_0, k)z_a}$ , and  $G_{ab}(\underline{k}; z_b, z_a) = i\kappa(k_0, k)$ .

##### 4.2 Baseband, Order 0

For shallow deployment ( $z_\ell, z_0 \ll r_{0\ell}$ ), the Green's function becomes

$$G(\underline{r}_{0\ell}; z_\ell, z_0) \approx \frac{e^{ik_0 r_{0\ell}}}{2\pi i r_{0\ell}} \sin\left(k_0 z_0 \frac{z_\ell}{r_{0\ell}}\right) \quad \dots \quad \ell = 1, 2, \quad (42)$$

and this reduces the zeroth-order baseband component Eq.(34) to

$$C_{\text{ref}}^{(0)}(\underline{r}_{01}, \underline{r}_{02}, f; z_0, z_1, z_2) \approx \delta(f) \frac{e^{ik_0(r_{02} - r_{01})}}{4\pi^2 r_{01} r_{02}} \sin\left(k_0 z_0 \frac{z_1}{r_{01}}\right) \sin\left(k_0 z_0 \frac{z_2}{r_{02}}\right). \quad (43)$$

As should be expected, this depends on the magnitudes of  $\underline{r}_{01}, \underline{r}_{02}$ , but not on their directions.

### 4.3 Baseband, Order 2

#### 4.3.1 Fundamental Integral

In this environment, Eq. (37) reduces to

$$J(\underline{K}, \underline{r}; z) = \frac{i}{(2\pi)^2} \int d^2 \underline{k} \kappa(k_0, k) e^{i\{(\underline{k}-\underline{K}) \cdot \underline{r} + \kappa(k_0, |\underline{k}-\underline{K}|)z\}}$$

so that, through Eq. (36) with the integration variable shifted from  $\underline{r}_b$  to  $\underline{r}_{b\ell}$ ,  $L$  becomes

$$L(\underline{K}, \underline{r}_{0\ell}; z_0, z_\ell) = \frac{i}{(2\pi)^2} \int d^2 \underline{k} \kappa(k_0, k) e^{i\kappa(k_0, |\underline{k}-\underline{K}|)z_\ell} \int d^2 \underline{r}_{b\ell} G_b(\underline{r}_{b\ell} - \underline{r}_{0\ell}; z_b, z_0) e^{-i(\underline{K}-\underline{k}) \cdot \underline{r}_{b\ell}} . \quad (44)$$

The spatial integral in this is  $e^{i(\underline{k}-\underline{K}) \cdot \underline{r}_{0\ell}} e^{i\kappa(k_0, |\underline{k}-\underline{K}|)z_0}$ , so the fundamental integral is just

$$L(\underline{K}, \underline{r}_{0\ell}; z_0, z_\ell) = \frac{i}{(2\pi)^2} \int d^2 \underline{k} \kappa(k_0, k) e^{i\Psi(\underline{k}, \underline{K}, k_0; \underline{r}_{0\ell}, z_0, z_\ell)} , \quad (45)$$

a 2-D wavenumber integral whose integrand has amplitude  $\kappa(k_0, k)$  and phase

$$\Psi(\underline{k}, \underline{K}, k_0; \underline{r}_{0\ell}, z_0, z_\ell) = (\underline{k} - \underline{K}) \cdot \underline{r}_{0\ell} + \kappa(k_0, |\underline{k} - \underline{K}|)(z_0 + z_\ell) .$$

#### 4.3.2 Stationary-Phase Evaluation

The shallow-deployment conditions, essentially

$$\epsilon \stackrel{def}{=} \bar{z}_{0\ell}/r_{0\ell} \ll 1 ,$$

facilitate applying the stationary-phase method to estimate  $L$ . First, the result with  $\underline{K} = K\underline{n}(\theta)$  and  $\ell = 2$  (for Eq. (35a)) is found explicitly. The result with  $\underline{K} = K\underline{n}(\theta + \pi)$  and  $\ell = 1$  (for Eq. (35b)) is obtained by inspection. To simplify the process, we introduce the dimensionless variables

$$\underline{\mu} = \underline{k}/k_0 \quad \underline{\nu} = \underline{K}/2k_0 \quad \psi = \Psi/k_0 r_{0\ell} \quad (46)$$

and the function  $\gamma(x) = \sqrt{1-x^2}$ . With these,  $L$  can be expressed (with the dependence on everything but  $\underline{\mu}, \underline{\nu}$  left implicit) as

$$L(\underline{\nu}) = ik_0 \left( \frac{k_0}{2\pi} \right)^2 \int d^2 \underline{\mu} \gamma(|\underline{\mu}|) e^{ik_0 r_{0\ell} \psi(\underline{\mu}, \underline{\nu})} \quad (47)$$

where

$$\psi(\underline{\mu}, \underline{\nu}) = (\underline{\mu} - 2\underline{\nu}) \cdot \underline{n}(\theta_\ell) + \gamma(|\underline{\mu} - 2\underline{\nu}|)2\epsilon . \quad (48)$$

Under the innocuous assumption that many wavelengths separate the source from the receiver (i.e., that  $k_0 r_{0\ell} \gg 1$ ) the stationary-phase estimate is

$$L(\underline{\nu}) \approx ik_0 \left( \frac{k_0}{4\pi r_{0\ell}} \right) \sum_{\underline{\sigma}} \gamma(|\underline{\sigma}|) \left| \det \underline{\underline{M}}(\underline{\sigma}, \underline{\nu}) \right|^{-1/2} e^{ik_0 r_{0\ell} \psi(\underline{\sigma}, \underline{\nu})} \quad (49)$$

in which the  $\underline{\sigma}$  are the stationary-phase points (i.e., points where  $\psi$  is real and  $\partial\psi/\partial\underline{\mu}$  vanishes), and  $\underline{\underline{M}}(\underline{\mu}, \underline{\nu}) = -\partial^2\psi(\underline{\mu}, \underline{\nu})/\partial\underline{\mu}\partial\underline{\mu}$  is the phase curvature tensor. To evaluate  $L$  for a particular

$\underline{\nu}$ , one must first find each  $\underline{\sigma}$ , then evaluate the amplitude factors  $\gamma(|\underline{\sigma}|)$  and  $\det \underline{\underline{M}}(\underline{\sigma}, \underline{\nu})$  and the phase  $\psi(\underline{\sigma}, \underline{\nu})$ . It is a straightforward, though tedious, calculation to do this exactly. We omit the details and note these approximations for  $\epsilon \ll 1$ :

$$\begin{aligned} \underline{\sigma} &= 2\underline{n}(\theta) + (1 - 2\epsilon^2)\underline{n}(\theta_\ell) + O(\epsilon^4) & \gamma(|\underline{\sigma}|) &= 2i\sqrt{1 + \cos \vartheta_\ell} + O(\epsilon^2) \\ \left| \det \underline{\underline{M}}(\underline{\sigma}, \underline{\nu}) \right|^{-1/2} &= 2\epsilon + O(\epsilon^3) & k_0 r_{0\ell} \psi(\underline{\sigma}, \underline{\nu}) &= k_0 r_{0\ell} + O(\epsilon^2) \end{aligned} \quad ,$$

so that the stationary-phase estimate is

$$L(\underline{\nu}) = -\frac{k_0^2 \bar{z}_{0\ell}}{\pi r_{0\ell}^2} \sqrt{1 + \cos \vartheta_\ell} e^{+ik_0 r_{0\ell}} .$$

No summation is needed because there is only one stationary point for each  $\underline{\nu}$ .

The above result gets used as-is with  $\ell = 2$  in Eq. (35a) and with  $\ell = 1$  and  $\theta \rightarrow \theta + \pi$  in Eq. (35b). The factors needed are, respectively,

$$[L(\underline{K}, \underline{r}_{02}; z_0, z_2)]_{\underline{K}=K(\omega')\underline{n}(\theta)} \approx -\frac{k_0^2 \bar{z}_{02}}{\pi r_{02}^2} \sqrt{1 + \cos \vartheta_2} e^{+ik_0 r_{02}} \quad (50a)$$

$$[L^*(\underline{K}, \underline{r}_{01}; z_0, z_1)]_{\underline{K}=K(\omega')\underline{n}(\theta+\pi)} \approx -\frac{k_0^2 \bar{z}_{01}}{\pi r_{01}^2} \sqrt{1 - \cos \vartheta_1} e^{-ik_0 r_{01}} . \quad (50b)$$

Although evaluation with  $|\underline{K}| = K(\omega')$  is called for, it is actually unnecessary; the outcome depends on  $\underline{K}$ 's direction but not its magnitude.

#### 4.3.3 CSD Estimate

With Eq. (50) for the  $L$  factors, with Eq. (42) for the remaining Green's functions, and with Eqs. (14) and (104) to simplify the angle and frequency integrals, Eq. (35) reduces to

$$C_{\text{ref}}^{02}(\underline{r}_{01}, \underline{r}_{02}, f; z_0, z_1, z_2) = -\delta(f) \frac{ie^{ik_0(r_{02}-r_{01})}}{4\pi^2 r_{01} r_{02}} \frac{2(k_0 h_{\text{rms}})^2}{\pi} \times \frac{\bar{z}_{02}}{r_{02}} \sin\left(k_0 z_0 \frac{z_1}{r_{01}}\right) W(\theta_2) \quad (51a)$$

$$C_{\text{ref}}^{20}(\underline{r}_{01}, \underline{r}_{02}, f; z_0, z_1, z_2) = +\delta(f) \frac{ie^{ik_0(r_{02}-r_{01})}}{4\pi^2 r_{01} r_{02}} \frac{2(k_0 h_{\text{rms}})^2}{\pi} \times \frac{\bar{z}_{01}}{r_{01}} \sin\left(k_0 z_0 \frac{z_2}{r_{02}}\right) W(\theta_1) , \quad (51b)$$

in terms of the azimuth integral

$$W(\theta_\ell) = \oint d\theta H(\theta) \times \frac{1}{2} \left( \sqrt{1 + \cos(\theta - \theta_\ell)} + \sqrt{1 - \cos(\theta - \theta_\ell)} \right) . \quad (52)$$

#### 4.4 Baseband Summary

The full baseband result through second order is  $C_{\text{ref}}^{00} + C_{\text{ref}}^{20} + C_{\text{ref}}^{02}$ , which can be written as

$$C_{\text{ref}}(\underline{r}_{01}, \underline{r}_{02}, f; z_0, z_1, z_2) = \delta(f) Q(\underline{r}_{01}, z_0, z_1) Q^*(\underline{r}_{02}, z_0, z_2) \quad (53)$$

in which<sup>5</sup>

$$Q(\underline{r}_{0\ell}, z_0, z_\ell) = \frac{e^{-ik_0 r_{0\ell}}}{2\pi r_{0\ell}} \left[ \underbrace{\sin\left(k_0 z_0 \frac{z_\ell}{r_{0\ell}}\right)}_{\sim 1} + i \underbrace{\frac{\bar{z}_{0\ell}}{r_{0\ell}}}_{\ll 1} \underbrace{8\pi \left(\frac{h_{\text{rms}}}{\lambda_0}\right)^2}_{\sim 1} \underbrace{W(\theta_\ell)}_{\sim 1} \right] . \quad (54)$$

<sup>5</sup>The relative sizes indicated below the factors in Eq. (54) have been exploited in rewriting the expression according to the pattern  $(s_1 s_2 - i\epsilon_2 X_2 s_1 + i\epsilon_1 X_1 s_2) = (s_1 + i\epsilon_1 X_1)(s_2 + i\epsilon_2 X_2)^* + O(\epsilon^2)$  for  $s_\ell, X_\ell \sim 1, \epsilon_\ell \ll 1$ . Figure 8 shows both  $H(\theta)$  and the geometric factor multiplying it in the integrand of Eq. (52). That figure confirms that  $W(\theta_\ell) \sim 1$ . It is easily verified that  $8\pi(h_{\text{rms}}/\lambda_0)^2 \sim 1$  for  $f_0 < 300\text{Hz}$ ,  $U < 20\text{m/s}$ .



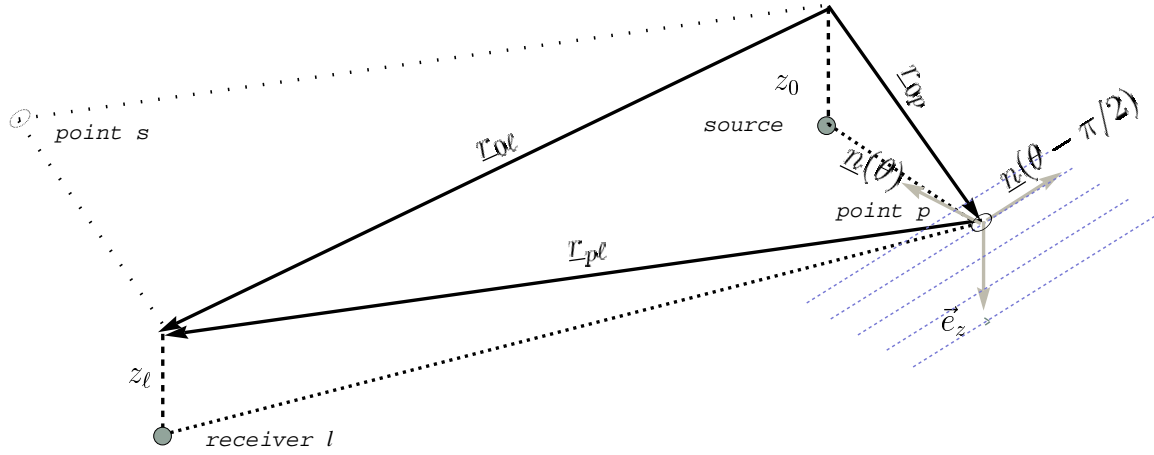


Fig. 1 — Bragg scattering at surface point  $p$  by a surface wave component with wavevector  $\underline{K} = \pm K \underline{n}(\theta)$ . The parallel dashed lines representing the wave crests are spaced  $\Lambda = 2\pi/K$  apart. The symmetric surface point  $s$  is shown.

#### 4.5 Sidebands, Fundamental Integral

With the Green's function of Eq. (41), the fundamental sideband integral Eq. (39) becomes

$$I(\underline{K}, \underline{r}_{0\ell}; z_0, z_\ell) = \frac{1}{(2\pi)^2} \int d^2 \underline{k} \exp \{ i \Psi(\underline{k}, \underline{K}, k_0; \underline{r}_{0\ell}, z_0, z_\ell) \} \quad \cdots \quad \ell = 1, 2, \quad (55)$$

whose integrand has unit amplitude and phase

$$\Psi(\underline{k}, \underline{K}, k_0; \underline{r}_{0\ell}, z_0, z_\ell) = \underline{k} \cdot \underline{r}_{0\ell} + \kappa(k_0, |\underline{k} - \frac{1}{2}\underline{K}|) z_0 + \kappa(k_0, |\underline{k} + \frac{1}{2}\underline{K}|) z_\ell \quad (56)$$

for any surface wavevector  $\underline{K}$ . To estimate  $I(\underline{K}, \cdots)$  for a given geometry, we will need to determine the range of  $\underline{K}$  in which stationary-phase  $\underline{k}$ 's arise and what their values are.

Before embarking on that, it seems advisable to review the physical significance of the stationary-phase condition. Stationarity (i.e.,  $\partial \Psi(\underline{k}, \cdots) / \partial \underline{k} = \underline{0}$ ) amounts to

$$\underline{r}_{0\ell} = z_0 \frac{\underline{k} - \frac{1}{2}\underline{K}}{\kappa(k_0, |\underline{k} - \frac{1}{2}\underline{K}|)} + z_\ell \frac{\underline{k} + \frac{1}{2}\underline{K}}{\kappa(k_0, |\underline{k} + \frac{1}{2}\underline{K}|)} . \quad (57)$$

Any  $\underline{k}$  that solves this for the prevailing  $\underline{K}$  can be used to define a point  $p$  on the sea surface via  $\underline{r}_{0\ell} = \underline{r}_{0p} + \underline{r}_{p\ell}$  (see Fig. 1) with

$$\frac{\underline{r}_{0p}}{z_0} = \frac{\underline{k} - \frac{1}{2}\underline{K}}{\kappa(k_0, |\underline{k} - \frac{1}{2}\underline{K}|)} \quad \text{and} \quad \frac{\underline{r}_{p\ell}}{z_\ell} = \frac{\underline{k} + \frac{1}{2}\underline{K}}{\kappa(k_0, |\underline{k} + \frac{1}{2}\underline{K}|)} . \quad (58)$$

In plane-wave terms, these correspond to propagation *to* and *from*  $p$  with the 3-D wavevectors

$$\vec{k}_{\text{to}} = (\underline{k} - \frac{1}{2}\underline{K}) + \kappa(k_0, |\underline{k} - \frac{1}{2}\underline{K}|) \vec{e}_z \quad \text{and} \quad \vec{k}_{\text{from}} = (\underline{k} + \frac{1}{2}\underline{K}) + \kappa(k_0, |\underline{k} + \frac{1}{2}\underline{K}|) \vec{e}_z . \quad (59)$$

Upon redirection at  $p$ , the wavevector changes by

$$\Delta \vec{k} \stackrel{\text{def}}{=} \vec{k}_{\text{from}} - \vec{k}_{\text{to}} = \underline{K} + \{ \kappa(k_0, |\underline{k} + \frac{1}{2}\underline{K}|) + \kappa(k_0, |\underline{k} - \frac{1}{2}\underline{K}|) \} \vec{e}_z . \quad (60)$$

Because of energy conservation, we have

$$|\vec{k}_{\text{to}}| = |\vec{k}_{\text{from}}| = k_0 . \quad (61a)$$

Furthermore, for  $\underline{K} = \pm K \underline{n}(\theta)$ , one finds from Eq. (60) that

$$\Delta \vec{k} \cdot \underline{n}(\theta \pm \frac{1}{2}\pi) = 0, \quad |\Delta \vec{k} \cdot \underline{n}(\theta)| = K . \quad (61b)$$

Equation (61) is precisely the condition for the signal to travel from the source to receiver  $\ell$  by first-order Bragg scattering from the surface wave with wavevector  $\underline{K}$  at point  $p$  on the sea surface. If the values of  $\underline{r}_{0p}$  and  $\underline{r}_{p\ell}$  are swapped, the same surface wave scatters the signal from a point  $s$  located at  $\underline{r}_{0s} = \underline{r}_{p\ell}$  and  $\underline{r}_{s\ell} = \underline{r}_{0p}$ . These points  $p, s$  lie on the port and starboard sides of the “heading”  $\underline{r}_{0\ell}$ . In Fig. 1, they are the vertices of the parallelogram that lie on opposite sides of the diagonal  $\underline{r}_{0\ell}$ .

Stationary-phase estimates of  $I(\underline{K}, \dots)$  for the wavevectors  $\underline{K} = \pm K \underline{n}(\theta)$  provide the up/down-Doppler sidebands  $\pm|f|$  in Eq. (38) that stem from first-order Bragg surface scattering. Equation (55) is evaluated next, and the result is used to determine the CSD contribution.

#### 4.6 Sidebands, Stationary-Phase Evaluation

This section develops the stationary-phase estimate for the fundamental sideband integral  $I(\underline{K}, \underline{r}_{0\ell}; z_0, z_\ell)$  in Eq. (55). The procedure is like the one in the baseband case but necessarily more complicated. Two separate depth/range parameters are involved,

$$\delta_\ell = \frac{z_0}{r_{0\ell}} , \quad \epsilon_\ell = \frac{z_\ell}{r_{0\ell}} \quad \text{with} \quad \nu_\ell = \max(\epsilon_\ell, \delta_\ell) , \quad (62)$$

and we are still concerned with shallow deployment,  $\nu_\ell \ll 1$ .

In terms of the dimensionless  $\underline{\mu}, \underline{\nu}$  and  $\psi$  from Eq. (46), the integral at issue has the form

$$I(\underline{\nu}) = \left( \frac{k_0}{2\pi} \right)^2 \int d^2 \underline{\mu} e^{ik_0 r_{0\ell} \psi(\underline{\mu}, \underline{\nu})} , \quad (63)$$

with the dependence on everything but  $\underline{\mu}$  and  $\underline{\nu}$  left implicit again. For  $k_0 r_{0\ell} \gg 1$ , the stationary-phase estimate is

$$I(\underline{\nu}) \approx \left( \frac{k_0}{4\pi r_{0\ell}} \right) \sum_{\underline{\sigma}} |\det \underline{\underline{M}}(\underline{\sigma}, \underline{\nu})|^{-1/2} e^{ik_0 r_{0\ell} \psi(\underline{\sigma}, \underline{\nu})} . \quad (64)$$

As in the baseband case,  $\underline{\sigma}$  is a stationary point,  $\psi$  the (scaled) phase, and  $\underline{\underline{M}}$  the phase curvature.

For the sideband case, this phase and its stationarity condition are

$$\psi(\underline{\mu}, \underline{\nu}) = \underline{n}(\theta_\ell) \cdot \underline{\mu} + \delta_\ell \gamma(|\underline{\mu} - \underline{\nu}|) + \epsilon_\ell \gamma(|\underline{\mu} + \underline{\nu}|) \quad (65)$$

$$\underline{n}(\theta_\ell) = \delta_\ell \frac{\underline{\mu} - \underline{\nu}}{\gamma(|\underline{\mu} - \underline{\nu}|)} + \epsilon_\ell \frac{\underline{\mu} + \underline{\nu}}{\gamma(|\underline{\mu} + \underline{\nu}|)} . \quad (66)$$

Estimates are needed for both sidebands in Eq. (38). With  $\nu > 0$ , this means evaluating Eq. (63) at  $\underline{\nu} = +\nu \underline{n}(\theta)$  and at  $\underline{\nu} = -\nu \underline{n}(\theta)$ . In this report, we deal explicitly with the *upper* sideband (the plus sign), and obtain the lower-sideband result by inspection. For any given  $\underline{\nu}$ , we first need to find the stationary point by solving Eq. (66) for  $\underline{\mu}$  within the region where  $\psi$  is real-valued. To do that, we adopt a pair of cartesian axis vectors

$$(\underline{e}_1, \underline{e}_2) = \left( \underline{n}(\theta - \frac{1}{2}\pi), \underline{n}(\theta) \right) , \quad (67)$$

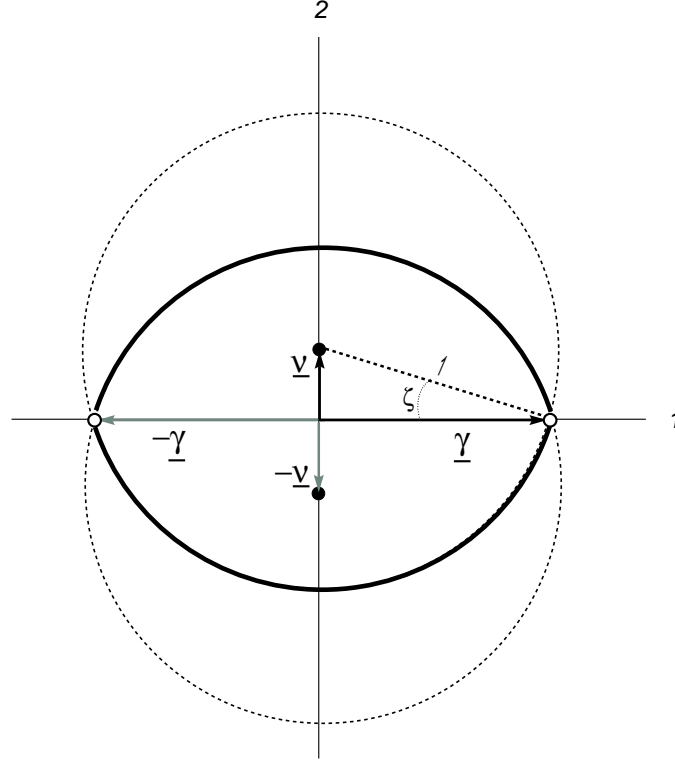


Fig. 2 —  $\underline{\mu}$ -plane shown for the *upper sideband* case. The two disks are the regions  $|\underline{\mu} - \underline{\nu}| < 1$  and  $|\underline{\mu} + \underline{\nu}| < 1$ . Any stationary phase points must lie in their overlap, where  $\psi(\underline{\mu}, \underline{\nu})$  is real.

where the first one points along the crests of the surface waves and the second along their propagation direction (see Fig. 1). The problem can now be understood in terms of the vectors  $\underline{\nu} = \nu \underline{e}_2$ ,  $\underline{\gamma} = \gamma \underline{e}_1$  and the two disks shown in Fig. 2. These disks have unit radii, their centers lie at the  $\bullet$  points where  $\underline{\mu} = \pm \underline{\nu}$ , and their edges intersect at the “vertices”  $\circ$ , where  $\underline{\mu} = \pm \underline{\gamma}$ . Any stationary points must lie within their *overlap*, the  $|\underline{\mu} \pm \underline{\nu}| \leq 1$  region bounded by  $\text{—}$ , so that both  $\gamma(|\underline{\mu} + \underline{\nu}|)$  and  $\gamma(|\underline{\mu} - \underline{\nu}|)$  will remain real. The need for such an overlap restricts  $\nu$  to values below unity. Since  $\delta_\ell$  and  $\epsilon_\ell$  are both much smaller than unity, Eq. (66) can only be satisfied when one of the denominators on its right-hand side is similarly small. This means that the stationary points must lie *near the boundary* of the overlap region. In scaled variables, Eq. (58) for scattering point  $p$  becomes

$$\frac{r_{0p}}{z_0} = \frac{\underline{\mu} - \underline{\nu}}{\gamma(|\underline{\mu} - \underline{\nu}|)} \quad \text{and} \quad \frac{r_{p\ell}}{z_\ell} = \frac{\underline{\mu} + \underline{\nu}}{\gamma(|\underline{\mu} + \underline{\nu}|)} . \quad (68)$$

If  $\gamma(|\underline{\mu} - \underline{\nu}|)$  is small compared to unity,  $\underline{\mu}$  must be close to the *lower* edge, and  $r_{0p}$  is, therefore, large. On the other hand, if  $\gamma(|\underline{\mu} + \underline{\nu}|)$  is small,  $\underline{\mu}$  lies near the *upper* edge and  $r_{p\ell}$  is large.<sup>6</sup>

The simplest analytical approach to finding the stationary points is to adopt bipolar coordinates  $(\xi, \eta)$  since they conform to the shape of the overlap (see Appendix A). (In adapting bipolar coordinates to the present problem, the function  $\gamma(x) = \sqrt{1 - x^2}$  has to be evaluated so often at  $x = \nu$  that  $\gamma(\nu)$  is abbreviated as  $\gamma$  wherever it occurs.) The top and bottom edges of the overlap

<sup>6</sup>There are solutions for which *both*  $\gamma(|\underline{\mu} - \underline{\nu}|)$  and  $\gamma(|\underline{\mu} + \underline{\nu}|)$  are small, and  $\underline{\mu}$ , therefore, lies near one of the vertices. These are neglected here because geometric spreading with *both*  $r_{0p}$  and  $r_{p\ell}$  large makes a far smaller contribution to the reverberation (smaller by at least 30 dB for all the simulations to appear in this report).

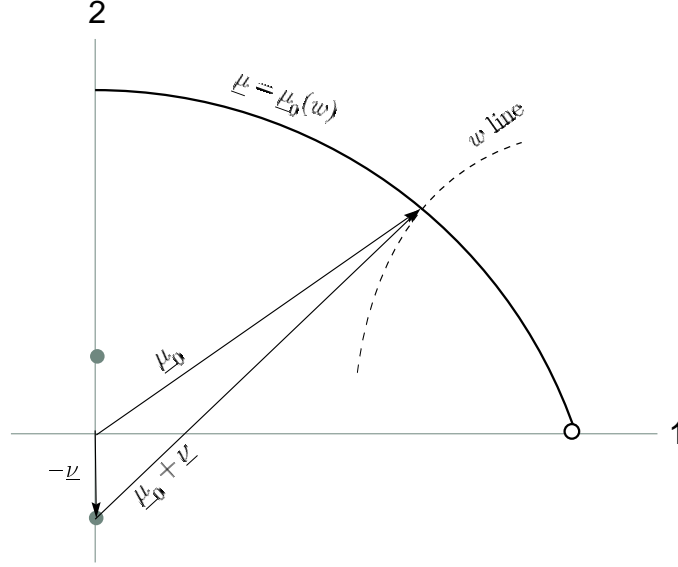


Fig. 3 — Upper edge of the overlap region—right half

are the coordinate lines  $\eta = \eta_0$  and  $\eta = 2\pi - \eta_0$ , where

$$\eta_0 = \arccos(-\nu) = \frac{\pi}{2} + \zeta \quad (69)$$

$$\zeta = \arctan(\nu/\gamma) . \quad (70)$$

$\zeta$  is the acute angle in Fig. 2. The angle  $\eta_0$  lies in the second quadrant  $(\frac{1}{2}\pi, \pi)$ , while  $2\pi - \eta_0$  is in the third quadrant  $(\pi, \frac{3}{2}\pi)$ . The interior of the overlap corresponds to  $-\infty < \xi < +\infty$ ,  $\eta_0 < \eta < 2\pi - \eta_0$ . The edges are reached by the limits  $\eta \downarrow \eta_0$  and  $\eta \uparrow 2\pi - \eta_0$  along constant- $\xi$  lines. We use  $w = e^{-|\xi|}$  and write  $\underline{R}(\theta)$  to indicate a counterclockwise plane rotation through  $\theta$ .

#### 4.6.1 Stationary Points

First, we examine the case with large  $r_{p\ell}/z_\ell$  and look for stationary points near the upper edge of the overlap. This edge is the coordinate line  $\eta = \eta_0$  on which  $\underline{\mu}$  is a function of  $w$  only:  $\underline{\mu} = \underline{\mu}_0(w)$ . At each point on it, the lower disk's unit radius vector  $\underline{\mu}_0(w) + \underline{\nu}$  is tangent to the  $w$  coordinate line through that point (because  $\xi, \eta$  are orthogonal coordinates).

We begin by focusing on the *right* ( $\xi > 0$ ) half-plane (see Fig. 3). Starting at the upper edge, we apply a small positive shift  $\delta\eta$  to move downward along the  $w$  line to a point  $\underline{\mu} = \underline{\mu}_0 + \delta\underline{\mu}$  inside the overlap. To first order, the inward shift  $\delta\underline{\mu}$  is antiparallel to  $\underline{\mu}_0 + \underline{\nu}$ . Throughout the right half-plane, Eq. (A5b) provides an exact result,  $\underline{\mu}(w, \eta) = [\underline{1} + w\underline{R}(\eta)][\underline{1} - w\underline{R}(\eta)]^{-1}\underline{\gamma}$ , from which the first-order inward shift is

$$\delta\underline{\mu} \approx \left. \frac{\partial \underline{\mu}}{\partial \eta} \right|_{\eta_0} \times \delta\eta = \frac{2w\partial \underline{R}(\eta)/\partial \eta}{(\underline{1} - w\underline{R}(\eta))^2} \bigg|_{\eta_0} \underline{\gamma} \delta\eta . \quad (71)$$

The derivative of the rotation is simply  $\partial \underline{R}(\eta)/\partial \eta = \underline{R}(\pi/2 + \eta)$ , and the inverse of  $\underline{1} - w\underline{R}(\eta)$  is given by Eq. (A6). Since  $(\cos \eta_0, \sin \eta_0) = (-\nu, \gamma)$ , one has

$$\underline{\mu}_0 = (a\underline{e}_1 + 2\gamma^2 w\underline{e}_2)/d , \quad \underline{\mu}_0 + \underline{\nu} = (a\underline{e}_1 + c\underline{e}_2)/d , \quad \underline{\mu}_0 - \underline{\nu} = (a\underline{e}_1 + b\underline{e}_2)/d \quad (72)$$

$$\delta\underline{\mu} = -\frac{2\gamma w \delta\eta}{d^2} (a\underline{e}_1 + c\underline{e}_2) \quad (73)$$

in terms of the temporary variables

$$\begin{aligned} a &= \gamma(1 - w^2) \geq 0 & c &= \nu + 2w + \nu w^2 \geq 0 \\ b &= -\nu + 2(1 - 2\nu^2)w - \nu w^2 & d &= 1 + 2\nu w + w^2 \geq 0. \end{aligned} \quad (74)$$

Variables  $a$  through  $d$  have absolute values less than 4 throughout  $0 \leq \nu, w \leq 1$ , and they are interrelated through  $a^2 + c^2 = d^2$  and  $c - b = 2\nu d$ . Since  $|\underline{\mu}_0 + \underline{\nu}| = 1$  and  $|\delta \underline{\mu}| \ll 1$ , Eq. (68) becomes

$$\frac{r_{p\ell}}{z_\ell} = \frac{\underline{\mu}_0 + \underline{\nu}}{\sqrt{-2(\underline{\mu}_0 + \underline{\nu}) \cdot \delta \underline{\mu}}} (1 + O(|\delta \underline{\mu}|)) \quad \text{and} \quad \frac{r_{0p}}{z_0} = \frac{\underline{\mu}_0 - \underline{\nu}}{2\sqrt{\underline{\mu}_0 \cdot \underline{\nu}}} (1 + O(|\delta \underline{\mu}|)) , \quad (75)$$

which, with Eqs. (72) and (73), is equivalent to

$$\frac{r_{p\ell}}{z_\ell} \approx \frac{1}{2\sqrt{\gamma w d} \delta \eta} (a \underline{e}_1 + c \underline{e}_2) \quad \text{and} \quad \frac{r_{0p}}{z_0} \approx \frac{1}{2\sqrt{2\gamma^2 \nu w d}} (a \underline{e}_1 + b \underline{e}_2) . \quad (76)$$

The stationarity relation Eq. (66) then reduces to

$$\underline{n}(\theta_\ell) = \frac{1}{2\sqrt{\gamma w d}} \left[ \frac{\delta_\ell}{\sqrt{2\gamma \nu}} (a \underline{e}_1 + b \underline{e}_2) + \frac{\epsilon_\ell}{\sqrt{\delta \eta}} (a \underline{e}_1 + c \underline{e}_2) \right] . \quad (77)$$

In cases of practical importance, the solutions for  $w$  that emerge from this equation are not arbitrarily small. This can be seen in the following way. Begin with the definition  $\nu = K/2k_0$ , invoke the gravity-wave dispersion relation  $K = \omega^2/g$  and take  $\omega$  to be the Pierson-Moskowitz dominant frequency  $\omega_d$ , Eq. (103). Then  $\nu$  has the value  $\nu_d = \omega_d^2/2gk_0 = \sqrt{\beta/20} \times gc_0/(\pi f_0 U^2)$ . For  $5\text{m/s} < U < 20\text{m/s}$ ,  $50\text{Hz} < f_0 < 200\text{Hz}$ , and  $\nu = \nu_d$ , the factor  $1/\sqrt{2\gamma \nu}$  in Eq. (77) is roughly  $4 (\pm 3)$ . This precludes  $w \sim \nu_\ell^2$  because values that small would leave the  $\delta_\ell$  term of order unity and the  $\epsilon_\ell$  term much greater than unity, making it impossible for  $\underline{n}(\theta_\ell)$  to have unit length. There may be solutions with  $w \sim \nu_\ell$ , but there are certainly none with  $w \sim \nu_\ell^2$ .

If we neglect the terms in Eq. (77) containing  $\delta_\ell/\sqrt{2\gamma \nu}$  relative to the much larger terms containing  $\epsilon_\ell/\sqrt{\delta \eta}$ , and form the components in the  $\underline{e}_2$  and  $\underline{e}_1$  directions, the outcome is

$$\sqrt{4\gamma w d} \cos \vartheta_\ell \approx \frac{\epsilon_\ell}{\sqrt{\delta \eta}} c \quad \text{and} \quad \sqrt{4\gamma w d} \sin \vartheta_\ell \approx \frac{\epsilon_\ell}{\sqrt{\delta \eta}} a . \quad (78)$$

Since  $a$  and  $c$  are non-negative, a solution for  $w$  and  $\delta \eta$  exists only when the angle  $\vartheta_\ell$  lies in the first quadrant  $(0, \frac{1}{2}\pi)$ . With  $\delta \eta$  eliminated, Eq. (78) reduces to  $a \cos \vartheta_\ell - c \sin \vartheta_\ell = 0$ , a quadratic equation in  $w$  whose physical solution is readily found to be

$$w = \frac{\gamma - \sin \vartheta_\ell}{\gamma \cos \vartheta_\ell + \nu \sin \vartheta_\ell} , \quad (79)$$

provided the angle is confined to  $0 \leq \vartheta_\ell \leq \frac{1}{2}\pi - \zeta$ . The angular restriction ensures that  $\cos \vartheta_\ell > \nu$  and, ultimately, that  $w$  lies in the physical range  $0 \leq w \leq 1$ . That entire range appears accessible only because the unattainably small values  $w \sim \epsilon_\ell^2$  have not yet been excluded.

Squaring and adding the two components of Eq. (78) produces  $\delta \eta = (\epsilon_\ell^2/4\gamma) \times (d/w)$  which, with  $w$  from Eq. (79), becomes

$$\delta \eta = \frac{\gamma \epsilon_\ell^2/2}{\cos \vartheta_\ell - \nu} . \quad (80)$$

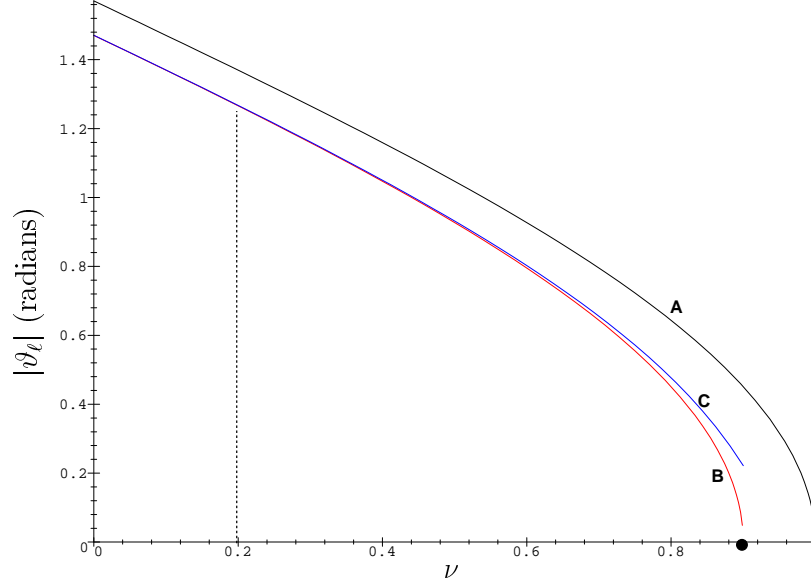


Fig. 4 — Admitted-angle sector for the upper edge, for  $\nu_\ell = 0.1$ . Curve (A) is  $\vartheta_\ell = \arccos \nu$ . The area above is the nonphysical  $w < 0$  region. Curves (B,C) are the exact and approximate forms of  $\vartheta_\ell = H_\ell(\nu)$  from Eqs. (81) and (85). The maximum wavenumber  $\nu = 1 - \nu_\ell$  is indicated by the  $\bullet$ . The dashed line shows the range of admitted  $\vartheta_\ell$  values at  $\nu = 0.2$  (i.e.,  $0 < \vartheta_\ell < 1.25 \approx 70^\circ$ ).

Because the azimuth has been restricted so that  $\cos \vartheta_\ell - \nu > 0$  (i.e.,  $\vartheta_\ell < \arccos(\nu) = \frac{1}{2}\pi - \zeta$ ), we know that  $\delta\eta$  is positive. Further restriction is needed to guarantee that it is small. Suppose we want to ensure that  $\delta\eta < (\epsilon_\ell^2/\nu_\ell) \times \gamma/2$ ; we will need to require  $\cos \vartheta_\ell - \nu > \nu_\ell$ , which means reducing the maximum allowable  $\vartheta_\ell$  from  $\frac{1}{2}\pi - \zeta$  to

$$H_\ell(\nu) = \arccos(\nu + \nu_\ell) . \quad (81)$$

This raises the minimum value of  $w$  obtainable via Eq. (79) from zero to  $\nu_\ell/2\gamma^2$ —the  $w \sim \nu_\ell$  minimum that was anticipated—and lowers the maximum  $\nu$  from 1 to  $1 - \nu_\ell$ . For a given geometry, stationary-phase points of the present type occur only for surface waves in the sector  $\theta_\ell \leq \theta \leq \theta_\ell + H_\ell(\nu)$ . Their bipolar coordinates are given by Eqs. (79) and (80).

The rest of the upper-edge stationary points—those in the *left* half-plane—are found in the same way, and the lower-edge points follow suit with only minor differences. We omit the details and just present the results.

In summary, we find the following for the sideband stationary points. All of them have

$$w = \frac{\gamma - |\sin \vartheta_\ell|}{\gamma |\cos \vartheta_\ell| + \nu |\sin \vartheta_\ell|} . \quad (82)$$

The *upper*-edge stationary points have  $\eta = \eta_0 + \delta\eta$  with

$$\delta\eta = \frac{\gamma \epsilon_\ell^2/2}{|\cos \vartheta_\ell| - \nu} \quad (83)$$

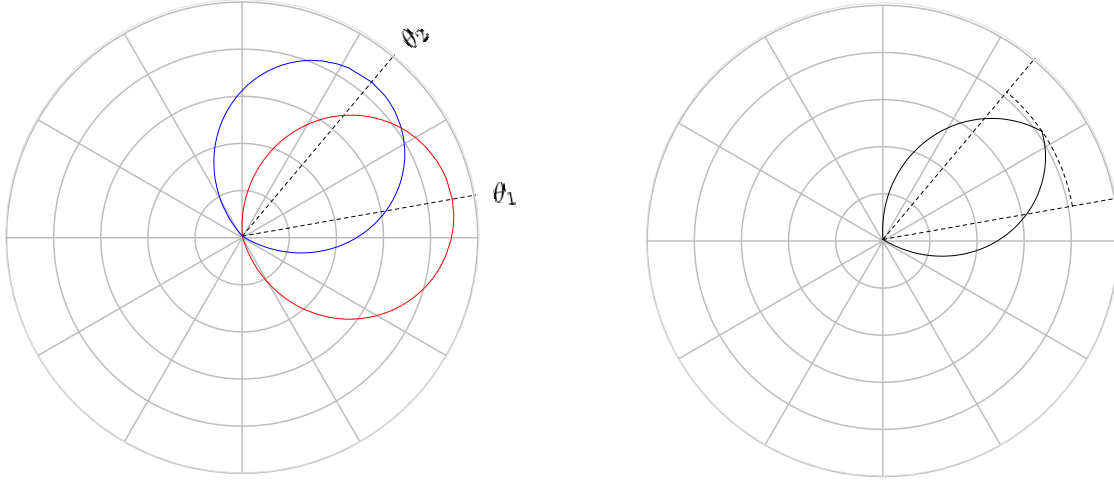


Fig. 5 —  $\nu$ - $\theta$  polar plots of the forward admitted sectors, for  $\nu \leq 1$ , with  $\theta_1 = 10^\circ$ ,  $\theta_2 = 50^\circ$ ,  $\nu_1 = 0.10$ , and  $\nu_2 = 0.15$ . Left:  $F_1(\nu)$  and  $F_2(\nu)$ .  $F_\ell(\nu)$  is centered on  $\theta_\ell$  and vanishes for  $\nu \geq 1 - \nu_\ell$ . Right: The intersection  $F(\nu) = F_1(\nu) \cap F_2(\nu)$ , which vanishes at  $\nu = \nu_{max}$  (dashed arc).

and correspond to near-*source* scattering from surface waves with  $\theta$  in the azimuth sector

$$F_\ell(\nu) \stackrel{def}{=} [\theta_\ell - H_\ell(\nu), \theta_\ell + H_\ell(\nu)] \quad (84)$$

(left side of Fig. 5), which is centered on the *forward* direction  $\theta = \theta_\ell$  and has a half-width of

$$H_\ell(\nu) \approx \frac{1}{2}\pi - (\zeta + \nu_\ell/\gamma) . \quad (85)$$

(Equation (85) is an order- $\nu_\ell$  approximation to Eq. (81). See Fig. 4.) The coordinate bounds are  $\nu_\ell/2\gamma^2 < w$  and  $\delta\eta < (\epsilon_\ell^2/\nu_\ell) \times \gamma/2$ , and the wavenumber range is  $0 < \nu < 1 - \nu_\ell$ . The *lower-edge* points have  $\eta = 2\pi - (\eta_0 + \delta\eta)$  with

$$\delta\eta = \frac{\gamma\delta_\ell^2/2}{|\cos \vartheta_\ell| - \nu} \quad (86)$$

and correspond to scattering near the *receivers* and to the surface-wave azimuth sector

$$\theta \in A_\ell(\nu) \stackrel{def}{=} [\pi + \theta_\ell - H_\ell(\nu), \pi + \theta_\ell + H_\ell(\nu)] , \quad (87)$$

which has the same half-width  $H_\ell(\nu)$  but is centered on the *aft* direction  $\theta = \pi + \theta_\ell$ . In this case,  $\delta\eta < (\delta_\ell/\nu_\ell) \times \gamma/2$ , but the  $w$  bound and  $\nu$  range are unaltered.

#### 4.6.2 Phase Factors

The phase of the fundamental sideband integral is given by Eq. (65). To lowest order, the small  $\epsilon_\ell$  and  $\delta_\ell$  terms may be neglected, so that  $\psi(\underline{\mu}, \underline{\nu}) \approx 1 - \nu |\cos(\theta - \theta_\ell)|$  for surface waves in either of the admitted sectors. Since  $\cos(\theta - \theta_\ell)$  is positive/negative in the forward/aft sectors,

$$\psi(\underline{\mu}, \underline{\nu}) = \begin{cases} 1 - \nu \cos(\theta - \theta_\ell) & \dots \quad \theta \in F_\ell(\nu) \\ 1 + \nu \cos(\theta - \theta_\ell) & \dots \quad \theta \in A_\ell(\nu) . \end{cases} \quad (88)$$

#### 4.6.3 Amplitude Factors

Straightforward differentiation produces the general result

$$\underline{\underline{M}}(\underline{\sigma}, \underline{\nu}) = \frac{\delta_\ell}{\gamma(|\underline{\sigma} - \underline{\nu}|)} \left\{ 1 + \frac{(\underline{\sigma} - \underline{\nu})(\underline{\sigma} - \underline{\nu})}{\gamma^2(|\underline{\sigma} - \underline{\nu}|)} \right\} + \frac{\epsilon_\ell}{\gamma(|\underline{\sigma} + \underline{\nu}|)} \left\{ 1 + \frac{(\underline{\sigma} + \underline{\nu})(\underline{\sigma} + \underline{\nu})}{\gamma^2(|\underline{\sigma} + \underline{\nu}|)} \right\}. \quad (89)$$

For upper-edge stationary points, we retain the term containing  $1/\gamma(|\underline{\mu} + \underline{\nu}|) \gg 1$  and drop the one containing  $1/\gamma(|\underline{\mu} - \underline{\nu}|) \gg 1$ . For lower-edge points, we do the opposite. This leads to

$$\det \underline{\underline{M}} \approx \begin{cases} \epsilon_\ell^{-2} & \cdots & \text{upper edge} \\ \delta_\ell^{-2} & \cdots & \text{lower edge} \end{cases}. \quad (90)$$

#### 4.6.4 Synthesis

With the amplitude and phase factors obtained above, the stationary-phase value of the fundamental sideband integral  $I(\underline{\nu})$  in Eq. (64) is

$$I(+2k_0\nu\underline{n}(\theta), \underline{r}_{0\ell}; z_0, z_\ell) = \frac{k_0}{4\pi r_{0\ell}^2} e^{ik_0 r_{0\ell}} \times \begin{cases} z_\ell e^{-ik_0\nu\underline{r}_{0\ell} \cdot \underline{n}(\theta)} & \cdots & \theta \in F_\ell(\nu) \\ z_0 e^{+ik_0\nu\underline{r}_{0\ell} \cdot \underline{n}(\theta)} & \cdots & \theta \in A_\ell(\nu) \end{cases}. \quad (91)$$

#### 4.6.5 Bragg-Only Constraint

For  $\nu < 1 - \nu_\ell$ ,  $H_\ell(\nu)$  is positive. Thus the source signal can be Bragg-scattered into the  $\ell$ th receiver by surface waves with  $\theta$  in either  $F_\ell(\nu)$  or  $A_\ell(\nu)$ . Requiring  $\nu < 1 - \nu_1$  and  $\nu < 1 - \nu_2$  would allow both receivers to be ensonified in this way, but that is not enough. The surface wave components doing the scattering are delta-correlated in azimuth (p. 8), which means that to produce a nonvanishing result, the *same* component must scatter to *both* receivers. Since  $H_\ell(\nu)$  decreases with  $\nu$ , we will need to reduce the maximum  $\nu$  to ensure this. We consider the forward sector explicitly.

For upper-edge stationary points, we must admit only surface waves that have  $\theta$  in the common forward sector  $F(\nu) \stackrel{def}{=} F_1(\nu) \cap F_2(\nu)$ . Since  $H_\ell(\nu)$  vanishes at  $\nu = 1 - \nu_\ell$ , we must require  $\nu < 1 - \max(\nu_1, \nu_2)$  to prevent the individual sectors  $F_1(\nu)$ ,  $F_2(\nu)$  from disappearing. To ensure that they overlap, we need  $|\theta_{12}| < H_1(\nu) + H_2(\nu)$ . At  $\nu = 1 - \max(\nu_1, \nu_2)$ , we have<sup>7</sup>  $H_1(\nu) + H_2(\nu) \approx \sqrt{2|\nu_{12}|}$ , with the following consequences (see Fig. 6). For  $|\theta_{12}| < \sqrt{2|\nu_{12}|}$  (e.g., lower  $\bullet$ ), no separate condition is needed. For  $|\theta_{12}| > \sqrt{2|\nu_{12}|}$  (e.g., upper  $\bullet$ ),  $\nu$  must be smaller than the solution of  $|\theta_{12}| = \arccos(\nu + \nu_1) + \arccos(\nu + \nu_2)$ . That solution is<sup>8</sup>

$$\nu_0 = \sqrt{q + \bar{\nu}_{12}} - \bar{\nu}_{12}, \quad (92)$$

where  $q = (1 + 2\nu_1\nu_2 \cos|\theta_{12}| - \cos^2|\theta_{12}| - \nu_1^2 - \nu_2^2)/2(1 - \cos|\theta_{12}|) > 0$ . Thus, the maximum  $\nu$  is

$$\nu_{max} = \begin{cases} 1 - \max(\nu_1, \nu_2) & \cdots & |\theta_{12}| < \sqrt{2|\nu_{12}|} \\ \nu_0 & \cdots & |\theta_{12}| > \sqrt{2|\nu_{12}|} \end{cases}. \quad (93)$$

<sup>7</sup> $\bar{\nu}_{12}$  and  $\nu_{12}$  are the mean and difference of  $\nu_1$  and  $\nu_2$ .

<sup>8</sup>Though it fails for  $|\theta_{12}| \sim \pi$ , this solution is valid for  $|\theta_{12}| < \pi/2$ , the range shown in Fig. 6, which easily covers all cases of practical interest.



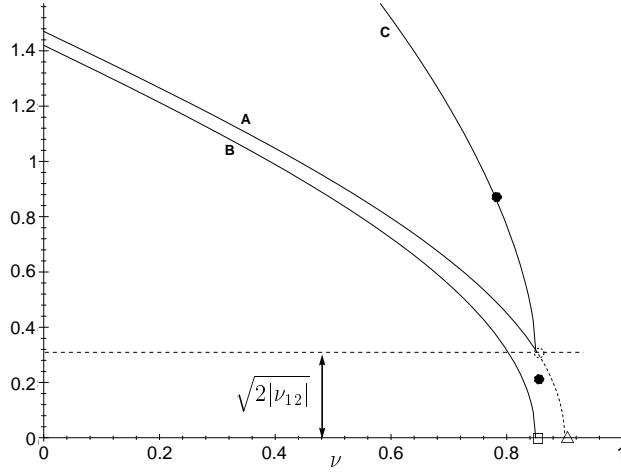


Fig. 6 — The Bragg-only constraint for the upper edge, with  $\nu_1 = 0.1$  and  $\nu_2 = 0.15$ . Curve (A) is the larger of  $H_1(\nu)$  and  $H_2(\nu)$ , curve(B) is the smaller, and curve (C) is their sum,  $H_1(\nu) + H_2(\nu)$ . The  $\square$  and  $\triangle$  indicate  $\nu = 1 - \max(\nu_1, \nu_2)$  and  $\nu = 1 - \min(\nu_1, \nu_2)$ , respectively. The ordinate of the point  $\circ$  is  $\sqrt{2|\nu_{12}|} \approx 0.316$ , corresponding to  $|\theta_{12}| \approx 18^\circ$ . The  $\bullet$  points are discussed in the text.

For  $0 < \nu < \nu_{max}$ , we have the nonvanishing forward-sector intersection,

$$F(\nu) = [-\tfrac{1}{2}\pi + \zeta + \max(\theta_1 + \nu_1/\gamma, \theta_2 + \nu_2/\gamma), \tfrac{1}{2}\pi - \zeta + \min(\theta_1 - \nu_1/\gamma, \theta_2 - \nu_2/\gamma)] \quad (94)$$

(see the right side of Fig. 5). For the lower-edge stationary points, the same sort of analysis applies and the surface wave azimuth  $\theta$  is restricted to the aft sector  $A(\nu) \stackrel{def}{=} A_1(\nu) \cap A_2(\nu)$  given by

$$A(\nu) = [\tfrac{1}{2}\pi + \zeta + \max(\theta_1 + \nu_1/\gamma, \theta_2 + \nu_2/\gamma), \tfrac{3}{2}\pi - \zeta + \min(\theta_1 - \nu_1/\gamma, \theta_2 - \nu_2/\gamma)] , \quad (95)$$

which is simply  $F(\nu)$  rotated by  $\pi$ .

#### 4.7 Sidebands, CSD Estimate

The final *upper*-sideband CSD result comes from Eq. (38). It is

$$\begin{aligned} C_{\text{ref}}^{(2,0)}(\underline{r}_{01}, \underline{r}_{02}, +|\omega|; z_0, z_1, z_2) &= \Phi(|\omega|) \int d\theta H(\theta) e^{ik_0 \nu \underline{r}_{12} \cdot \underline{n}(\theta)} \\ &\times I^*(+2k_0 \nu \underline{n}(\theta), \underline{r}_{01}; z_0, z_1) \times I(+2k_0 \nu \underline{n}(\theta), \underline{r}_{02}; z_0, z_2) , \end{aligned} \quad (96)$$

with the stationary-phase estimates for the fundamental integral  $I$  taken from Eq. (91). This is evaluated over the appropriate range of  $\nu$  for the geometry, with the integration including the admitted azimuths for each  $\nu$ . We have seen that this reduces to

$$C_{\text{ref}}^{(2,0)}(\underline{r}_{01}, \underline{r}_{02}, +|\omega|; z_0, z_1, z_2) = A e^{ik_0(r_{02}-r_{01})} \left\{ B \int_{F(\nu)} + D \int_{A(\nu)} e^{i2k_0 \nu \underline{r}_{12} \cdot \underline{n}(\theta)} \right\} H(\theta) d\theta , \quad (97)$$

$$A = \frac{\Phi(|\omega|)}{r_{01} r_{02}} \left( \frac{k_0}{4\pi} \right)^2 , \quad B = \frac{z_1 z_2}{r_{01} r_{02}} , \quad \text{and} \quad D = \frac{z_0^2}{r_{01} r_{02}} . \quad (98)$$

This applies within the range  $0 < \nu < \nu_{max}$ , where the source is able to ensonify both receivers by Bragg scattering from the same surface-wave component. The admitted sectors  $F(\nu)$ ,  $A(\nu)$  contain the azimuths  $\theta$  of all such components traveling in the forward and aft directions, respectively. With the relative receiver displacement expressed as  $\underline{r}_{12} = \varrho \underline{n}(\varphi)$ , the phase term in the above CSD integral is simply  $2k_0 \nu \underline{r}_{12} \cdot \underline{n}(\theta) = 2k_0 \nu \varrho \cos(\theta - \varphi)$ . A change of variables reduces Eq. (97) to

$$C_{\text{ref}}^{(2,0)}(\underline{r}_{01}, \underline{r}_{02}, +|\omega|; z_0, z_1, z_2) = A e^{ik_0(r_{02} - r_{01})} \times \int_{F(\nu)} d\theta \left\{ B H(\theta) + D e^{-i2k_0 \varrho \nu \cos(\theta - \varphi)} H(\theta + \pi) \right\}, \quad (99)$$

where  $k_0$  and  $K$  are wavenumbers for the acoustic signal and surface waves and  $\nu = K/2k_0$ . The sea surface is described by its dispersion relation  $|\omega| = \Omega(K)$ , power spectrum  $\Phi(|\omega|)$ , and directional spectrum  $H(\theta)$ . The *lower* sideband at  $-|\omega|$  is exactly the same except that  $H(\theta)$  and  $H(\theta + \pi)$  are interchanged.

#### 4.8 Sidebands, Colocated Receivers: the PSD

When the receivers are merged at a common location  $\vec{r}_*$ , the CSD reduces to the PSD,

$$C_{\text{ref}}^{(2,0)}(\underline{r}_{0*}, \pm|\omega|; z_0, z_*) = C_{\text{ref}}^{(2,0)}(\underline{r}_{02}, \underline{r}_{01}, \pm|\omega|; z_0, z_1, z_2) \Big|_{\underline{r}_{01}=\underline{r}_{02}=\underline{r}_{0*}; z_1=z_2=z_*},$$

with

$$A = \Phi(|\omega|)(k_0/4\pi r_{0*})^2, \quad B = (z_*/r_{0*})^2, \quad D = (z_0/r_{0*})^2.$$

The upper-sideband PSD is then

$$C_{\text{ref}}^{(2,0)}(\underline{r}_{0*}, +|\omega|; z_0, z_*) = A \int_{F(\nu)} d\theta \{ B H(\theta) + D H(\theta + \pi) \} \quad \cdots \quad 0 < \nu < \nu_{max}, \quad (100)$$

and the lower-sideband result  $C_{\text{ref}}^{(2,0)}(\underline{r}_{0*}, -|\omega|; z_0, z_*)$  is produced from it via  $H(\theta) \Rightarrow H(\theta + \pi)$ .

#### 4.9 Sidebands, Symmetries

In general, the upper and lower CSD sideband contributions are unequal. However, as Harper and Labianca originally noted for the PSD in the bistatic limit [3–5], identical sidebands *do* result in one special geometry—when the receivers lie in the crosswind direction from the source (i.e., in the  $x = 0$  plane<sup>9</sup>). It is not difficult to show that, for receivers anywhere in that vertical plane, the interchange  $H(\theta) \Rightarrow H(\theta + \pi)$  leaves the  $F$  and  $A$  integrals in Eq. (97) unaltered.<sup>10</sup> Thus, in that one particular configuration,<sup>11</sup> the sidebands are identical in both amplitude and phase.

A different kind of symmetry arises from the transformation

$$\theta_1, \theta_2 \longrightarrow \pi - \theta_1, \pi - \theta_2, \quad (101)$$

which reflects  $\underline{r}_1$  and  $\underline{r}_2$  across the  $x$  (i.e., crosswind) axis. With the CSD expressions obtained here, only trivial manipulation is needed to reveal that the effect of Eq. (101) is simply to swap the sidebands.<sup>10</sup>

<sup>9</sup>References 3 and 5 cite the  $x = 0$  plane; Ref. 4 cites the  $y = 0$  plane, but this is presumably just a typo.

<sup>10</sup>This also requires the fairly innocuous assumption of crosswind symmetry,  $H(\theta) = H(-\theta)$ .

<sup>11</sup>Of course, this also occurs trivially in *any* configuration with a completely isotropic sea surface  $\mu = 0$ .

The PSD sidebands are also unequal except in certain special source/receiver configurations. Obviously, one such configuration is the bistatic limit ( $\varrho \rightarrow 0$ ) of any configuration with equal CSD sidebands (e.g., any receiver located in the  $x = 0$  vertical plane). The PSD also has symmetric sidebands whenever the source and receiver are at the same depth (since  $z_0 = z_*$  implies  $B = D$ ), a fact recognized early on by Harper and Labianca [2–6].

## 5. SIDEBAND SIMULATIONS

This section presents several CSD sideband computations for an ocean of uniform sound speed,  $c_0 = 1500$  m/s. The sea surface is characterized by expressions for the power and directional spectra  $\Phi(\omega)$  and  $H(\theta)$  that have found theoretical or experimental support. The power spectrum is the archetypical one for fully developed wind-driven seas—the Pierson-Moskowitz distribution [26],

$$\Phi(\omega) = \frac{\alpha g^2}{\omega^5} \exp\left(-\frac{5}{4}(\omega_d/\omega)^4\right) \quad \cdots \quad \omega > 0 \quad (102)$$

(see Fig. 7), which modifies Phillips’s  $\omega^{-5}$  behavior [27] by introducing a dominant frequency

$$\omega_d = (\frac{4}{5}\beta)^{1/4} g/U \quad (103)$$

( $U$  is the wind speed at 19.5 m,  $g$  is the gravity constant,  $\alpha = 0.0081$  is the Phillips constant, and  $\beta = 0.74$  is a second empirical constant.) The associated mean-square waveheight is

$$h_{\text{rms}}^2 = \int_0^\infty d\omega \Phi(\omega) = \frac{\alpha g^2}{5\omega_d^4} = \frac{\alpha}{4\beta g^2} U^4 \quad (104)$$

The directional spectrum is an empirical “cosine-power” form inferred from at-sea data by Longuet-Higgins and coworkers [28,29] (see Fig. 8),

$$H(\theta) \propto |\cos(\theta/2)|^{2\mu} \quad (105)$$

The normalization is  $\oint d\theta H(\theta) = 1$ , and the directionality index  $\mu$  has a non-negative frequency-dependent value, typically about 4 but sometimes less than 1. Unlike such forms as  $H(\theta) \propto \cos^2(\theta)$  [12], this is *not* upwind/downwind symmetric (except in the isotropic  $\mu = 0$  case).

The simulations explore the influence of source/receiver geometry for various  $U$ ,  $f_0$ , and  $\mu$ . In each case, values are chosen for these three parameters and results are then generated simultaneously for an entire series of receiver geometries. (The computation is vectorized over geometry.) For each geometry, the upper and lower sidebands are evaluated at 80 frequency points each, and the numerical azimuth integration is done by the trapezoid method with  $2^\circ$  step size. Simulations are identified by figure number (e.g., the CSD from simulation 12 is in Fig. 12). These figures all use a common format. The upper half is a plot of the top<sup>12</sup> 30 dB of the *magnitude* of the CSD, with decibel values indicated in a color scale on the right. Overall levels are low because source-to-surface and surface-to-receiver propagation losses have not been removed, as is done in computing surface scattering strengths. However, all the computations are done at the same average source-receiver range (5 km), so the results can be directly compared with each other. The lower half of each figure shows the CSD *phase* in degrees, using a  $360^\circ$ -periodic color scale. The ordinate of each plot simply enumerates the geometries used. The abscissa is the Doppler frequency shift. Its axis extends in both directions to a maximum value  $f_{\text{max}} \stackrel{\text{def}}{=} \Omega(2k_0)/2\pi = \sqrt{gf_0/\pi c_0}$ , corresponding to

<sup>12</sup>Values more than 30 dB below the maximum are not rendered. They appear as patches of white space.

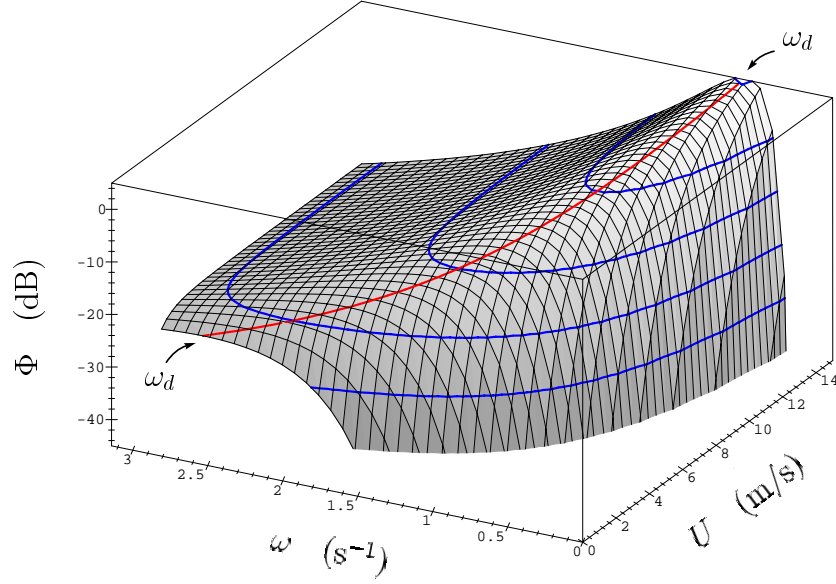


Fig. 7 — The Pierson-Moskowitz power spectral density  $\Phi(\omega)$ , Eq. (102), with the parametric dependence on wind speed  $U$  shown. Contours are at 10-dB intervals. The dominant frequency  $\omega_d$ , Eq. (103), is also shown running along the ridge. For this plot, the largest  $\omega$  corresponds to 0.5 Hz and the smallest  $U$  used is 3 m/s.

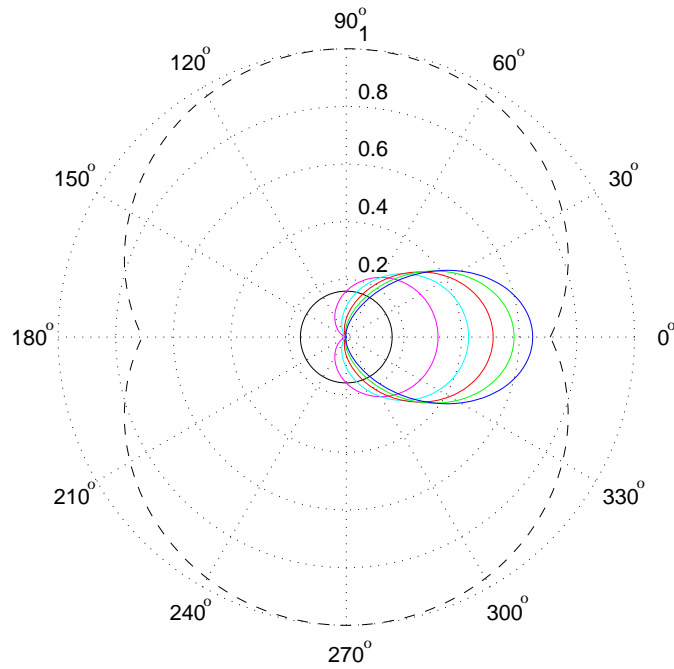


Fig. 8 — Solid: the Longuet-Higgins “cosine-power” directional spectrum  $H(\theta)$ , Eq. (105), for integer values of  $\mu$  from 0 (circular) to 5 (most elongated).  $\mu \approx 4$  is typical. The wind blows left-to-right, so  $0^\circ$  is the downwind direction. The dashed line shows a factor in Eq. (52).

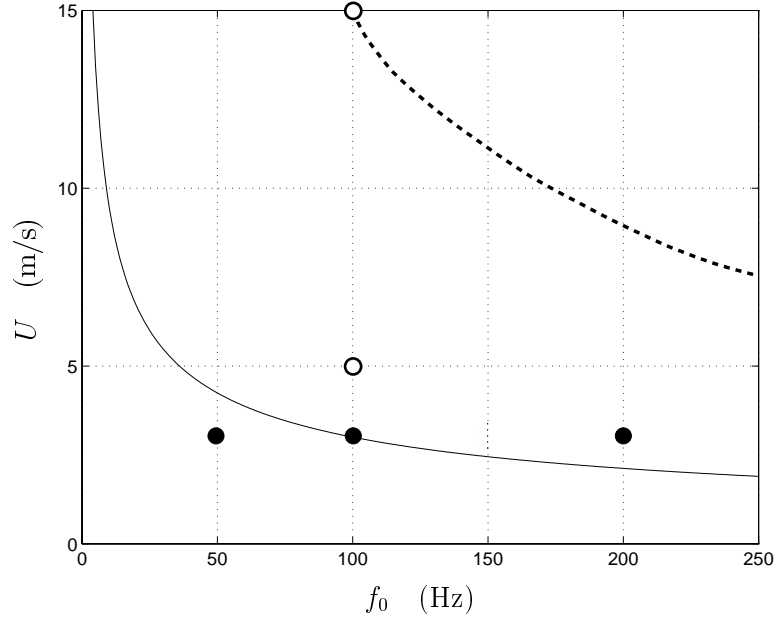


Fig. 9 — Wind speeds and frequencies used in simulations, as described in the text

the  $\nu = 1$  cutoff of Bragg scattering. Although there is no minimum Doppler shift in the theory, a *de facto*  $f_{min}$  occurs where the 30 dB window used in rendering these figures cuts off the exponential low-frequency rolloff of the surface power spectrum. These figures are all blank in the baseband  $|f| < f_{min}$ . It should be remembered that this is not because the zero-Doppler contributions are absent, but because only the sideband contributions are being plotted.

The wind speeds and frequencies used are represented by the five circles in Fig. 9. With one exception, these are chosen to lie between the solid and dashed lines in that figure. The dashed line is taken from Ogden and Erskine [1, Fig. 21] and represents their estimate for the onset of significant whitecap formation. We stay below it so that surface reverberation can reasonably be attributed to interface scattering. The solid line represents  $\nu_d = 1$ . Since  $\nu_d$  varies inversely with  $f_0$  and  $U$ , one has  $\nu_d < 1$  only *above* the line. Bragg scattering from a surface component requires  $\nu < 1$ , so the region below the solid line should yield much lower reverberation levels because the dominant surface waves cannot contribute there.

The impact of  $\mu$  is foreshadowed in Fig. 10. This figure presents a plan view of the surface points (\*) where dominant waves scatter the signal to a typical receiver. Those on the left side lie relatively close to the source and seem to form one branch of a hyperbola. The ones on the right are grouped around the receiver and appear to coincide with the other branch. The line segments indicate directions of travel for the pair of counterpropagating waves that participate in the scattering at each \*. Their lengths are  $H(\theta)$  and  $H(\theta + \pi)$ , where  $\theta$  and  $\theta + \pi$  are the headings of the two surface waves. Different colors indicate contributions to the upper and lower sidebands (USB, LSB).

## 5.1 Horizontal Geometries

In each of the first ten simulations, a horizontal reference point  $\underline{r}_c = (r_c, \theta_c)$  is chosen and the receivers are laid out at a common depth in the following way. The first placement (with geometry index 1) has  $\underline{r}_1$  and  $\underline{r}_2$  closely bracketing  $\underline{r}_c$ . As the geometry index increases,  $\underline{r}_1$  and  $\underline{r}_2$

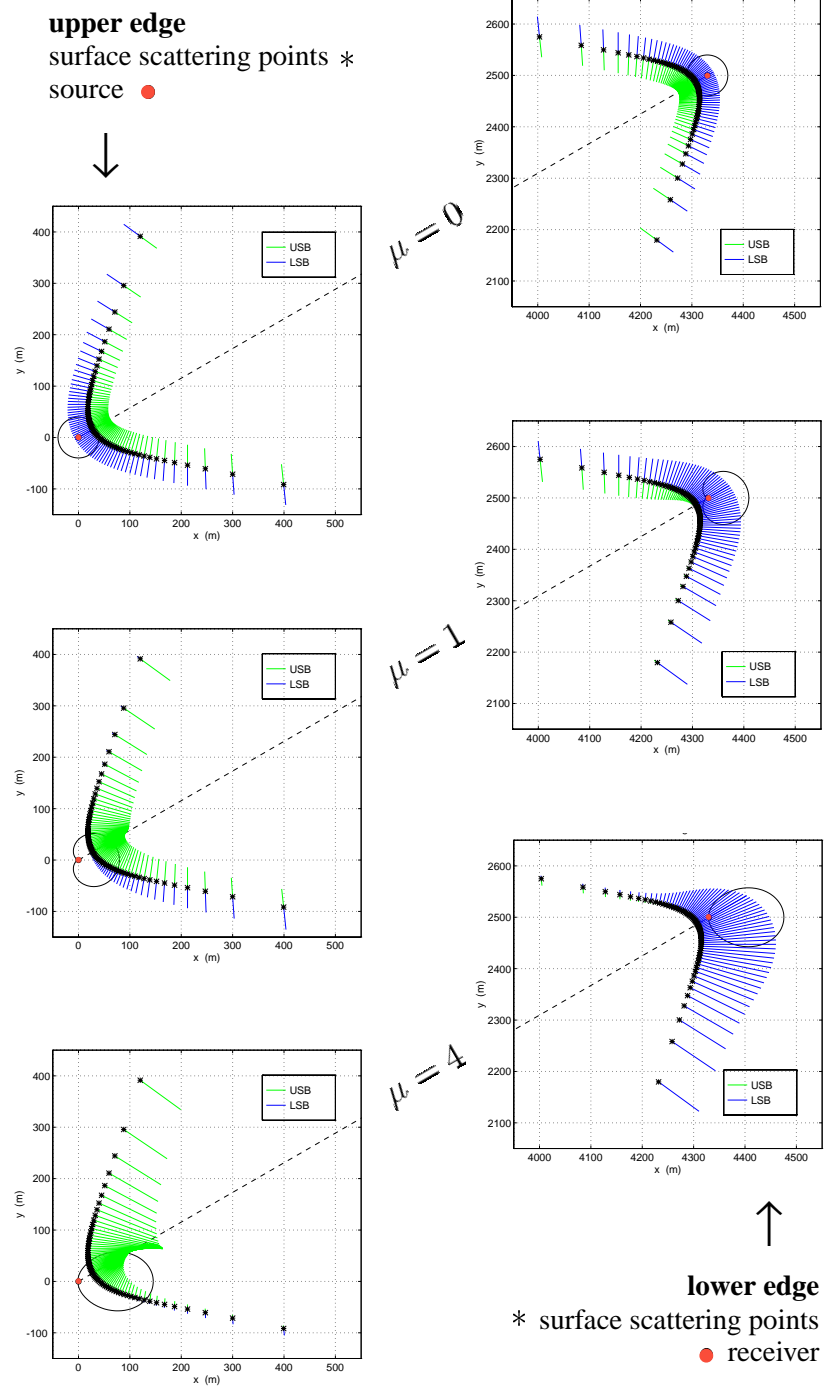


Fig. 10 — Plan view of the surface scattering points for the  $\nu = \nu_d$  components of a Pierson-Moskowitz surface spectrum. The azimuth is sampled in  $2^\circ$  steps.  $f_0 = 100$  Hz,  $U = 5$  m/s,  $\theta_\ell = 30^\circ$ ,  $z_0 = 110$  m,  $z_\ell = 90$  m, and  $r_{0\ell} = 5$  km.

separate uniformly along a straight line, keeping  $\underline{r}_c$  between them. The result is a series of receiver geometries with a common value of  $\varphi$  and with steadily increasing  $\varrho$ , as in Fig. 11. Parameter values are always chosen so that the geometry index is numerically equal to the receiver separation  $\varrho$  in meters. The depths are not varied. For all cases,  $r_c = 5$  km,  $\theta_c = 30^\circ$ ,  $\varrho = (1 \text{ m}, 2 \text{ m}, \dots, 200 \text{ m})$ ,  $z_1 = z_2 = 100$  m, and  $z_0 = 90$  m. Table 1 gives the values of the remaining variables.

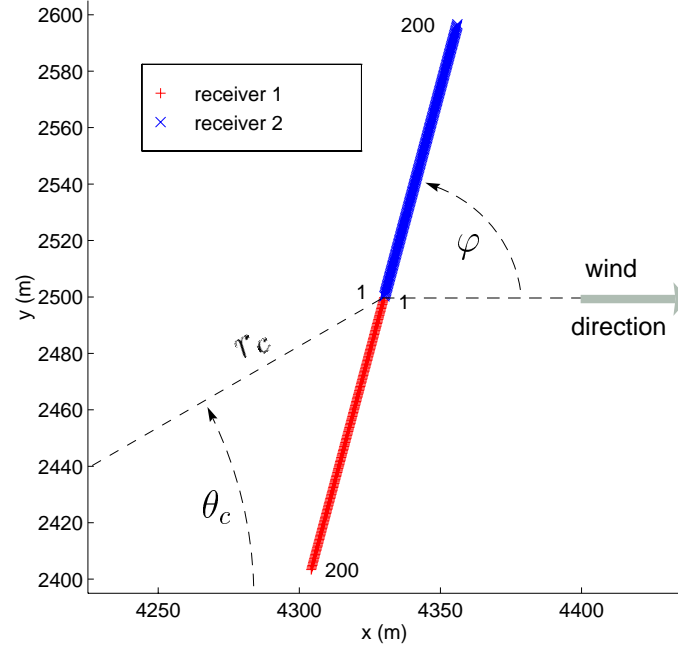


Fig. 11 — Geometries for a horizontal simulation. In this example, geometry index =  $1, \dots, 200$

Table 1 — Input Parameters for the Horizontal Simulations

Fig.	$f_0$ (Hz)	$U$ (m/s)	$\mu$	$\varphi$ ( $^\circ$ )
12	100	15	4	75
13	100	15	4	50
14	100	15	4	0
15	100	5	4	75
16	100	5	4	50
17	100	5	4	0
18	200	3	4	50
19	100	3	4	50
20	50	3	4	50
21	100	5	0	75

Simulations 12–14 correspond to the upper  $\circ$  in Fig. 9. The wind speed is the maximum from that figure and the frequency is the highest value consistent with pure interface scattering at that wind speed. The amplitudes for these simulations have certain main features in common:

1. sideband peaks at  $f_d = 0.09$  Hz, due to scattering by the dominant surface waves,
2. amplitudes that drop off by 30 dB before reaching  $f_{max} = 0.45$  Hz, and
3. a *de facto* minimum  $f_{min} = 0.05$  Hz, which is produced by the 30 dB cutoff.

There is, however, considerable detail that varies from one simulation to another.

In simulation 12, the amplitude is largest where  $\varrho$  is one meter (at geometry index 1). At that point, the two sidebands are symmetric about zero Doppler. With increasing separation, the USB remains virtually unchanged, but the entire LSB structure narrows considerably as  $\varrho$  approaches 200 m. This contraction is accompanied by the emergence of a set of secondary peaks—the ridges on the downshift side. These appear to grow at the expense of the main peak, which falls by 5 dB while the adjacent secondary peak rises to within 10 dB of it. The corresponding phase is shown in the bottom half of the figure. The USB has very little structure. Each  $\varrho$  produces the same phase for all Doppler shifts, and this value simply loops through about  $9^{1/4}$  regular  $360^\circ$  cycles as  $\varrho$  traverses its 200 m range. This is easily understood in terms of the horizontal source/receiver layout for this simulation, which is shown Fig. 11. The receivers lie at a horizontal angle  $|\theta_c - \varphi| = 45^\circ$ , with the radial to the source. Given the signal’s 15 m wavelength, direct line-of-sight propagation would yield  $\arccos(9.25 * 15/200) = 46.07^\circ$ , which agrees quite well considering that it neglects the deviation due to grazing the surface. The LSB phase is virtually the same if one looks only under the main peak. The secondary peaks, however, are an altogether different matter. At any given  $\varrho$ , the phase under these structures is not even approximately independent of Doppler shift.

For simulation 13,  $\varphi$  is reduced to  $50^\circ$ . The effect on the CSD amplitude is to lessen the large- $\varrho$  narrowing of the LSB and to fill in the troughs between its secondary peaks, leaving only a slightly wavy shoulder on the downshifted side. The phase shows a corresponding smoothing of the secondary-peak artifacts in its LSB. The USB now executes approximately  $12^{1/2}$  full phase cycles, corresponding to  $\arccos(12.5 * 15/200) = 20.36^\circ \approx |\theta_c - \varphi| = 20^\circ$ .

Simulation 14 uses  $\varphi = 0^\circ$  (i.e., one receiver directly downwind of the other). The phase executes about  $11^{1/2}$  full cycles, which yields the now familiar angular agreement:  $\arccos(11.5 * 15/200) = 30.40^\circ$  vs  $|\theta_c - \varphi| = 30^\circ$ . Beyond that, there is no more than a slight quantitative shift to distinguish this from the preceding simulation. The sidebands’ amplitudes are quite similar, but the LSB’s phase is still Doppler dependent.

These simulations were all rerun, with  $\theta_c, \phi \longrightarrow \pi - \theta_c, \pi - \phi$ . That transformation is equivalent to Eq. (101) and, thus, should simply swap the sidebands in each simulation. This is exactly what happened. The results are not included since they are merely Figs. 12–14 held up to a mirror.

Simulations 15–17 repeat the previous three simulations with  $U$  reduced to 5 m/s. This wind speed corresponds to the lower  $\circ$  in Fig. 9, and since that symbol lies above the solid line, dominant-wave scattering should still be a principal feature. Relative to simulations 12–14:

1. the levels are down by about 25 dB, of which 15–20 dB can be attributed to the reduction in  $\Phi(\omega_d)$  as the wind speed drops from 15 m/s to 5 m/s (see Fig. 7);
2.  $f_{max}$ , being independent of wind speed, is unchanged;
3.  $f_d \propto U^{-1}$ , so the main Doppler peaks are upshifted a factor of 3 to about 0.27 Hz; and
4.  $f_{min}$  rises by roughly the same factor to about 0.16 Hz.



The USB remains as featureless as ever, but there is more detailed structure in the LSBs and greater variation among the simulations.

In simulation 15, the LSB amplitude falls off faster with increasing  $\varrho$  than it did in simulation 12, where the wind speed was higher. Indeed, by the time  $\varrho$  has reached 20 m, the main peak is already down by roughly 5 dB. It is hard to be exact about this figure, however, because the secondary peaks cut across the main peak, blending with it to form a heavily corrugated structure. The LSB phase reflects this structure but otherwise differs little from simulation 12.

Simulations 16 and 17 continue the trend noted in simulations 13 and 14. As  $\varphi$  is reduced, there is a substantial fading of the irregularities in the LSB's amplitude. For  $\varrho$  less than a few meters, the LSB is always identical to the USB in both amplitude and phase. As  $\varrho$  increases further, the main LSB Doppler peak drops rapidly by about 10 dB and then begins to taper off more slowly, while the USB undergoes no material change. Ultimately, as  $\varphi$  reaches  $0^\circ$  in simulation 17, the LSB amplitude resembles a version of the USB with the top 5 dB of the Doppler peak removed. The phases, however, remain markedly different. At any given receiver separation (i.e., any geometry index), the USB frequency components are all in phase but the LSB components are not.

Simulations 18–20 correspond to the three  $\bullet$  symbols in Fig. 9. The frequencies  $f_d$ ,  $f_{max}$ , and the decibel level of the CSD amplitude are examined and compared to extrapolations from simulation 16 based on the relations  $f_d \propto U^{-1}$ ,  $f_{max} \propto \sqrt{f_0}$ ,  $A \propto f_0^2$  and the  $U$  dependence of  $\Phi(\omega_d)$  from Fig. 7. In all three simulations,  $f_{min}$  remains approximately 0.27 Hz, and the number of phase cycles in the USB remains accurately proportional to  $f_0$ .

Simulation 18, with  $\nu_d = 0.50$ , lies well within the  $\nu_d < 1$  region.

1. The level is  $-5.5$  dB relative to simulation 16. To a good approximation, this is the sum of the  $-11$  dB change in  $\Phi(\omega_d)$  as  $U$  decreases from 5 m/s to 3 m/s and the  $+6$  dB change in  $A$  due to the doubling of  $f_0$ .
2. The maximum Doppler is now  $0.45 \text{ Hz} * \sqrt{2} = 0.64 \text{ Hz}$ .
3. The main Doppler peak is shifted to  $0.27 \text{ Hz} * 5/3 = 0.45 \text{ Hz}$ .

The extrapolations from simulation 16 are all accurate.

Simulation 19 is the borderline case,  $\nu_d = 1.00$ .

1. The dB level change is  $-14$ , whereas the dominant-wave prediction is  $-11$ .
2.  $f_{max} = 0.45 \text{ Hz}$ , as in simulation 16.
3.  $f_d = 0.45 \text{ Hz}$ , but the main Doppler peak is actually at  $0.40 \text{ Hz}$ .

The  $\omega_d < \omega$  part of the surface spectrum is unable to Bragg scatter. This reduces the dB level and even skews the main Doppler peak to a lower value.

Simulation 20 has  $\nu_d = 2.00$ .

1. The dB level change is  $-33.5$ , but the dominant-wave prediction is  $-11 - 6 = -17$ .
2.  $f_{max} = 0.45 \text{ Hz} * \sqrt{0.5} = 0.32 \text{ Hz}$ .
3. There is no actual Doppler peak, since  $f_{max} < f_d = 0.45 \text{ Hz}$ .

This simulation is so far below the dominant-wave cutoff  $\nu_d = 1$  that all extrapolations based on the dominant wave picture of Bragg scattering are invalid.

Simulation 21 repeats simulation 15 with an isotropic sea surface. The sidebands are perforce symmetric. The amplitude still exhibits 5 dB corrugations, but the phase has only mild ripple features with none of the wild behavior previously seen in the LSB.

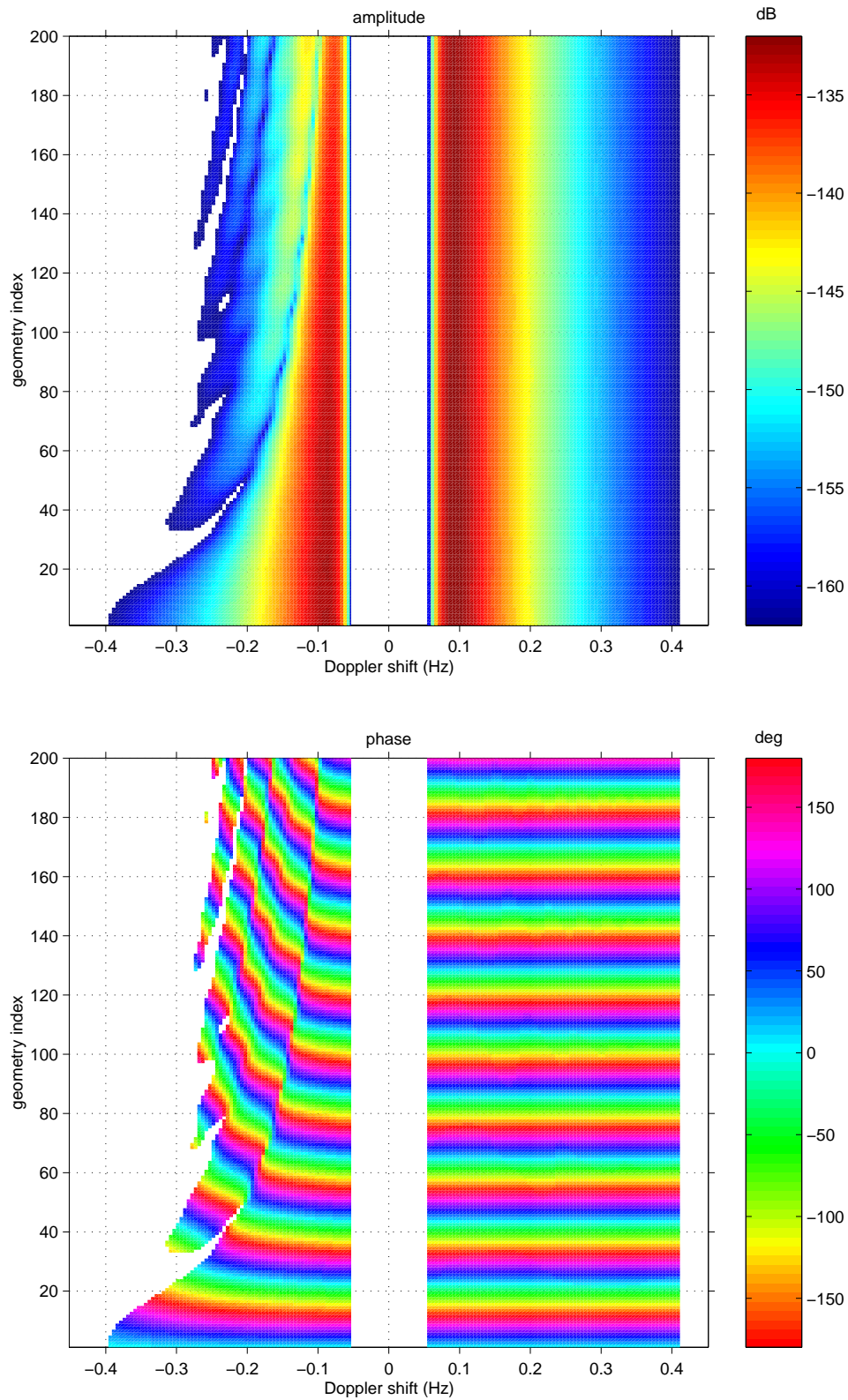


Fig. 12 — CSD simulation 12

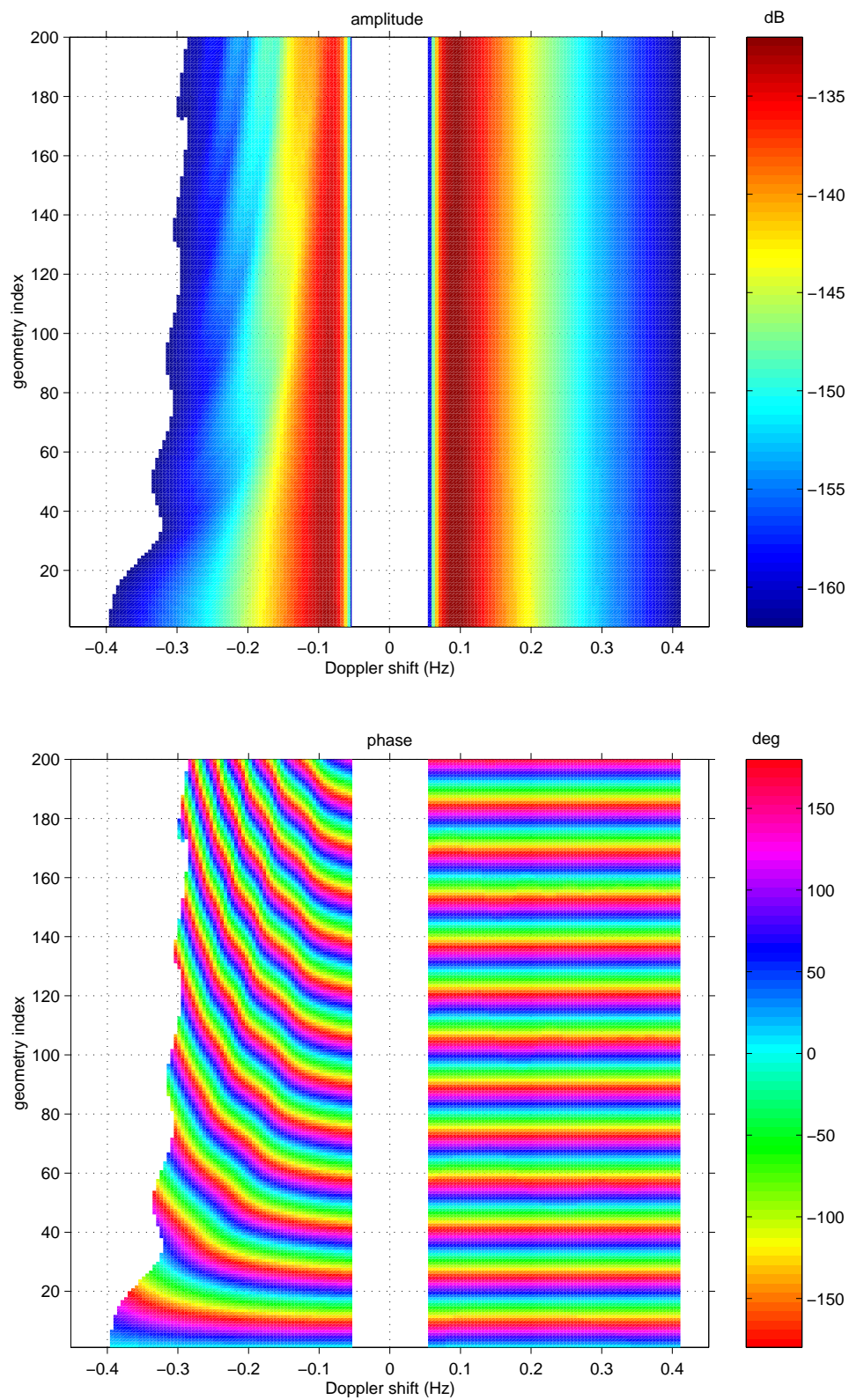


Fig. 13 — CSD simulation 13



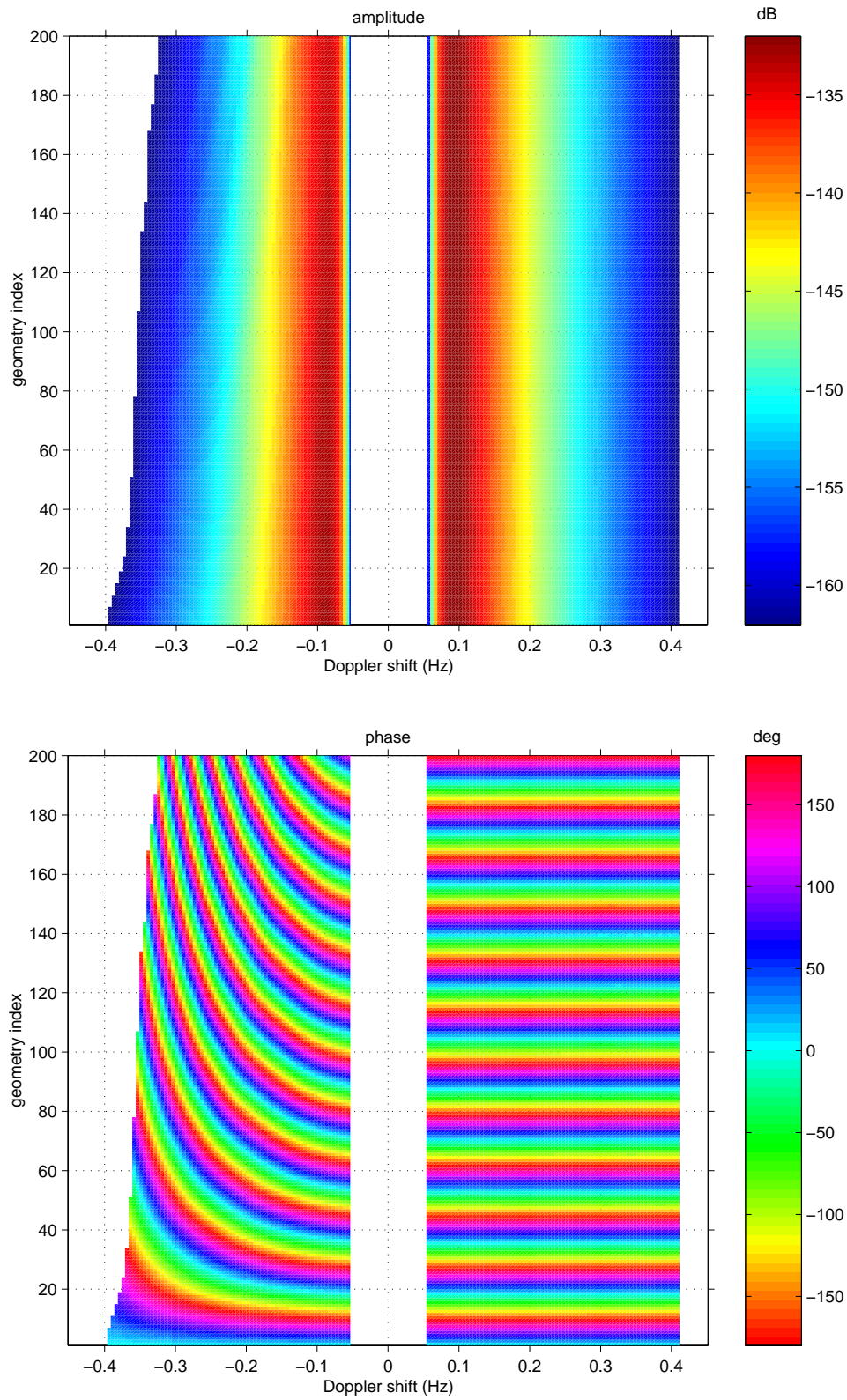


Fig. 14 — CSD simulation 14

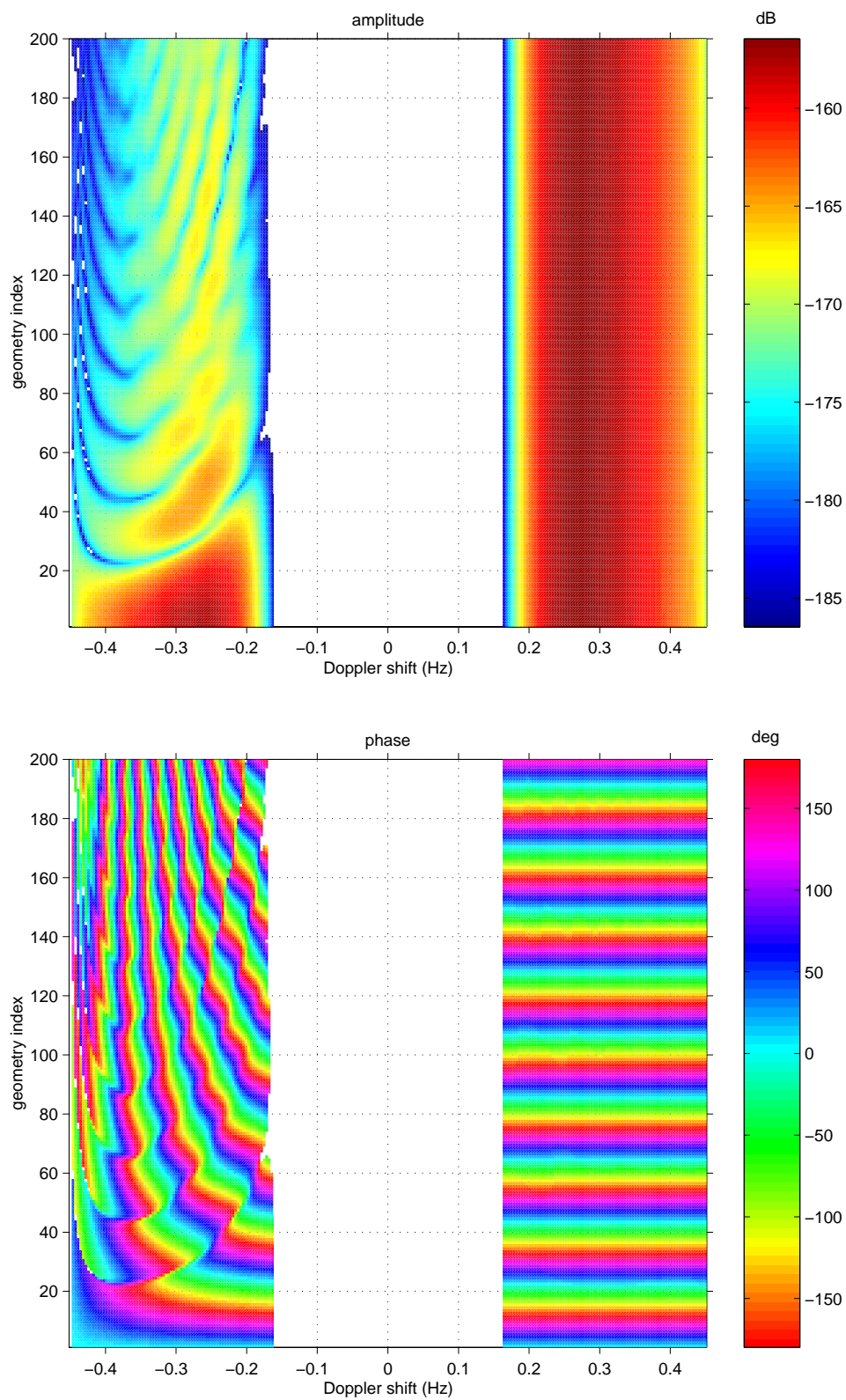


Fig. 15 — CSD simulation 15

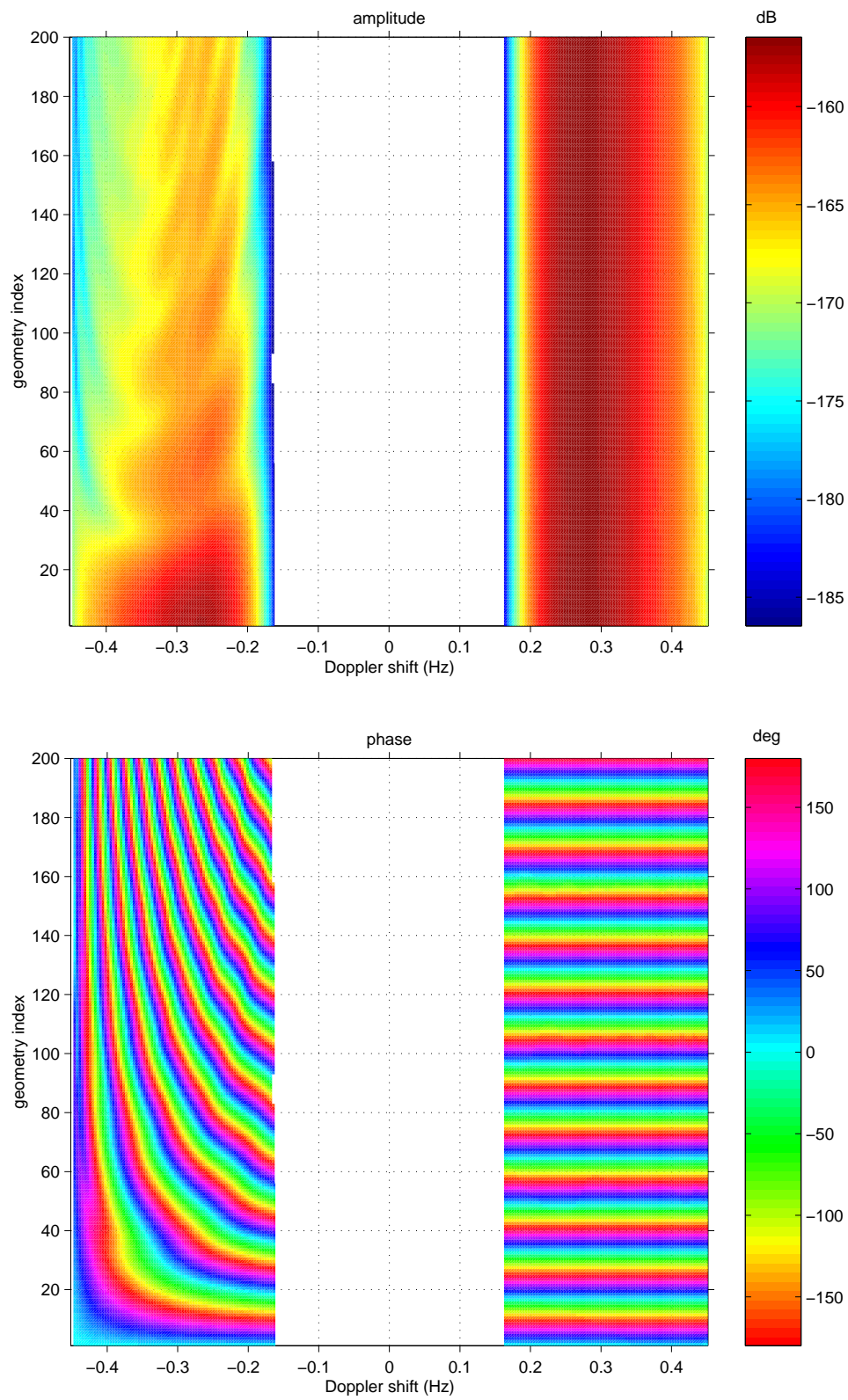


Fig. 16 — CSD simulation 16



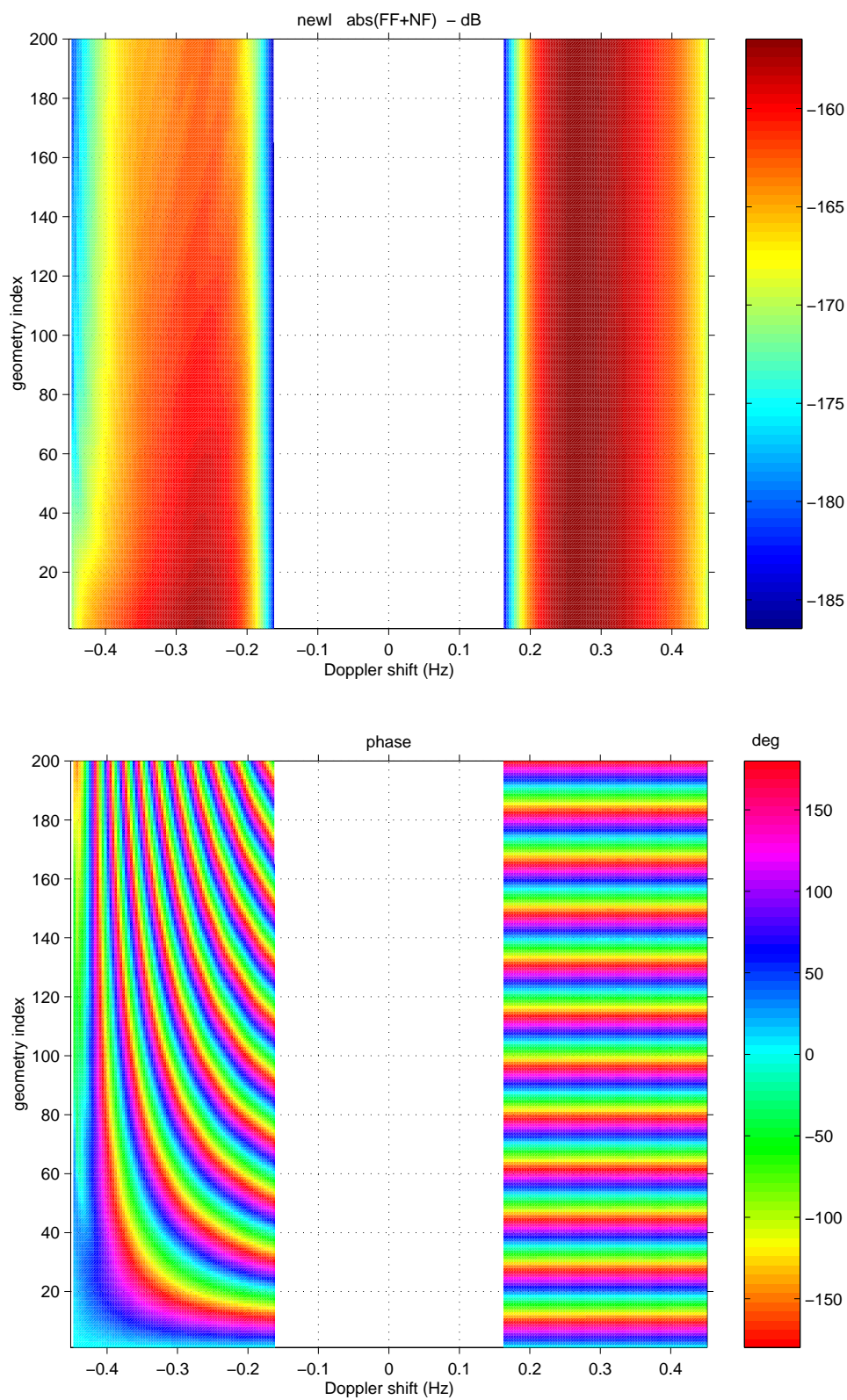


Fig. 17 — CSD simulation 17

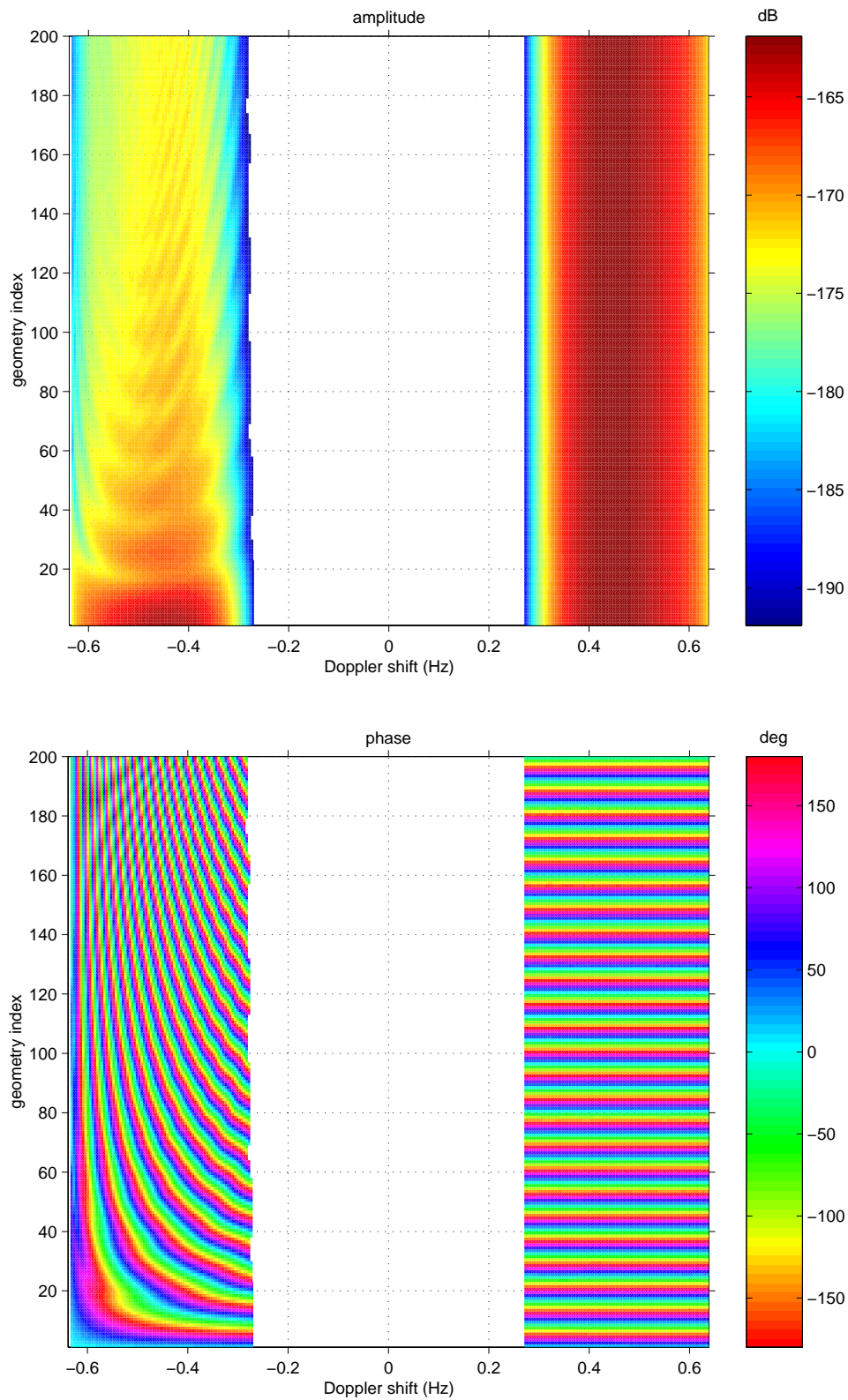


Fig. 18 — CSD simulation 18



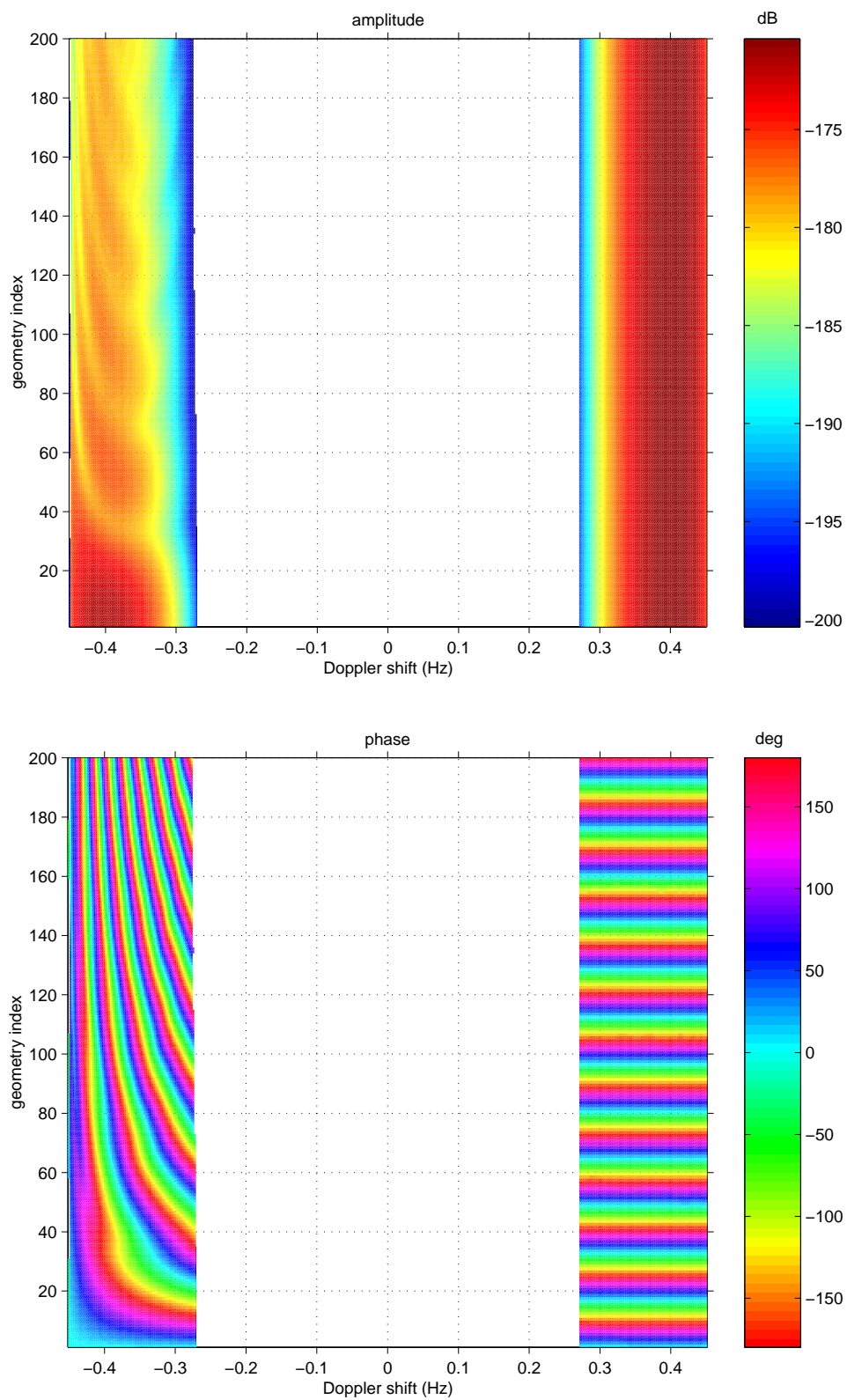


Fig. 19 — CSD simulation 19

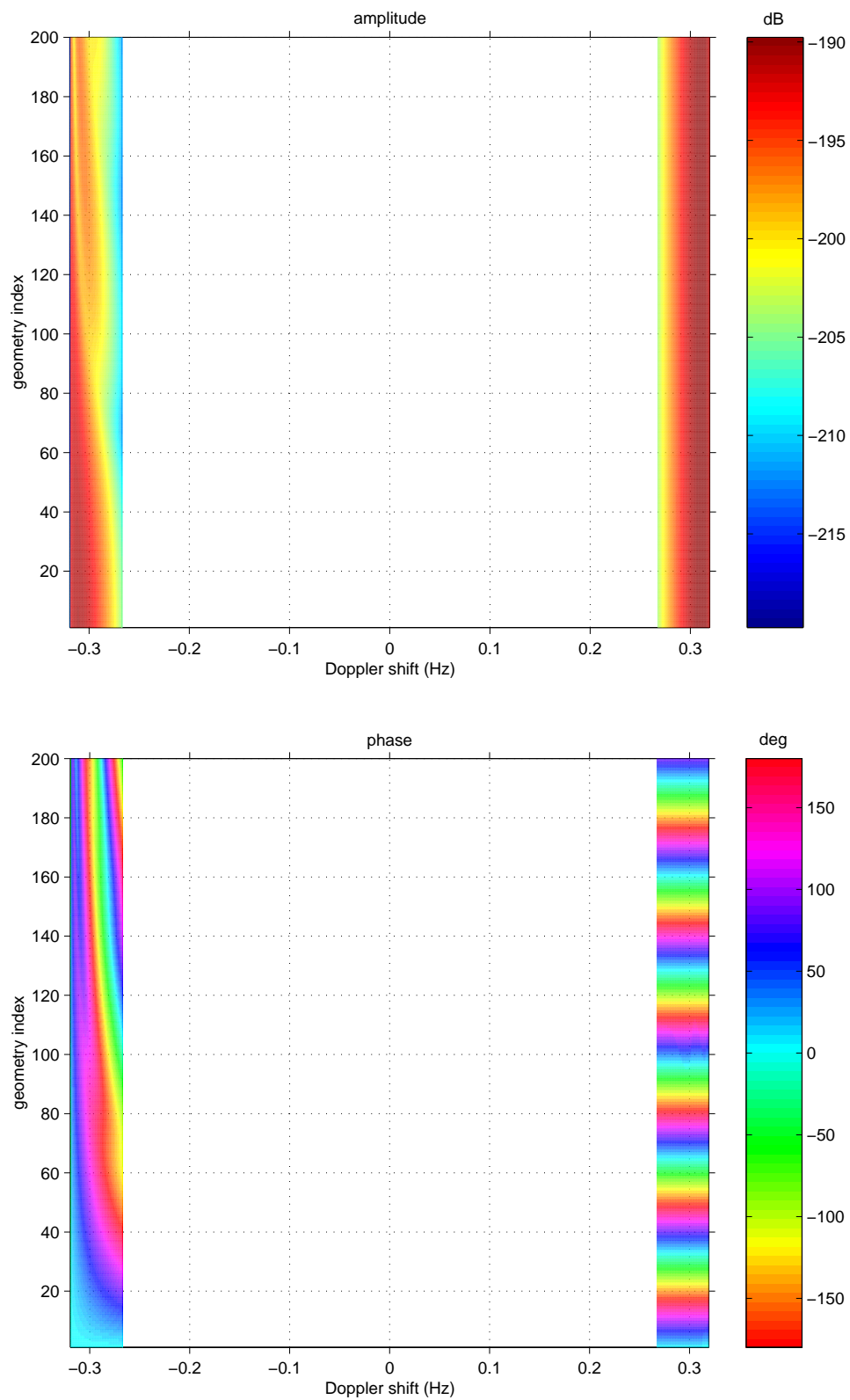


Fig. 20 — CSD simulation 20

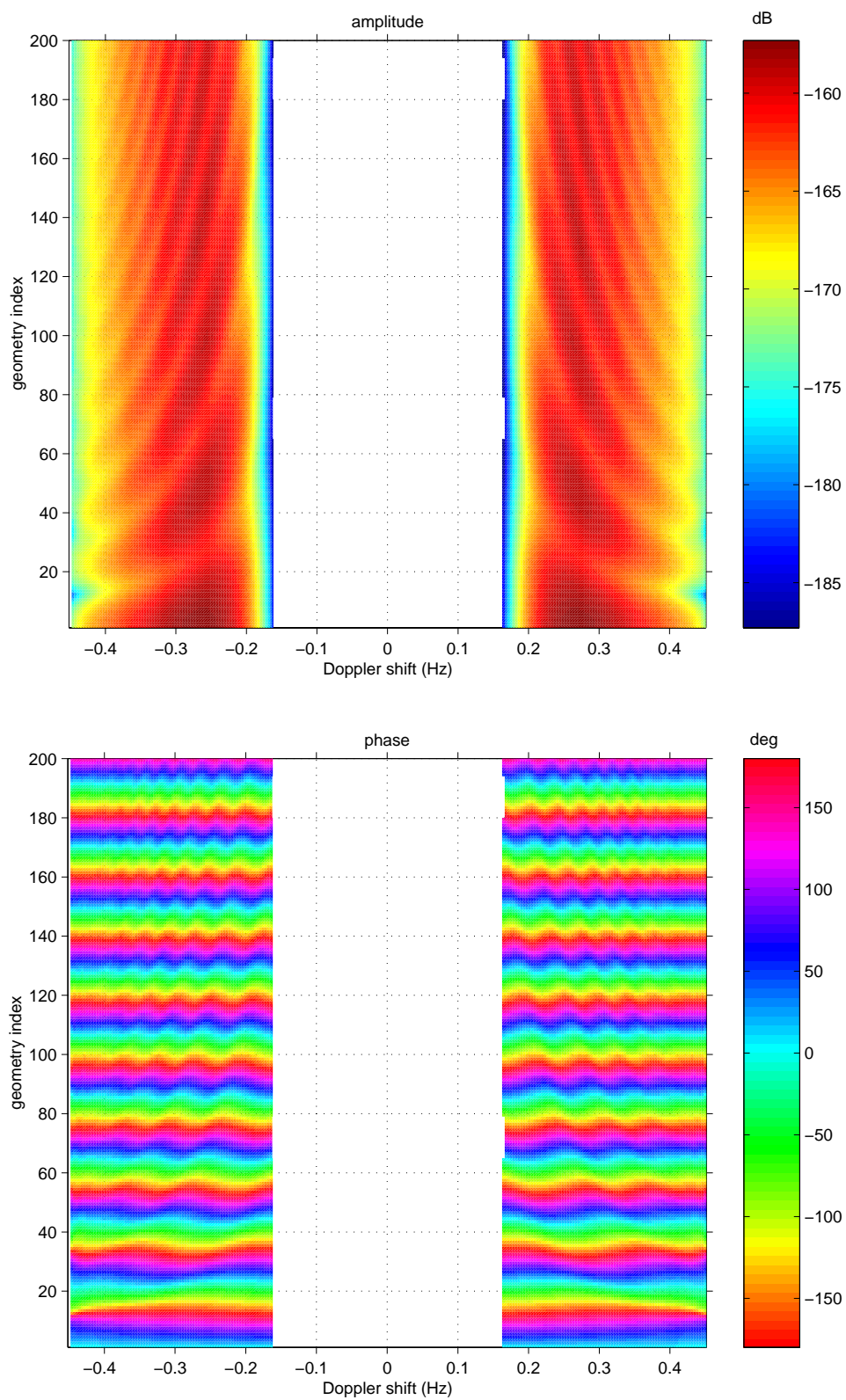


Fig. 21 — CSD simulation 21

## 5.2 Vertical Geometries

Here the receivers are located at a common horizontal position ( $\underline{r}_c = \underline{r}_{01} = \underline{r}_{02}$ ) but at different depths. Thus  $\varrho$  vanishes,  $\varphi$  is irrelevant, and we have

$$C_{\text{ref}}^{(2,0)}(\underline{r}_c, +|\omega|; z_0, z_1, z_2) = A \int_{F(\nu)} d\theta \{BH(\theta) + DH(\theta + \pi)\} \quad \dots \quad 0 < \nu < \nu_{\max} \quad (106)$$

$$A = \Phi(|\omega|) (k_0/4\pi r_c)^2, \quad B = (z_c/r_c)^2, \quad D = (z_0/r_c)^2, \quad (107)$$

where  $z_c = \sqrt{z_1 z_2}$  is the geometric mean of the receiver depths.

For simulations 23–25,  $z_1$  and  $z_2$  vary from 20 m to 120 m in 10 m steps, with  $z_1 \geq z_2$ . The resulting 66 geometries are numbered in order of increasing  $z_c$  (see Fig. 22). In all three simulations  $f_0 = 100$  Hz,  $U = 5$  m/s, and  $\mu = 4$ . ( $\varrho = 0$  m, and  $\varphi$  is undefined.) In simulations 23, 24, and 25,  $z_0$  is 20 m, 70 m, and 120 m, respectively. Since Eq. (106) produces real-valued CSDs, the amplitudes are plotted but not the corresponding phases.

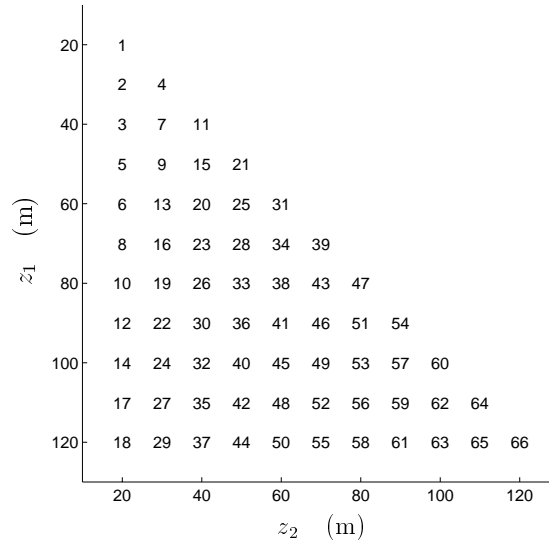


Fig. 22 — Geometry index values for the receiver depths used in simulations 23–25. Geometries are enumerated so that  $z_c = \sqrt{z_1 z_2}$  increases monotonically with the geometry index.

Since the receivers are situated under a highly directional field of surface waves almost straight downwind from the source, it is a good approximation to neglect  $H(\theta + \pi)$  in favor of  $H(\theta)$ . Then the upper and lower sidebands are given approximately by

$$C_{\text{ref}}^{(2,0)}(\underline{r}_c, +|\omega|; z_0, z_1, z_2) \approx \left( A \int_{F(\nu)} d\theta H(\theta) \right) \times B \quad (108a)$$

$$C_{\text{ref}}^{(2,0)}(\underline{r}_c, -|\omega|; z_0, z_1, z_2) \approx \left( A \int_{F(\nu)} d\theta H(\theta) \right) \times D. \quad (108b)$$

This explains why the upper sideband is independent of  $z_0$  but increases with the geometry index (i.e., with  $z_c$ ) in exactly the same way in all three simulations, while the lower sideband is independent of geometry index but increases with  $z_0$ .

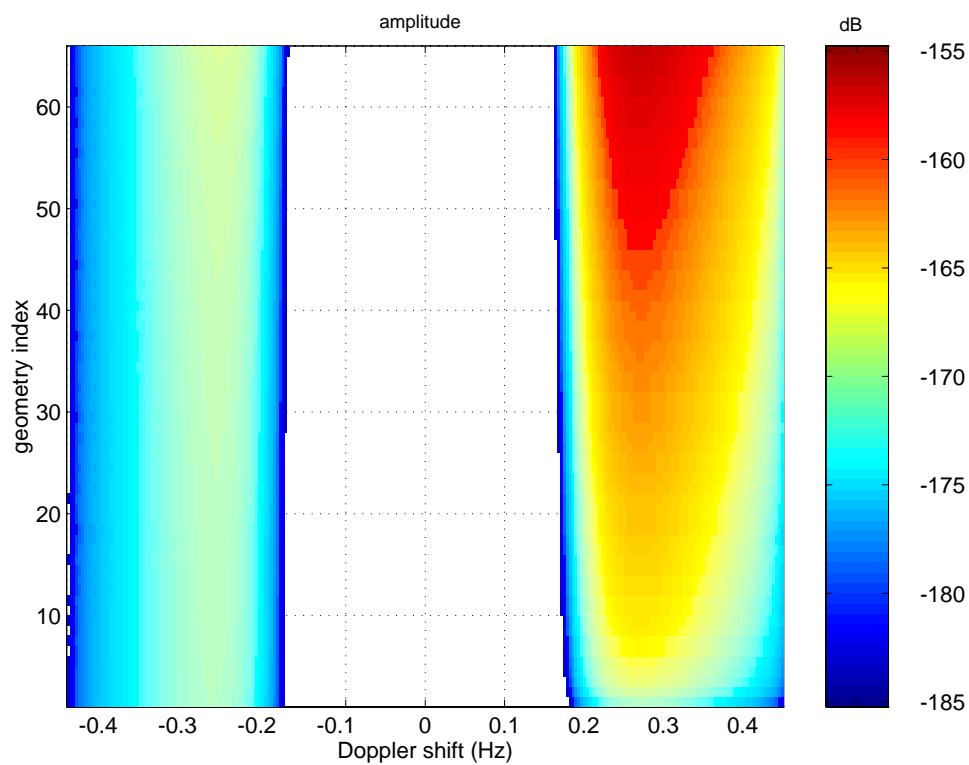


Fig. 23 — CSD simulation 23

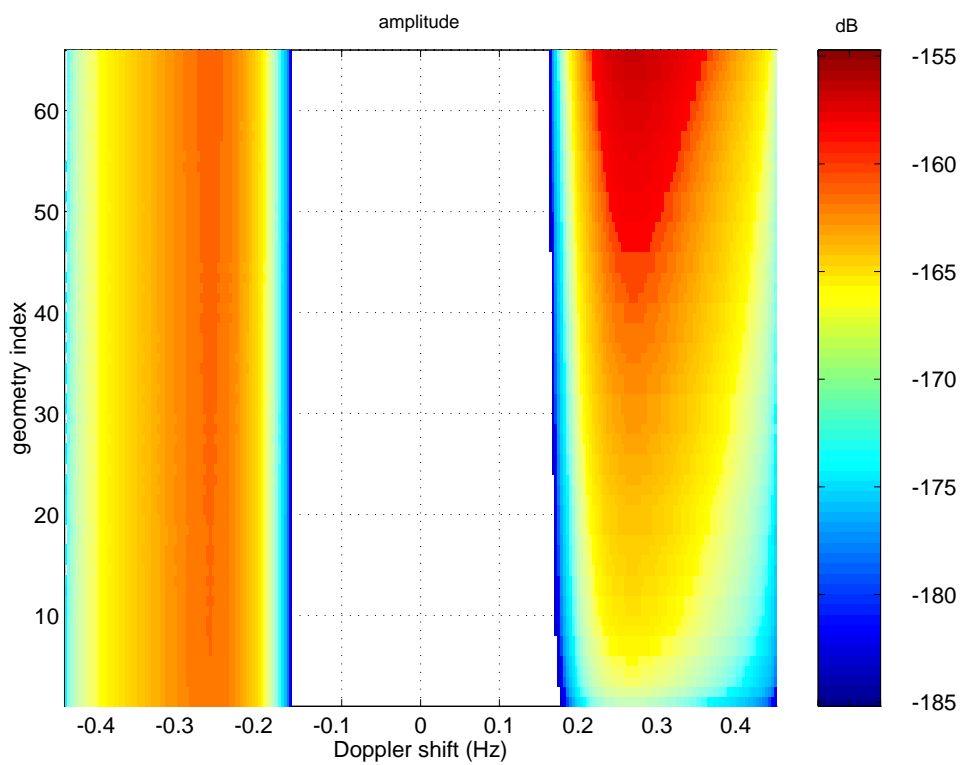


Fig. 24 — CSD simulation 24

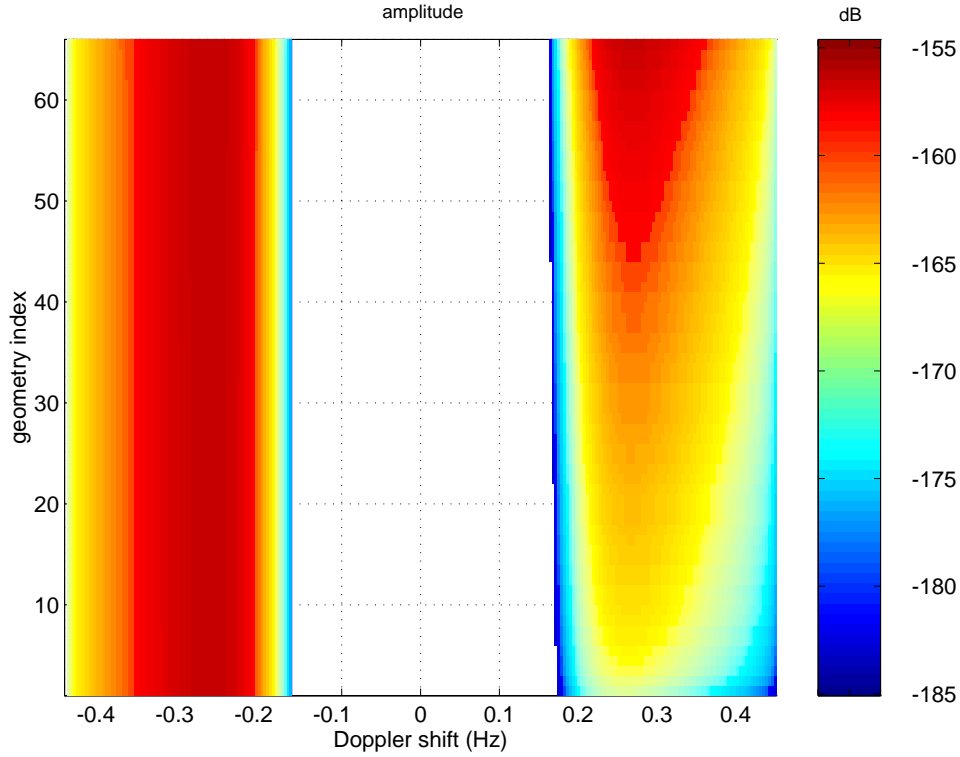


Fig. 25 — CSD simulation 25

## 6. SUMMARY AND CONCLUSIONS

The problem of multistatic reverberation from a sea surface has been posed with a narrowband source and a pair of receivers deployed beneath the surface of a fully developed wind-driven sea. The small-waveheight approximation was used to express the cross-spectral density of the reverberation as a sum of baseband and sideband integrals over the mean sea surface. Statistical stationarity and the customary angle/frequency factorization *ansatz* for surface-wave moments were used to reduce these expressions to manageable form—notably Eqs. (29) and (30) for the sidebands. The further assumption of a homogeneous ocean and shallow source and receiver placement allowed these expressions to be simplified into analytic forms containing only a single (azimuth) integration. The sideband result, Eqs. (98) and (99), was embodied in a Matlab script with (a) the gravity-wave dispersion relation for deep water, (b) the Pierson-Moskowitz power spectrum, and (c) an empirical directionality from Longuet-Higgins. This computer tool was used to explore the parametric dependence of the sideband structure on the depth and orientation of the source and receivers, the frequency and wind speed, and the directionality of the surface waves.

The aim of the work has been to provide a rapid, reliable means of calculating the reverberation CSD, particularly the Doppler components, for essentially any pair of receivers. This capability is essential in designing and evaluating beamformers for active operation against moving targets. The output of an array (whether horizontal, vertical, or volumetric) and, thus, the input for its associated beamformer (whether conventional or nonlinear) is the complex cross-spectral density matrix—the matrix of cross-spectral densities for the hydrophones taken in pairs.

One should really not expect to make many sweeping predictions about the operational performance of beamformers by simply pondering the structure of the reverberation CSD. It is too

complicated. The amplitudes and phases of its sidebands are nontrivial functions of frequency, wind speed, and surface directionality in addition to source and receiver position. Furthermore, the process of creating an effective beamformer is an art unto itself, and the CSD is only the raw material, not the finished product. Nevertheless, some rudimentary design ideas do seem to emerge from the CSD analysis undertaken here. For instance, it is clear from the vertical geometry simulations that, if the receivers lie downwind (upwind) under a fairly directional sea surface, then operating with the source at a shallow depth should improve the LSB (USB), though this would not work on the USB (LSB). However, the most straightforward approach might be to look for robust ways to remove the sidebands. They are produced by Bragg scattering from a set of points on the sea surface near each receiver and at another set near the source (the \*s in Fig. 10). One obvious approach for eliminating the sidebands is to use directional sources and receivers. The simple expedient of using a receiver beampattern with a vertical null of about  $45^\circ$  half-width should help significantly. The source might be a horizontal linear array laid out along the receiver direction. Conical beams could be steered in the usual way, skipping the beam whose intersection with the surface coincides with the hyperbola formed by the near-source surface scattering points.

There are several directions in which extensions to this work might be pursued. One of these is to allow the source to have nonvanishing bandwidth. This has been anticipated and would only require an additional frequency convolution. Another possibility is to modify the surface description. Different functional forms could certainly be used for the directionality and power spectrum. It would be quite easy, for example, to replace the Pierson-Moskowitz spectrum with the Toba spectrum [30]. A further option is to extend the treatment beyond the uniform ocean model—to ducted propagation in shallow water, for example. This would enhance the operational relevance of the effort, though at the cost of a potentially very great increase in analytical complexity. Finally, one might improve the treatment of the surface boundary condition (e.g., replace the small-waveheight approximation with a small-slope condition [30]). This would mean a complete reformulation of much of the analytic approach, and the level of effort required is unclear.

## 7. ACKNOWLEDGMENT

This work was supported by the Office of Naval Research.

## REFERENCES

1. P.M. Ogden and F.T. Erskine, "Surface Scattering Measurements using Broadband Explosive Charges in the Critical Sea Test Experiments," *J. Acoust. Soc. Am.* **95**, 746–761 (1994).
2. E.Y. Harper and F.M. Labianca, "Perturbation Theory for Scattering of Sound from a Point Source by a Moving Rough Surface in the Presence of Refraction," *J. Acoust. Soc. Am.* **57**, 1044–1050 (1975).
3. E.Y. Harper and F.M. Labianca, "Scattering of Sound from a Point Source by a Rough Surface Progressing over an Isovelocity Ocean," *J. Acoust. Soc. Am.* **58**, 349–364 (1975).
4. F.M. Labianca and E.Y. Harper, "Asymptotic Theory of Scattering by a Rough Surface Progressing over an Inhomogeneous Ocean," *J. Acoust. Soc. Am.* **59**, 799–812 (1976).
5. F.M. Labianca and E.Y. Harper, "Sideband Structure of Sound from a Harmonic Point Source Scattered by a Rough Surface Moving over an Upward-Refracting Ocean," *J. Acoust. Soc. Am.* **61**, 378–389 (1977).
6. F.M. Labianca and E.Y. Harper, "Connection Between Various Small-Waveheight Solutions of the Problem of Scattering from the Ocean Surface," *J. Acoust. Soc. Am.* **62**, 1144–1157 (1977).
7. J. S. Bendat and A. G. Piersol, *Random Data: Analysis and Measurement Procedures* (Wiley-Interscience, New York, 1971).
8. M.J. Beran and G.B. Parrent, Jr., *Theory of Partial Coherence* (Prentice-Hall, Englewood Cliffs, N.J., 1964).
9. M. Born and E. Wolf, *Principles of Optics*, 6th ed. (Pergamon, Oxford, 1980).
10. A.S. Marathy, *Elements of Optical Coherence Theory* (Wiley, New York, 1982).
11. J. Peřina, *Coherence of Light*, 2nd ed. (Reidel, Dordrecht, Holland, 1985).
12. P.W. Goalwin, "A Stationary Phase Approach to the Calculation of the Correlation of the Acoustic Field Scattered from a Two-Dimensional Random Sea Surface," *J. Acoust. Soc. Am.* **93**, 214–223 (1993).
13. M. Rahman, *Water Waves: Relating Modern Theory to Advanced Engineering Applications* (Oxford Univ. Press, Oxford, 1995).
14. W.C. Elmore and M.A. Heald, *Physics of Waves* (Dover, New York, 1969).
15. P.G. Bergmann, "The Wave Equation in a Medium with a Variable Index of Refraction," *J. Acoust. Soc. Am.* **17**, 329–222 (1946).
16. B. Friedman, *Principles and Techniques of Applied Mathematics* (Wiley & Son, New York, 1956).
17. S.T. McDaniel and A.D. Gorman, "Spectral Spread of Sea-Surface Reverberation," *J. Acoust. Soc. Am.* **74**, 241–248 (1983).
18. E.I. Thorsos, "Modeling of Frequency Broadening for Sea Surface Reverberation," *J. Acoust. Soc. Am.* **93**, Pt. 2, 2300 (1993).
19. C.T. Tindle, A.P. Stamp and K.M. Guthrie, "Virtual Modes and the Surface Boundary Condition in Underwater Acoustics," *J. Sound Vib.* **49**, 231–240 (1976).
20. P.M. Morse and M. Feshbach, *Methods of Mathematical Physics* (McGraw-Hill, New York, 1953).



21. J.W. Strutt Lord Rayleigh, "On the Dynamical Theory of Gratings," *Proc. Roy. Soc.* **A79**, 399–416 (1907).
22. D.R. Jackson, D.P. Winebrenner, and A. Ishimaru, "Comparison of Perturbation Theories for Rough Surface Scattering," *J. Acoust. Soc. Am.* **83**, 961–969 (1988).
23. S.M. Baxter and C.L. Morfey, *Angular Distribution Analysis in Acoustics* (Springer-Verlag, Berlin, 1986).
24. M.A. Donelan, J. Hamilton, and W.H. Hui, "Directional Spectra of Wind-Generated Waves," *Phil. Trans. R. Soc. Lond.* **A62**, 509–562 (1985).
25. W.A. Kuperman and F. Ingenito, "Spatial Correlation of Surface Generated Noise in a Stratified Ocean," *J. Acoust. Soc. Am.* **67**, 1988–1996 (1980).
26. W.J. Pierson and L. Moskowitz, "A Proposed Spectral form for Fully Developed Wind Seas Based on the Similarity Theory of S.A. Kitaigorodskii," *J. Geophys. Res.* **69**, 5181–5190 (1965).
27. O.M. Phillips, *The Dynamics of the Upper Ocean*, 2nd ed. (Cambridge Univ. Press, Cambridge, 1977).
28. M.S. Longuet-Higgins, D.E. Cartwright, and D.N. Smith, "Observations of the Directional Spectrum of Sea Waves Using the Motions of a Floating Buoy," *Proc. Conf. Ocean Wave Spectra*, 111–132, (Prentice-Hall, Englewood Cliffs, N.J., 1963).
29. H. Mitsuyasu, F. Tasai, T. Suhara, S. Mizuno, M. Ohkusu, T. Honda, and K. Rikiishi, "Observations of the Directional Spectrum of Ocean Waves Using a Cloverleaf Buoy," *J. Phys. Ocean.* **5**, 750–760 (1975).
30. R. Dashen, F.S. Henyey, and D. Wurmser, "Calculations of Acoustic Scattering from the Ocean Surface," *J. Acoust. Soc. Am.* **88**, 310–315 (1990).

## Appendix

### BIPOLAR COORDINATES

For any positive  $\gamma$ , bipolar coordinates  $(\xi, \eta)$  are defined as follows. The  $\xi$  coordinate lines are parameterized by

$$(x - \gamma \coth \xi)^2 + y^2 = (\gamma / \sinh \xi)^2 \quad \cdots \quad -\infty \leq \xi \leq +\infty , \quad (\text{A1})$$

which defines a circle with radius  $\gamma / |\sinh \xi|$  and center  $(x, y) = (\gamma \coth \xi, 0)$ . Circles with  $\xi > 0$  lie in the right half-plane, and those with  $\xi < 0$  are their mirror images in the left half-plane. Both approach the  $y$  axis as  $\xi$  vanishes and, in the  $\xi \rightarrow \pm\infty$  limits, they shrink down to the “vertices”  $(x, y) = (\pm\gamma, 0)$ . The  $\eta$  coordinate lines are parameterized by

$$x^2 + (y - \gamma \cot \eta)^2 = (\gamma / \sin \eta)^2 \quad \cdots \quad 0 \leq \eta \leq 2\pi , \quad (\text{A2})$$

which corresponds to a circle with radius  $\gamma / \sin \eta$  and center  $(x, y) = (0, \gamma \cot \eta)$ . The circles of this second family have their centers on the  $y$  axis, and all of them pass through both vertices. Each circle is split by the  $x$  axis into two arcs. The arc in the upper half-plane corresponds to an  $\eta$  value in the interval  $[0, \pi]$ , and the arc that completes the circle in the lower half-plane corresponds to that same  $\eta$  plus  $\pi$ .

The transformations to Cartesian coordinates  $(x, y)$  and polar coordinates  $(r, \theta)$  are

$$x = \frac{\gamma}{\cosh \xi - \cos \eta} \sinh \xi \quad y = \frac{\gamma}{\cosh \xi - \cos \eta} \sin \eta \quad (\text{A3})$$

$$r^2 = \frac{\cosh \xi + \cos \eta}{\cosh \xi - \cos \eta} \quad \tan \theta = \frac{\sin \eta}{\sinh \xi} . \quad (\text{A4})$$

These allow the plane vector  $\underline{r} = x\underline{e}_1 + y\underline{e}_2 = r\underline{\underline{R}}(\theta)\underline{e}_1$  to be expressed directly in terms of bipolar-coordinate operations:<sup>13</sup>

$$\underline{r} = -\frac{\underline{\underline{1}} + w\underline{\underline{R}}(-\eta)}{\underline{\underline{1}} - w\underline{\underline{R}}(-\eta)}\gamma\underline{e}_1 \quad \cdots \quad \xi < 0 \quad (\text{A5a})$$

$$\underline{r} = +\frac{\underline{\underline{1}} + w\underline{\underline{R}}(+\eta)}{\underline{\underline{1}} - w\underline{\underline{R}}(+\eta)}\gamma\underline{e}_1 \quad \cdots \quad \xi > 0 , \quad (\text{A5b})$$

using the logarithmic measure  $w = e^{-|\xi|}$ . The inverse operators are easily found to be

$$\left(\underline{\underline{1}} - w\underline{\underline{R}}(\pm\eta)\right)^{-1} = \left(1 - 2w \cos \eta + w^2\right)^{-1} \left(\underline{\underline{1}} - w\underline{\underline{R}}(\mp\eta)\right) . \quad (\text{A6})$$

The vertices are the  $w \rightarrow 0$  limits,  $\underline{r} = \pm\gamma\underline{e}_1$ . Equations (A5) and (A6) are used directly in the stationary-phase analysis in the body of the report.

---

<sup>13</sup>Ordering (i.e., the distinction between  $\underline{\underline{A}}\underline{\underline{B}}^{-1}$  and  $\underline{\underline{B}}^{-1}\underline{\underline{A}}$ ) is irrelevant here. Since these operators are all 2-D rotations, they all commute with each other.

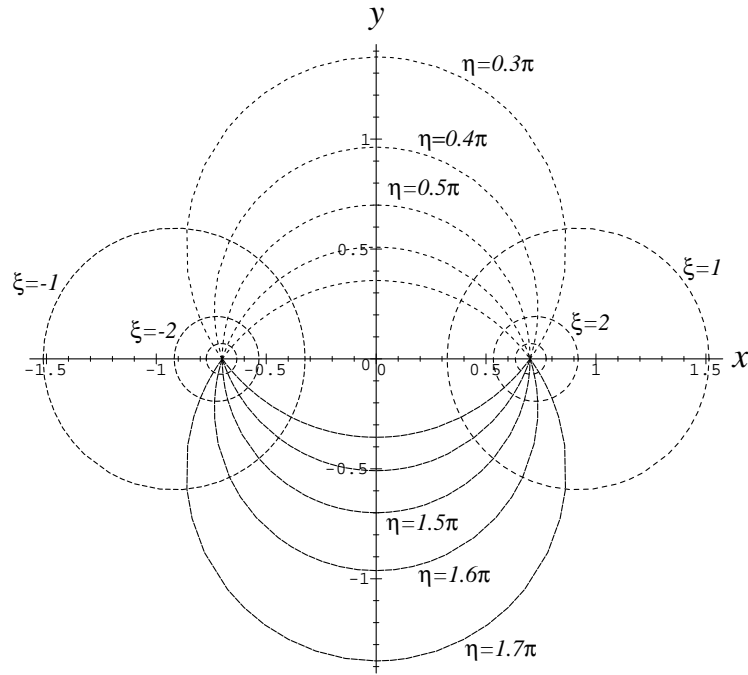


Fig. A1 — Bipolar coordinates for  $\gamma = 0.7$ . Coordinate lines are shown for:  $\xi = 1, 2, 3$  (circles in  $x > 0$  half-plane);  $\xi = -1, -2, -3$  (circles in  $x < 0$  half-plane);  $\eta = 0.3\pi, 0.4\pi, 0.5\pi, 0.6\pi, 0.7\pi$  (arcs in  $y > 0$  half-plane); and  $\eta = 1.3\pi, 1.4\pi, 1.5\pi, 1.6\pi, 1.7\pi$  (arcs in  $y < 0$  half-plane). The vertices are the two points on the  $x$  axis where circles with different  $\eta$  values intersect.